

Improved results of chiral limit study with the large N_c standard U(3) ChPT inputs in the on-shell renormalized quark-meson model

Vivek Kumar Tiwari^{1,*}

¹Department of Physics, University of Allahabad, Prayagraj, India-211002

(Dated: February 13, 2026)

When the f_π , f_K and M_η^2 given by the (m_π, m_K) dependent scaling relations of the large N_c standard U(3) Chiral perturbation theory (ChPT) and the infrared regularized U(3) ChPT, are used in the on-shell renormalized 2+1 flavor quark-meson (RQM) model to find its parameters in the path to the chiral limit $(m_\pi, m_K) \rightarrow 0$ away from the physical point $(m_\pi^{\text{Phys}}, m_K^{\text{Phys}}) = (138, 496)$ MeV, one gets the respective framework of RQM-S model and RQM-I model. Computing and comprehensively comparing the RQM-S and I model Columbia plots for the $m_\sigma = 400, 500$ and 600 MeV, it has been shown that the use of large N_c standard U(3) ChPT inputs give the better and improved framework for the Chiral limit studies as the RQM-S model tricritical lines show the expected saturation pattern after becoming flat in the vertical meson (quark) mass $\mu - m_K$ ($\mu - m_s$) plane for all the cases of m_σ whereas the divergent RQM-I model tricritical line for the $m_\sigma = 500$ MeV becomes strongly divergent when the $m_\sigma = 600$ MeV. The relative position $m_K^{\text{TCP}}/m_K^{\text{Phys}}(m_s^{\text{TCP}}/m_s^{\text{Phys}})$ of the RQM-S model tricritical point $_{\text{TCP}}$ on the $m_K(m_s)$ axis for the $m_\pi(m_{ud}) = 0$, shifts from the 0.5016 to 0.4405(0.2927 to 0.2280) whereas the critical pion (light quark) mass $m_\pi^c(m_{ud}^c)$ changes from the 134.51(3.8) to 117.26(2.9) MeV when the $m_\sigma = 400 \rightarrow 600$ MeV. In contrast, the shift of $m_K^{\text{TCP}}/m_K^{\text{Phys}}(m_s^{\text{TCP}}/m_s^{\text{Phys}})$ from the 0.4405 to 0.2988(0.2280 to 0.1068) and the change of $m_\pi^c(m_{ud}^c)$ from the 117.26(2.9) to 82.07(1.43) MeV is significantly large when the $m_\sigma = 600 \rightarrow 800$ MeV. The tricritical line shrinks to very small regions for the high $m_\sigma = 750$ MeV. Even though the first order regions in the horizontal $m_\pi - m_K$ plane of the RQM-S model Columbia plot, get much reduced for the $m_\sigma = 750$ MeV, its spread is comparable to what has been found in the QM model Columbia plot drawn by the functional renormalization group methods for the $m_\sigma = 530$ MeV.

I. INTRODUCTION

The color charge neutral hadrons, which are the units of Quantum Chromodynamics (QCD) at low energies, get dissolved into color charge carrying quark gluon units for extremely high temperatures and densities and such a QCD phase transition [1–5] gives the color conducting medium of quark gluon plasma (QGP). The QCD phase transition studies are very important for understanding the early universe evolution [6, 7], the structure of compact stars [8–10], and the nature of the strong interaction in heavy-ion collision experiments [11–14]. The chiral symmetry and color confinement are two important and deeply interlinked properties of QCD. The phase transition is theoretically constructed by exploiting the approximate $SU_A(3)$ chiral symmetry of the QCD Lagrangian which becomes exact for the massless light u, d and strange s quarks. The exact $SU_A(3)$ chiral symmetry gets spontaneously broken for the low temperatures and densities in the non-perturbative low energy QCD vacuum giving the eight massless Goldstone bosons which constitute the observed octet of light pions with a relatively heavier K and η mesons as pseudo-Goldstone modes in nature because the chiral symmetry is broken explicitly also by the very small (small) mass of light (strange) quark. The first principle lattice QCD (LQCD) simulations have settled that the chiral symmetry restoring phase transition at $\mu = 0$ for the observed π and K

meson masses corresponding to the real light and strange quark masses at the physical point, is a crossover transition with pseudo-critical temperature $T_\chi \equiv 155 \pm 2$ MeV [15–19].

The chiral transition is first order in the massless chiral limit $m_u = m_d = m_{ud} = 0 = m_s$ according to the universality [20] arguments and it becomes second order of the $O(4)$ universality class if $m_{u,d} = 0$, $m_s = \infty$ with the strong $U_A(1)$ axial anomaly [21] (η' mass $m_{\eta'}(T_c) \gg T_c$) at the chiral symmetry restoring critical temperature T_c . The second chiral order transition becomes first order at a tricritical point $_{\text{TCP}}$ for some finite $m_s = m_s^{\text{TCP}}(m_K = m_K^{\text{TCP}})$ in the light chiral limit $m_{u,d} = 0$ ($m_\pi = 0$). The chiral crossover at $\mu = 0$ turns first order for the critical quark (pion) mass m_q (m_π) $< m_q^c(m_\pi^c)$ for three flavors $N_f = 3$ of degenerate quarks. The mass dependence of the order of chiral phase transitions and structures of the critical lines which separate the first from the second order and crossover chiral transition regions, are presented in the $m_\pi - m_K$ or $m_{ud} - m_s$ planes of the Columbia plot [22] which is well understood in the heavy quark mass limit both from the continuum and lattice QCD (LQCD) studies [23–27]. Since the LQCD results are prone to large variations on account of the strong cut-off and discretization effects, the exact mapping of the critical lines for the small masses in the $m_{u,d} - m_s$ ($m_\pi - m_K$) plane, becomes quite tough and challenging in the LQCD [28–33]. Confirming the first order region close to the chiral limit, different LQCD studies between 2001 to 2017 have found that the m_π^c lies in the range 290–67 MeV [29–35]. On the other

* vivekkrt@gmail.com

hand, no evidence of first-order transition has been found for small pion mass as the LQCD study with improved Wilson fermions constrains $m_\pi^c \leq 100$ MeV [36] while the study with improved $N_\tau = 6$ staggered fermions [37] give $m_\pi^c \leq 50$ MeV whereas the LQCD study with highly improved $N_\tau = 8$ staggered quarks [38] finds no first order region for $m_\pi^c \geq 80$ MeV and another study [39] suggests that m_π^c could even be zero. Considering the flavor dependence of the position of τ_{CP} , the Ref. [40] finds that the chiral transition is of second order in the chiral limit for $N_f = 3$. With the Möbius domain wall fermions, the Ref.[41] finds small $m_q^c \leq 4$ MeV. Since the implementation of chiral fermions on the lattice is a notoriously difficult problem, the order of chiral transition in the small mass regions of the Columbia plot, remains an unsettled issue even if the improved LQCD studies are suggesting a small or no first order regions in some cases.

The Dyson-Schwinger approach $N_f = 3$ study in Ref. [42] and another study in Ref. [43] apart from some LQCD studies, find that the chiral transition is of second order in the small mass regions of the Columbia plot. Using the functional renormalization group (FRG) methods in the local potential approximation (LPA), the very recent studies in Refs. [44, 45] have discussed their findings that instead of the ϵ expansion predictions of first order regions in the Ref. [20], the chiral transition can be of second order for $N_f \geq 2$ if the $U_A(1)$ symmetry gets restored at the T_χ . However they have added a caveat note that the effect of wave function renormalization that gets completely neglected under the LPA, might affect the final results. Furthermore since some studies [46–51] find that the axial $U_A(1)$ anomaly remains finite and relevant at the critical point T_χ while others [38, 52–55] claim that it vanishes, the thermal fate of the $U_A(1)$ anomaly remains unsettled [56]. The chiral limit behavior of the $U_A(1)$ symmetry restoring observables, has been studied in Refs. [57–61]. The recent study in the Ref. [62], has conjectured some novel signals if anomaly strength becomes very weak at the T_χ . The Ref. [63] recently proposed a scenario where the decreasing first order regions completely vanish to give second order transition in the Columbia plot when the the sixth order coupling for the $U_A(1)$ anomaly term, becomes relevant and strong.

The lattice QCD studies have a long history of getting support and insights from the effective theory model studies like the linear sigma model (LSM) [64–74], the quark-meson (QM) model [75–89] or the Nambu-Jona-Lasinio [90–92] (NJL) model and the non-perturbative FRG framework models [93–115]. The 2+1 flavor QM model FRG method study under the LPA in the Ref. [35] finds that, the critical pion mass $m_\pi^c \equiv 86$ MeV, obtained using the extended mean field approximation (e-MFA) in the QM model where the thermal and vacuum quantum fluctuations of only the quark loops are considered, becomes quite low $m_\pi^c \equiv 17$ MeV indicating much reduced first order regions in the Columbia plot when the thermal and vacuum quantum fluctuations of meson loops are also included in their study with the full FRG flow. How-

ever the Ref. [62] has pointed out that the approximation used in the above work is known to overestimate the mesonic fluctuations [116] that tend to soften the chiral transition. Including the nonperturbative mesonic loop corrections in the Hartree approximation of LSM using the Cornwall-Jackiw-Tomboulis (CJT) two-particle (2PI) irreducible effective action formalism, the beyond perturbation method studies [65, 66] reported a large first order region in the Columbia plot when the $U_A(1)$ anomaly is absent and the results show drastic σ mass dependence in the presence of the $U_A(1)$ anomaly where the heavier m_σ values give the first order regions which disappear for the realistic m_σ . Note that since it is not clear, how the σ meson of the Lagrangian is connected to the physical $\sigma/f_0(500)$ state [117], one computes the m_σ dependence of the results. Using the symmetry improved CJT called the SICJT formalism [118] in the LSM, the very recent study in the Ref. [119], finds a stable first-order regime with a definite τ_{CP} which shows small variation on increasing the m_σ . They clarified that the enhanced first order regions found with the conventional CJT formalism, are merely an artifact due to the lack of manifest invariance of Nambu Goldstone and low energy theorems at finite temperature.

The exact chiral effective potential of the renormalized QM (RQM) model was calculated recently after treating the quark one-loop vacuum fluctuations consistently in the Refs. [120–125] for the two flavor and the Refs. [126–131] for the three (2+1) flavor of the QM model. The parameters of the RQM model are renormalized on-shell by matching the counter terms in the on-shell scheme with those in the modified minimal subtraction $\overline{\text{MS}}$ scheme when the mass parameter and the running couplings are put into the relation of the pole masses of the pseudoscalar π , K , η , η' and the scalar σ mesons. Since the condensate dependent part of the $U_A(1)$ anomaly term gets modified when the meson self energies due to quark loops are calculated using the pole masses of mesons, the renormalized 't Hooft coupling c gets significantly stronger. Further, the renormalized explicit chiral symmetry breaking strength $h_x(h_y)$ gets weaker by a small (relatively large) amount. The RQM model with the above novel features, got developed recently to give very fruitful frameworks of chiral limit studies by enriching the model with the chiral perturbation theory (ChPT) inputs [128, 129]. Its parameter fixing away from the physical point for the reduced π and K masses as the $m_\pi, m_K \rightarrow 0$, was refined by using the (m_π, m_K) dependent scaling relations for the f_π, f_K and M_η^2 given by the $\mathcal{O}(\frac{1}{f^2})$ accurate results of the large N_c standard $U(3)$ chiral perturbation theory (ChPT) [132–137] in the RQM-S model framework [128] and the infrared regularized $U(3)$ ChPT [69, 138–141] in the RQM-I model framework [129]. The enrichment of the RQM model with the ChPT inputs, cured the problem of the loss of the spontaneous chiral symmetry breaking (SCSB) for the mass range $m_\sigma = 400 – 800$ MeV when the $m_\pi, m_K \rightarrow 0$ in the commonly used method [64, 66, 82, 92, 93, 99] of chiral

limit studies in the QM model called the fixed-ultraviolet (UV) scheme [35] where the light (strange) explicit chiral symmetry breaking strengths $h_x(h_y)$ are changed while all other parameters are kept same as the ones at the physical point. It is emphasized that RQM model frameworks do not have any ambiguity when parameters get fixed towards the chiral limit for the $m_\sigma = 400 \rightarrow 800$ MeV whereas the e-MFA:FRG QM model chiral limit study in the Ref. [35], where the FRG flow allows for the scalar σ masses only in the range $m_\sigma \in [400, 600]$ MeV, could avoid the loss of SCSB only by heuristically adjusting the initial effective action successively to larger scales $\Lambda' > \Lambda$ at each step of reducing the strengths h_x and h_y such that the f_π does not change in their ChPT motivated fixed f_π scheme.

The very recent work of the Ref. [128] showed that, for the $m_\sigma = 530$ MeV, the chiral limit study results in the RQM-S model are approximately similar to those found in the RQM-I model but the RQM-I model tricritical line, that separates the first and second order transitions in the vertical $\mu - m_K$ plane of the Columbia plot at $m_\pi = 0$, looks divergent after the $m_K \geq 500$ MeV while the RQM-S model tricritical line became flat showing proper saturation that is consistent and desirable on the physical grounds because the 2+1 flavor tricritical line is expected to be connected to the tricritical point of the two flavor chiral limit [142] at higher μ and m_K . The first motivation of the present work is to compute the Columbia plots of the RQM-S model for the $m_\sigma = 400, 500, 600$ MeV and the RQM-I model for the $m_\sigma = 500$ and 600 MeV. Bringing out similarities and differences after a thorough and comprehensive comparison of the RQM-S and RQM-I model Columbia plots for the $m_\sigma = 400, 500$ and 600 MeV, our first goal will let us find if the large N_c standard U(3) ChPT scaling relations for the (m_π, m_K) dependence of the f_π, f_K and M_η^2 , constitute the improved and better prescription for the Chiral limit studies for all the m_σ . Computing RQM-S model Columbia plots for the $m_\sigma = 750$ and 800 MeV and comparing them with those for the $m_\sigma = 400 \rightarrow 600$ MeV, our second goal is to find the relative shifts of the $_{\text{TCP}}$ at $m_K^{\text{TCP}}(m_s^{\text{TCP}})$ and the critical pion (quark) mass $m_\pi^c(m_{ud}^c)$ for the shrinking first order regions when the $m_\sigma = 600 \rightarrow 800$ MeV. Furthermore the divergence in the shape of tricritical line, that corresponds to significantly shrunk first order region in the $\mu - m_K$ ($\mu - m_s$) plane, will also be revealed when the $m_\sigma = 750$ MeV is high. Our third goal is to compare the Columbia plots of the RQM-S model, when the strength of chiral transition gets significantly diluted for the $m_\sigma = 750$ and 800 MeV, with the Columbia plots of the e-MFA:FRG QM model study for the $m_\sigma = 530$ MeV and the QM with fermionic vacuum term (QMVT) model study for the $m_\sigma = 400$ MeV where the strength of chiral transition gets strongly softened by the very large smoothing effects of quark one-loop vacuum fluctuations due to its treatment in the $\overline{\text{MS}}$ scheme of renormalization and the use of curvature masses of mesons to fix the model parameters.

The paper is arranged as follows. The 2+1 flavor RQM model is presented briefly in the section II. The Chiral perturbation theory (ChPT) scaling of the f_π, f_K and M_η has been discussed in the section II A where the infrared regularized U(3) ChPT formulas are presented in the section II A-1 whereas the large N_c standard U(3) ChPT formulas are described in the section II B. Results and discussions are presented in the section III. The temperature variations of the π and σ curvature masses in the RQM-S and RQM-I models for the $m_\sigma = 400, 500, 600, 750$ and 800 MeV are presented in the section III A. The RQM-S and RQM-I model Columbia plots for the $m_\sigma = 400, 500, 600$ MeV are presented and compared with each other in the section III B where the RQM-S model Columbia plot for the $m_\sigma = 750, 800$ MeV are also compared. The RQM-S and RQM-I model Columbia plots in the quark mass $m_{ud} - m_s$ and $\mu - m_s$ planes for the $m_\sigma = 400, 500, 600$ MeV are presented and compared with each other in the section III C where the RQM-S model Columbia plots for the $m_\sigma = 750$ and 800 MeV are also presented. The whole work is summarized in the section IV.

II. THE RQM MODEL

The RQM model effective potential as presented in the Ref. [128, 129] is reproduced below in this section. The model Lagrangian [65, 82, 86] is written as :

$$\mathcal{L}_{Q\mathcal{M}} = \bar{\psi}[i\gamma^\mu D_\mu - g T_a(\sigma_a + i\gamma_5\pi_a)]\psi + \mathcal{L}(\mathcal{M}) . \quad (1)$$

$$\begin{aligned} \mathcal{L}(\mathcal{M}) = & \text{Tr}(\partial_\mu \mathcal{M}^\dagger \partial^\mu \mathcal{M} - m^2(\mathcal{M}^\dagger \mathcal{M})) \\ & - \lambda_1 [\text{Tr}(\mathcal{M}^\dagger \mathcal{M})]^2 - \lambda_2 \text{Tr}(\mathcal{M}^\dagger \mathcal{M})^2 \\ & + c[\det \mathcal{M} + \det \mathcal{M}^\dagger] + \text{Tr}[H(\mathcal{M} + \mathcal{M}^\dagger)] \end{aligned} \quad (2)$$

The Yukawa coupling g couples the flavor triplet quark fields ψ (color N_c -plet Dirac spinor) to the nine scalar(pseudo-scalar) meson ξ fields $\sigma_a(\pi_a)$ of 3×3 complex matrix $\mathcal{M} = T_a \xi_a = T_a(\sigma_a + i\pi_a)$. $T_a = \frac{\lambda_a}{2}$ where λ_a ($a = 0, 1..8$) are Gell-Mann matrices with $\lambda_0 = \sqrt{\frac{2}{3}} \mathbb{I}_{3 \times 3}$. The field ξ picks up the non-zero vacuum expectation value $\bar{\xi}$ in the 0 and 8 directions. The condensates $\bar{\sigma}_0$ and $\bar{\sigma}_8$ break the $SU_L(3) \times SU_R(3)$ chiral symmetry spontaneously while the external fields $H = T_a h_a$ with $h_0, h_8 \neq 0$ break it explicitly. The change from the singlet octet (0,8) to the light strange basis (x, y) gives $x(h_x) = \sqrt{\frac{2}{3}}\bar{\sigma}_0(h_0) + \frac{1}{\sqrt{3}}\bar{\sigma}_8(h_8)$ and $y(h_y) = \frac{1}{\sqrt{3}}\bar{\sigma}_0(h_0) - \sqrt{\frac{2}{3}}\bar{\sigma}_8(h_8)$. Considering mesons at mean field level with the thermal and quantum fluctuations of the quarks/anti-quarks, the grand potential [82, 86], is the sum of the vacuum effective potential $U(x, y)$ and the quark/anti-quark contribution $\Omega_{q\bar{q}}$ at finite temperature T and quark chemical potential μ_f ($f = u, d, s$).

$$\Omega_{\text{MF}}(T, \mu) = U(x, y) + \Omega_{q\bar{q}}(T, \mu; x, y) . \quad (3)$$

$$\Omega_{q\bar{q}}(T, \mu; x, y) = \Omega_{q\bar{q}}^{vac} + \Omega_{q\bar{q}}^{T,\mu}. \quad (4)$$

$$\begin{aligned} U(x, y) = & \frac{m^2}{2} (x^2 + y^2) - h_x x - h_y y - \frac{c}{2\sqrt{2}} x^2 y \\ & + \frac{\lambda_1}{2} x^2 y^2 + \frac{1}{8} (2\lambda_1 + \lambda_2) x^4 + \frac{1}{8} (2\lambda_1 + 2\lambda_2) y^4. \end{aligned} \quad (5)$$

$$\Omega_{q\bar{q}}^{vac} = -2N_c \sum_f \int \frac{d^3 p}{(2\pi)^3} E_q \theta(\Lambda_c^2 - \vec{p}^2). \quad (6)$$

$$\Omega_{q\bar{q}}^{T,\mu} = -2N_c \sum_{f=u,d,s} \int \frac{d^3 p}{(2\pi)^3} T \left[\ln g_f^+ + \ln g_f^- \right]. \quad (7)$$

$$\Omega_{QM}(T, \mu, x, y) = U(x, y) + \Omega_{q\bar{q}}^{T,\mu}. \quad (8)$$

The $g_f^\pm = \left[1 + e^{-E_f^\pm/T}\right]$ where $E_f^\pm = E_f \mp \mu_f$ and $E_f = \sqrt{p^2 + m_f^2}$ is the quark/anti-quark energy. The light (strange) quark mass $m_{u/d} = \frac{g_x}{2}$ ($m_s = \frac{g_y}{\sqrt{2}}$) and $\mu_u = \mu_d = \mu_s = \mu$. The quark one-loop vacuum term with ultraviolet cut-off Λ_c in Eq. (6) is dropped for the standard mean field approximation (s-MFA) of the quark meson (QM) model grand effective potential in Eq. (8). Several studies have used the minimal subtraction scheme to regularize the quark one-loop vacuum divergences after including the vacuum fluctuations in the extended mean field approximation (e-MFA) [143–149] but the effective potential $\Omega_{vac}(x, y) = U(x, y) + \Omega_{q\bar{q}}^{vac}$ in their treatment, turns inconsistent as they fix the model parameters using curvature masses of mesons which are obtained by taking the double derivatives of the effective potential with respect to the different fields at its minimum. The above mentioned inconsistency becomes apparent when one notes that the calculation of the curvature masses, involves the evaluation of the meson self-energies at zero momentum because the effective potential is the generator of the n-point functions of the theory at vanishing external momenta [120–127, 150–152]. It has to be noted that the pole definition of the meson mass is the physical and gauge invariant [153, 154] one.

Here, we will employ the consistent e-MFA RQM model effective potential calculated in our very recent works [126, 127] after relating the counter-terms in the $\overline{\text{MS}}$ scheme to those in the on-shell (OS) scheme [120–125]. The relations between the renormalized parameters of both the schemes are determined when the physical quantities (the on-shell pole masses of the $m_\pi, m_K, m_\eta, m_{\eta'}$ and m_σ , the pion and kaon decay constants f_π and f_K) are put into the relation of the $\overline{\text{MS}}$ running couplings and mass parameter. These relations are used as input when the effective potential is calculated using the modified minimal subtraction procedure. After the cancellation of the $1/\epsilon$ divergences, the vacuum effective potential $\Omega_{vac} = U(x_{\overline{\text{MS}}}, y_{\overline{\text{MS}}}) + \Omega_{\overline{\text{MS}}}^{q,vac} + \delta U(x_{\overline{\text{MS}}}, y_{\overline{\text{MS}}})$ in the $\overline{\text{MS}}$ scheme has been rewritten in Ref. [126] in terms of the scale Λ independent constituent quark mass parameters $\Delta_x = \frac{g_{\overline{\text{MS}}} x_{\overline{\text{MS}}}}{2}$ and $\Delta_y = \frac{g_{\overline{\text{MS}}} y_{\overline{\text{MS}}}}{\sqrt{2}}$ as the fol-

lowing.

$$\begin{aligned} \Omega_{vac}(\Delta_x, \Delta_y) = & \frac{m_0^2}{g_0^2} (2\Delta_x^2 + \Delta_y^2) - 2 \frac{h_{x0}}{g_0} \Delta_x - \sqrt{2} \frac{h_{y0}}{g_0} \Delta_y \\ & - 2 \frac{c_0}{g_0^3} \Delta_x^2 \Delta_y + 4 \frac{\lambda_{10}}{g_0^4} \Delta_x^2 \Delta_y^2 + 2 \frac{(2\lambda_{10} + \lambda_{20})}{g_0^4} \Delta_x^4 \\ & + \frac{(\lambda_{10} + \lambda_{20})}{g_0^4} \Delta_y^4 + \frac{2N_c \Delta_x^4}{(4\pi)^2} \left[\frac{3}{2} + \ln \left(\frac{\Lambda^2}{m_u^2} \right) + \ln \left(\frac{m_u^2}{\Delta_x^2} \right) \right] \\ & + \frac{N_c \Delta_y^4}{(4\pi)^2} \left[\frac{3}{2} + \ln \left(\frac{\Lambda^2}{m_u^2} \right) + \ln \left(\frac{m_u^2}{\Delta_y^2} \right) \right]. \end{aligned} \quad (9)$$

The condition that the minimum of the effective potential of the RQM model does not shift from that of the QM model fixes the scale Λ_0 [126, 127] as :

$$\ln \left(\frac{\Lambda_0^2}{m_u^2} \right) + \mathcal{C}(m_\pi^2) + m_\pi^2 \mathcal{C}'(m_\pi^2) = 0. \quad (10)$$

The terms $\mathcal{C}(m_\pi^2)$ and $\mathcal{C}'(m_\pi^2)$ and the derivations for the renormalized parameters $m_0^2 = (m^2 + m_{\text{FIN}}^2)$, $h_{x0} = (h_x + h_{x\text{FIN}})$, $h_{y0} = (h_y + h_{y\text{FIN}})$, $\lambda_{10} = (\lambda_1 + \lambda_{1\text{FIN}})$, $\lambda_{20} = (\lambda_2 + \lambda_{2\text{FIN}})$ and $c_0 = (c + c_{\text{FINTOT}})$ are given in detail in Refs. [126, 127]. The m_{FIN}^2 , $h_{x\text{FIN}}$, $h_{y\text{FIN}}$, $\lambda_{1\text{FIN}}$, $\lambda_{2\text{FIN}}$ and c_{FINTOT} are the finite on-shell corrections in the parameters at the scale Λ_0 . The experimental values of the pseudo-scalar meson masses $m_\pi, m_K, m_\eta, m_{\eta'}$ ($m_\eta^2 + m_{\eta'}^2$), the scalar σ mass m_σ and the f_π, f_K as input determine the tree level QM model quartic couplings λ_1, λ_2 , mass parameter m^2 , h_x, h_y and the coefficient c of the t'Hooft determinant term for the $U_A(1)$ axial anomaly [65, 82].

Although the f_π, f_K and g get renormalized due to the dressing of the meson propagator in the on-shell scheme, they do not change as the $g_{\overline{\text{MS}}} = g_{ren} = g_0 = g$, $x_{\overline{\text{MS}}} = x, y_{\overline{\text{MS}}} = y$ at Λ_0 . Further $x_{\overline{\text{MS}}} = f_{\pi,ren} = f_\pi$ and $y_{\overline{\text{MS}}} = \frac{2f_{K,ren} - f_{\pi,ren}}{\sqrt{2}} = \frac{2f_K - f_\pi}{\sqrt{2}}$ at the minimum. Using $\Delta_x = \frac{g_x}{2}$ and $\Delta_y = \frac{g_y}{\sqrt{2}}$, the vacuum effective potential in the Eq. (9) can be written in terms of the x and y as :

$$\begin{aligned} \Omega_{vac}^{\text{RQM}}(x, y) = & \frac{(m^2 + m_{\text{FIN}}^2)}{2} (x^2 + y^2) - (h_x + h_{x\text{FIN}}) x \\ & - (h_y + h_{y\text{FIN}}) y - \frac{(c + c_{\text{FINTOT}})}{2\sqrt{2}} x^2 y + \frac{(\lambda_1 + \lambda_{1\text{FIN}})}{2} x^2 y^2 \\ & + \frac{\{2(\lambda_1 + \lambda_{1\text{FIN}}) + (\lambda_2 + \lambda_{2\text{FIN}})\} x^4}{8} + (\lambda_1 + \lambda_{1\text{FIN}} + \lambda_2 \\ & + \lambda_{2\text{FIN}}) \frac{y^4}{4} + \frac{N_c g^4 (x^4 + 2y^4)}{8(4\pi)^2} \left[\frac{3}{2} - \mathcal{C}(m_\pi^2) - m_\pi^2 \mathcal{C}'(m_\pi^2) \right] \\ & - \frac{N_c g^4}{8(4\pi)^2} \left[x^4 \ln \left(\frac{x^2}{f_\pi^2} \right) + 2y^4 \ln \left(\frac{2y^2}{f_\pi^2} \right) \right]. \end{aligned} \quad (11)$$

$$\Omega_{QM}(T, \mu, x, y) = \Omega_{vac}^{\text{RQM}}(x, y) + \Omega_{q\bar{q}}^{T,\mu}. \quad (12)$$

The search of the grand potential minima $\frac{\partial \Omega_{\text{RQM}}}{\partial x} = \frac{\partial \Omega_{\text{RQM}}}{\partial y} = 0$ for the Eq. (12) gives the T and μ dependence of the x and y . The curvature masses of mesons

are different from their pole masses in the RQM model due to the on-shell renormalization of the parameters [151, 152]. The derivation of the RQM model curvature mass expressions for the mesons are presented in the section (IIA) of the Ref.[128]. When one uses the Eq. (11) to evaluate the equations of motion $\frac{\partial \Omega_{vac}^{RQM}}{\partial x} = 0 = \frac{\partial \Omega_{vac}^{RQM}}{\partial y}$, one gets the renormalized explicit chiral symmetry breaking strengths h_{x0} and h_{y0} as the following.

$$h_{x0} = m_{\pi,c}^2 f_\pi. \quad (13)$$

$$h_{y0} = \left(\sqrt{2} f_K m_{K,c}^2 - \frac{f_\pi}{\sqrt{2}} m_{\pi,c}^2 \right). \quad (14)$$

The pion and kaon curvature masses $m_{\pi,c}$ and $m_{K,c}$ as derived in the Ref. [126] have the following expressions.

$$m_{\pi,c}^2 = m_\pi^2 \left\{ 1 - \frac{N_c g^2}{4\pi^2} m_\pi^2 \mathcal{C}'(m_\pi^2, m_u) \right\}. \quad (15)$$

$$\begin{aligned} m_{K,c}^2 = m_K^2 & \left[1 - \frac{N_c g^2}{4\pi^2} \left\{ \mathcal{C}(m_\pi^2, m_u) + m_\pi^2 \mathcal{C}'(m_\pi^2, m_u) \right. \right. \\ & - \left(1 - \frac{(m_s - m_u)^2}{m_K^2} \right) \mathcal{C}(m_K^2, m_u, m_s) + \\ & \left. \left. \left(1 - \frac{f_\pi}{f_K} \right) \left(\frac{m_u^2 - m_s^2 + 2m_s^2 \ln(\frac{m_s}{m_u})}{m_K^2} \right) \right] \right]. \quad (16) \end{aligned}$$

In order to see the consistency check of the above expressions, one can verify that when the $x = f_\pi$ and $y = \frac{(2f_K - f_\pi)}{\sqrt{2}}$ in the vacuum, the expression of $m_{p,11c}^2$ in the Eq. (18) of Ref. [128] gives the same value as the $m_{\pi,c}^2$ in the Eq. (15) while the expression of $m_{p,44c}^2$ in the Eq. (19) of Ref. [128] gives the value that is equal to the kaon curvature mass square $m_{K,c}^2$ given by the Eq. (16). The pion curvature mass $m_{\pi,c} = 135.95$ MeV in vacuum turns out to be 2.05 MeV smaller than its pole mass $m_\pi = 138$ MeV whereas the vacuum kaon curvature mass $m_{K,c} = 467.99$ MeV is 28.01 MeV smaller than its pole mass of $m_K = 496$ MeV [126, 127].

A. The ChPT scaling of f_π, f_K and $M_\eta^2 = m_\eta^2 + m_{\eta'}^2$

In order to investigate the current quark mass ($m_{u/d} - m_s$ plane) sensitivity of the chiral phase transition in the lower left corner of the Columbia plot, one resorts to the equivalent description of the pion kaon mass $m_\pi - m_K$ plane because the low energy effective theory framework of the 2+1 flavor QM model deals with scalar and pseudo-scalar mesons rather than the u, d and s quarks of the perturbative QCD regime. The explicit chiral symmetry breaking source strengths in the non-strange and strange directions $h_x = f_\pi m_\pi^2$, $h_y = \sqrt{2} f_K m_K^2 - f_\pi m_\pi^2 / \sqrt{2}$ as well as the effective theory model parameters can be determined only at the physical point because here the experimental information is in tune with the underlying theory

of QCD. Since it is not clear, a priori, how the parameters change as the system is tuned away from the physical point, different strategies are adopted to fix the model parameters. The fixed-ultraviolet (UV) scheme [35] is the most commonly used strategy [64, 66, 82, 92, 93, 99] in the literature. It relies on the assumption that the change in current quark masses of QCD can be directly mapped onto a change of symmetry breaking source strengths. Hence one varies the $h_x(h_y)$ while keeps all other parameters same as the ones at the physical point such that the initial effective action does not change in the UV [35]. Since the spontaneous chiral symmetry breaking (SCSB) gets lost in the chiral limit as the mass parameter m^2 becomes positive for the moderate m_σ , the fixed-UV scheme does not work for the scalar σ mass range $m_\sigma = 400 - 800$ MeV [35, 82]. This problem for the chiral limit study in the QM model got circumvented in the Ref. [82] by choosing quite a large $m_\sigma \geq 800$ MeV.

Resch et. al. computed Columbia plots for the QM model in the Ref. [35] using nonperturbative FRG methods under the LPA. Motivated by the findings of ChPT, they proposed a fixed- f_π scheme where the initial effective action is to be heuristically adjusted to the larger scales ($\Lambda' > \Lambda$) at each step of the calculation when smaller masses are taken in the path to the chiral limit in the Columbia plot such that the pion decay constant f_π in the infra-red (IR) always remains fixed to its physical value. In the fixed- f_π scheme, the changing scale ($\Lambda' > \Lambda$) accounts for the change in parameters (which retain the same value as at the Λ in the fixed UV-scheme) when the chiral symmetry breaking strengths h_x and h_y are decreased away from the physical point. The problem of fixed-UV scheme is resolved by construction in the fixed- f_π scheme because the condensates being intimately related to the fixed f_π do not drop to zero and hence the SCSB does not get lost. The fixed f_π scheme suffers from the problem of a heuristic determination of the initial effective action [35], even though it is physically reasonable. More accurate methods of fixing the model parameters unambiguously will be employed below where one exploits the ChPT predicted scaling relations for the decay constants f_π, f_K and $M_\eta^2 = m_\eta^2 + m_{\eta'}^2$, when the m_π and $m_K \rightarrow 0$ and therefore the explicit chiral symmetry breaking strengths h_x and h_y approach zero in the RQM model as one moves away from the physical point towards the chiral limit in the Columbia plot.

The chiral symmetry of the QCD Lagrangian gets enhanced to the $U_L(3) \times U_R(3)$ when the quark loops responsible for the $U_A(1)$ anomaly get suppressed by taking the large N_c limit. Using the nonet of the Goldstone bosons where the η' meson becomes the ninth addition to the $SU_A(3)$ octet of (π, K, η) , one can construct the effective Lagrangian with $U(3)$ chiral symmetry. The systematic expansion of the Green functions of the $U(3)$ ChPT in powers momenta, quark masses and the $\mathcal{O}(p^2)$ parameter $\frac{1}{N_c}$, was introduced in the Ref. [132] and it got firmly established in Refs.[133–137]. The studies in Refs. [138–140] have argued that the large N_c arguments are not nec-

essary for constructing the effective Lagrangian with the singlet field as the additional $\frac{1}{N_c}$ counting scheme is imposed only to ensure that loops with an η' are suppressed by powers of $\frac{1}{N_c}$. They have pointed out that the mass of the η' particle that introduces an additional low energy scale of about 1 GeV, is proportional to $\frac{1}{N_c}$. Hence the η' can be treated perturbatively, for its systematic inclusion in the ChPT without using the $\frac{1}{N_c}$ counting rules. This alternative method of treating massive fields got firmly established in the Ref. [141] where the loop integrals are evaluated using a modified regularization scheme, the so-called infrared regularization, in which Lorentz and chiral invariance are kept at all stages [138, 139]. Discussing the inclusion of loops and renormalization issues, the authors in the Ref. [139], have argued that the η' loops do not contribute (at the fourth order Lagrangian) in infrared regularization and the η' can be treated as a background field while the contribution of Goldstone boson (π, K, η) loops get evaluated. The above discussed framework is different from the large N_c standard U(3) ChPT approach taken in the Refs. [135–137] where the authors have treated the η' mesons on the same footing as the original Golstone Bosons and included the η' in loops.

The quark mass and condensate dependent expressions of the decay constants f_π, f_K and the masses m_π, m_K and M_η^2 given by the infrared regularized U(3) ChPT [138–140] approach are described below for performing the chiral limit study in the RQM-I model. The m_π, m_K dependent scaling relations for the f_π, f_K and M_η^2 given by the large N_c standard U(3) ChPT [135–137] for performing the chiral limit study in the RQM-S model are presented in the subsection II B. The RQM-I and RQM-S model results of the chiral limit studies and Columbia plots have been compared exhaustively by varying the mass of the scalar σ meson as $m_\sigma = 400, 500$ and 600 MeV. The Columbia plots have been drawn both in the pion-kaon mass plane and the light-strange quark mass plane. The $m_\pi - m_K$ and $m_{ud} - m_s$ planes of the RQM-S model Columbia plots have been drawn also when the σ mass becomes very high as $m_\sigma = 750$ and 800 MeV. The RQM-S model results of chiral limit studies have been compared with other results available in the current literature.

1 : M_η^2 from infrared regularized U(3) ChPT inputs

The infrared regularized U(3) ChPT prescription of treating the η' meson, gives a particular expression of the M_η^2 that constitutes the main ingredient of this ChPT based parameter fixing procedure. It was proposed originally in the Ref.[69] for the linear sigma model studied in the optimized perturbation theory framework. In this approach, it is sufficient to use the $SU_L(3) \times SU_R(3)$ ChPT framework for knowing the functional forms $f_\pi(m_\pi, m_K)$ and $f_K(m_\pi, m_K)$. The One-loop ChPT calculations in the Ref. [132] give the follow-

ing expressions of $m_\pi^2, m_K^2, f_\pi, f_K$ with $\mathcal{O}(\frac{1}{f^2})$ accuracy in terms of the eight parameters $f, A, q, M_0, L_4, L_5, L_6, L_8$.

$$m_\pi^2 = 2A \left[1 + \frac{1}{f^2} \left\{ \mu_\pi - \frac{\mu_\eta}{3} + 16A(2L_8 - L_5) + 16A(2+q)(2L_6 - L_4) \right\} \right]. \quad (17)$$

$$m_K^2 = A(1+q) \left[1 + \frac{1}{f^2} \left\{ \frac{2}{3}\mu_\eta + 8A(1+q)(2L_8 - L_5) + 16A(2+q)(2L_6 - L_4) \right\} \right]. \quad (18)$$

$$f_\pi = f + \frac{1}{f} [-2\mu_\pi - \mu_K + 8AL_5 + 8A(2+q)L_4] \quad (19)$$

$$f_K = f \left[1 + \frac{1}{f^2} \left\{ -\frac{3}{4}(\mu_\pi + \mu_\eta + 2\mu_K) + 8A(2+q)L_4 + 4A(1+q)L_5 \right\} \right]. \quad (20)$$

The chiral logarithms $\mu_{\text{PS}} = \frac{m_{\text{PS}}^2}{32\pi^2} \ln(\frac{m_{\text{PS}}^2}{M_0^2})$ are evaluated at the scale M_0 in the above expressions where the leading order squared mass of the corresponding meson in the pseudo-scalar octet, is substituted for the m_{PS}^2 . One should note that the chiral constants L_i do not vary with the pseudo-scalar masses. The quark mass and quark condensate dependence of the above one-loop ChPT expressions of the m_π^2, m_K^2, f_π and f_K are governed by the parameters $q = 2m_s/(m_u + m_d) = m_s/m_{ud}$ and $A = B (m_u + m_d)/2 = Bm_{ud}$ where the chiral limit value of the quark condensate $\langle \bar{u}u \rangle$ determines the B . Inverting the Eqs. (17) and (18) to order $\mathcal{O}(\frac{1}{f^2})$ accuracy, the q and A can be expressed below in terms of the masses m_π, m_K, m_η and chiral constants L_i .

$$A = \frac{m_\pi^2}{2} \left[1 - \frac{1}{f^2} \left\{ \mu_\pi - \frac{\mu_\eta}{3} + 8m_\pi^2(2L_8 - L_5) + 8(2m_K^2 + m_\pi^2)(2L_6 - L_4) \right\} \right]. \quad (21)$$

$$q+1 = \frac{2m_K^2}{m_\pi^2} \left[1 - \frac{1}{f^2} \left\{ \mu_\eta - \mu_\pi + 8(m_K^2 - m_\pi^2)(2L_8 - L_5) \right\} \right]. \quad (22)$$

The leading order relations of the above two equations are sufficient to find the following $\mathcal{O}(\frac{1}{f^2})$ accurate m_π, m_K -dependence of the f_π, f_K from Eqs. (19) and (20).

$$f_\pi = f - \frac{1}{f} \left[2\mu_\pi + \mu_K - 4m_\pi^2(L_4 + L_5) - 8m_K^2L_4 \right]. \quad (23)$$

$$f_K = f \left[1 - \frac{1}{f^2} \left\{ \frac{3}{4}(\mu_\pi + \mu_\eta + 2\mu_K) - 4m_\pi^2L_4 - 4m_K^2(2L_4 + L_5) \right\} \right]. \quad (24)$$

With the input $f_\pi=93$ MeV, $f_K=113$ MeV, $m_\pi=138$ MeV, $m_K=495.6$ MeV, $m_\eta=547.8$ MeV and $M_0 = 4\pi f_\pi \equiv 1168$ MeV, $f=88$ MeV, one gets the constants L_4 and L_5 at the physical point as :

$$L_4 = -0.7033 \times 10^{-3}; \quad L_5 = 0.3708 \times 10^{-3}. \quad (25)$$

The values of A and q that one takes at the physical point, control the constants L_6 and L_8 . The strange to average non-strange quark mass ratio has the value $q = 24.9$ similar to the Ref.[69] as it is close to the lattice determination and compatible with the range $20 \leq q \leq 34$ indicated by the PDG listing [155]. Choosing leading order ChPT value of A in the physical point $A = A^{(0)}$ and then using the phenomenological values of m_π^2, m_K^2 with the Gell-Mann-Okubo formula for m_η^2 in the $\mathcal{O}(\frac{1}{f^2})$ accurate expressions of A and q , one gets :

$$L_6 = -0.3915 \times 10^{-3}; \quad L_8 = 0.511 \times 10^{-3}. \quad (26)$$

The values of M_0 , f and L_i can be used further for the continuation of A and q from the physical point to an arbitrary point in the $m_\pi - m_K$ plane.

One should note that the physical η and η' states are obtained from the mixtures of the states η_0 and η_8 . Apart from the values of m_π^2 and m_K^2 , one needs the numerical input for the $m_{\eta,00}^2 + m_{\eta,88}^2$ also in order to fix the quartic coupling λ_2 in the LSM/QM model [66, 82, 85, 86]. After finding the value of λ_2 , the 't Hooft cubic coupling c gets easily fixed. The experimental masses m_η and $m_{\eta'}$ are known only at the physical point. Since the numerical value of only the total sum $m_\eta^2 + m_{\eta'}^2 = m_{\eta,00}^2 + m_{\eta,88}^2 = M_\eta^2$ is required for finding the λ_2 , even if one does not know the individual values of m_η^2 (m_π, m_K) and $m_{\eta'}^2$ (m_π, m_K), the knowledge of the sum M_η^2 (m_π, m_K) as input is necessary and sufficient for fixing the λ_2 when one moves towards the chiral limit away from the physical point.

In order to find the functional form of the M_η^2 (m_π, m_K), one needs the application of the infrared regularized $U_L(3) \times U_R(3)$ ChPT that proceeds through similar steps as in the previous description but the mixing in the masses of the η_0, η_8 makes it a little involved. The Ref. [69] has given the collection of the relevant formulas spread over several papers [135, 138, 139]. The values of experimental masses $m_\eta, m_{\eta'}$ together with the choice of mixing angle $\theta_\eta = -20^0$, give the values of $m_{\eta,00}^2, m_{\eta,88}^2, m_{\eta,08}^2$ at the physical point. When the ChPT expressions of $m_{\eta,00}^2, m_{\eta,88}^2, m_{\eta,08}^2$, are made equal to their respective numerical values at the physical point, the four chiral constants $L_7, v_0^{(2)}, v_2^{(2)}, v_3^{(1)}$ appearing in those expressions, get restricted by the three relations. One should note that the constant $v_0^{(2)}$ takes into account the $U_A(1)$ anomaly contribution to the η' mass that gets determined primarily by the topological characteristics of the gluonic configurations. Hence it would be insensitive against the quark mass variations. Choosing the large N_c relation for $v_0^{(2)} = -29.3f^2$, the remaining three chiral

constants as reported in Ref. [69] are :

$$L_7 = -0.2272 \times 10^{-3}; \quad v_3^{(1)} = 0.095; \quad v_2^{(2)} = -0.1382. \quad (27)$$

The sum of Eqs. (B10) and (B11) in Ref. [69] gives the following (m_π, m_K) dependence of the M_η^2 .

$$\begin{aligned} M_\eta^2 = & 2m_K^2 - 3v_0^{(2)} + 2(2m_K^2 + m_\pi^2) \{3v_2^{(2)} - v_3^{(1)}\} + \\ & \frac{1}{f^2} \left[8v_0^{(2)}(2m_K^2 + m_\pi^2)(3L_4 + L_5) + m_\pi^2(\mu_\eta - 3\mu_\pi) \right. \\ & \left. - 4m_K^2\mu_\eta + \frac{16}{3} \left\{ (6L_8 - 3L_5 + 8L_7)(m_\pi^2 - m_K^2)^2 + \right. \right. \\ & \left. \left. 2L_6(m_\pi^4 - 2m_K^4 + m_\pi^2m_K^2) + L_7(m_\pi^2 + 2m_K^2)^2 \right\} \right] \end{aligned} \quad (28)$$

The η mass occurs at the leading order in chiral logarithm i.e. $(m_\eta^{(0)})^2 = (4m_K^2 - m_\pi^2)/3$, hence the functions $f_\pi(m_\pi, m_K)$, $f_K(m_\pi, m_K)$ and $M_\eta^2(m_\pi, m_K)$ are applicable only when $4m_K^2 > m_\pi^2$. Eqs.(28) together with the Eqs.(23) and (24) enable the calculation of the RQM/QM model couplings λ_2, c, m^2 and λ_1 in the $m_\pi - m_K$ plane.

The chiral symmetry breaking strengths for the chiral limit studies are reduced by reducing the m_π and m_K away from the physical point. The results obtained in the $m_\pi - m_K$ plane can be mapped to the corresponding results in the light-strange quark mass $m_{us} - m_s$ plane after using the Eqs. (21) and (22) whose multiplication gives $\mathcal{O}(1/f^2)$ expression of $A(q+1) = B(m_s + m_{ud})$ in terms of the π, K masses and chiral constants. The constant B gets determined from the Eq. (21) for the $m_\pi = 138$ MeV as $A = B m_{ud}$ after taking the $m_{ud} = 4$ MeV at the physical point. The quark masses away from the physical point can be evaluated easily after knowing the constant B and the Columbia plot in the $m_{ud} - m_s$ plane can be drawn.

B. f_π, f_K, m_π, m_K and M_η^2 from large N_c U(3) ChPT

The large N_c standard U(3) ChPT prescription as described in the Refs. [136, 137] gives the following expressions of the pion, kaon decay constants and masses f_π, f_K and m_π^2, m_K^2 .

$$f_\pi = f \left(1 + 4 \frac{L_5}{f^2} m_\pi^2 \right). \quad (29)$$

$$f_K = f \left(1 + 4 \frac{L_5}{f^2} m_K^2 \right). \quad (30)$$

$$m_\pi^2 = 2 m_{ud} B \left[1 + \frac{16 m_{ud} B}{f^2} (2L_8 - L_5) \right]. \quad (31)$$

$$m_K^2 = m_{ud} B (1+q) \left[1 + \frac{8 m_{ud} B}{f^2} (1+q)(2L_8 - L_5) \right] \quad (32)$$

Note that only the dominant low energy constants L_5 and L_8 are appearing in the above expressions as they are the $\mathcal{O}(N_c)$ while the other constants $L_{4,6,7}$ are sub leading and hence suppressed in the large N_c standard U(3) ChPT. The chiral limit value of the quark condensate $\langle \bar{u}u \rangle$ is used to fix the parameters $q = m_s/m_{ud}$ and B . Taking $f_\pi = 93$ MeV with $f_K = 1.223 f_\pi$ and using Eqs. (29) and (30) for the physical $m_\pi = 138$ MeV and $m_K = 496$ MeV, one finds $f = 91.2599$ MeV and $L_5 = 2.084659 \times 10^{-3}$. The expressions of the octet η_8 and singlet η_0 masses [136, 137] are written as the following.

$$m_{88}^2 = \frac{(4m_K^2 - m_\pi^2)}{3} + \frac{4}{3}(m_K^2 - m_\pi^2)\Delta_M . \quad (33)$$

$$m_{00}^2 = \frac{(2m_K^2 + m_\pi^2)}{3}(1 - 2\Delta_N) + \frac{2}{3}(m_K^2 - m_\pi^2)\Delta_M - 3v_{02} . \quad (34)$$

$$\Delta_M = \frac{8}{f^2}(m_K^2 - m_\pi^2)(2L_8 - L_5) . \quad (35)$$

$$\Delta_N = 3v_{31} - \frac{12}{f^2}v_{02}L_5 . \quad (36)$$

$$M_\eta^2 = m_{00}^2 + m_{88}^2 = 2m_K^2 - \frac{2}{3}(m_K^2 - m_\pi^2)y + 2(m_K^2 - m_\pi^2)\Delta_M - \frac{2}{3}(2m_K^2 + m_\pi^2)\Delta_N \quad (37)$$

The $\frac{2(m_K^2 - m_\pi^2)}{3}y = 3v_{02}$ in Eq.(37) defines y . The η' mass $m_{\eta'}^2 = (M_\eta^2 - m_\eta^2)$ with the following mass for physical η .

$$m_\eta^2 = m_K^2 - \frac{(m_K^2 - m_\pi^2)}{3}[y + (\sqrt{9 + 2y + y^2})] + \Delta_M (m_K^2 - m_\pi^2)\left(1 - \frac{9 + y}{3\sqrt{9 + 2y + y^2}}\right) - \frac{\Delta_N}{3}\left\{2m_K^2 + m_\pi^2 - \frac{3(2m_K^2 - 3m_\pi^2) - y(2m_K^2 + m_\pi^2)}{\sqrt{9 + 2y + y^2}}\right\} \quad (38)$$

The five parameters v_{02}, v_{31}, L_8 together with the quark mass parameters $m_{ud}B$ and q can be expressed in terms of five independent observables $m_\pi, m_K, m_\eta, m_{\eta'}$ and the $\eta - \eta'$ mixing angle θ . Thus large N_c ChPT is not predictive at this level. In order to get predictions from the large N_c ChPT, Ref. [136] imposed that $\mathcal{O}(\delta)$ corrections are not too large so that the large N_c expansion makes sense [137]. Keeping the mixing angle in the range $20^\circ < \theta < 24^\circ$, the Ref.[136] gives the following range of

the parameters fit for the physical observables.

$$0.980 \leq \frac{2m_{ud}B}{m_\pi^2} \leq 0.988 ,$$

$$18.3 \leq (q - 1) \leq 20.9$$

$$26 \leq \frac{-v_{02}}{f^2} \leq 29 ,$$

$$-0.164 \leq v_{31} \leq -0.161 ,$$

$$1.35 \times 10^{-3} \leq L_8 \leq 1.57 \times 10^{-3} \quad (39)$$

The experimental masses $m_\eta = 547.5$ MeV and $m_{\eta'} = 957.78$ MeV give $M_\eta = (\sqrt{m_\eta^2 + m_{\eta'}^2}) = 1103.22$ MeV. With this same numerical value of the M_η , when the pole masses $m_\eta = 528.48$ MeV and $m_{\eta'} = 968.41$ MeV are used as input in the RQM model (With the f_π, f_K as above) for calculating the η, η' self energy corrections and the renormalized parameters, the same pole masses for the η and η' are reproduced in the output after adding the corresponding self energy corrections to their respective masses calculated from the new set of renormalized parameters. For getting the $M_\eta = 1103.22$ MeV at the physical point from the ChPT expression given in the Eq.(37), one finds the following numerical values of the U(3) ChPT parameters.

$$L_8 = 1.44 \times 10^{-3}, v_{31} = -0.1637 \text{ and } v_{02} = -29.1f^2(40)$$

It is important to note that with the above set of parameter values at the physical point, the ChPT expressions in Eqs. (38) and (37) give the η and η' masses as $m_\eta = 527.82$ MeV and $m_{\eta'} = 968.77$ which are almost same as the corresponding masses obtained in the RQM model. Note that the QM model parameters give $m_\eta = 538.96$ MeV and $m_{\eta'} = 962.62$ MeV in the output when the $M_\eta = 1103.22$ MeV at the physical point.

One can find the light and strange quark masses corresponding to the reduced masses of pions and kaons from the Eqs.(31) and (32). Solving the quadratic Eq.(31) and taking the positive root, one gets $m_{ud}B$ whose value for the $m_\pi = 138$ MeV will give the constant B if one takes $m_{ud} = 4$ MeV at the physical point. The positive root of the quadratic Eq.(32) gives numerical values of $Bm_{ud}(q + 1) = B(m_{ud} + m_s)$ for different kaon masses. Thus knowing B , One can know the m_{ud} and m_s for different values of the m_π and m_K as one moves away from the physical point in the Columbia plot.

III. RESULTS AND DISCUSSION

The RQM model [126, 127] whose parameters are renormalized on-shell after the proper treatment of the quark one-loop vacuum fluctuation, got refined very recently into a valuable tool of chiral limit studies by enriching the model with the chiral perturbation theory

TABLE I. Chiral limit is approached by defining the reduced π , K meson starred masses as $\frac{m_\pi^*}{m_\pi} = \frac{m_K^*}{m_K} = \beta \leq 1$ such that $\frac{m_\pi^*}{m_K^*} = \frac{m_\pi}{m_K}$ where $m_\pi = 138$ and $m_K = 496$ MeV at the physical point [82]. The f_π , f_K for any β in the RQM-S model using the large N_c standard U(3) ChPT, are obtained by putting the corresponding m_π^* , m_K^* in the Eq. (29) and Eq. (30). The parameters and chiral constants of the standard U(3) ChPT at the physical point which reproduce the experimental M_η :Expt=1103.22 MeV corresponding to the experimental values $(m_\eta, m_{\eta'}) = (547.5, 957.8)$ MeV, give the $(m_\eta, m_{\eta'}) = (527.82, 968.77)$ MeV from the Eqs.(37) and (38) for the input set S. The Eq. (23) and Eq. (24) with the m_π^* , m_K^* for any β , give the corresponding f_π , f_K for the infrared regularized U(3) ChPT input set I where the corresponding M_η gets calculated using the Eq. (28). The infrared regularized U(3) ChPT expression in the Eq. (28) gives M_η -I=1035.55 MeV for the physical m_π , m_K . The RQM model parameters $\lambda_{20}, c_0, \lambda_{10}, m_0^2, h_{x0}^*$ and h_{y0}^* for the physical point $\beta = 1$ and critical end point ratio β_{CEP} , are presented for both the ChPT input sets S and I when the $m_\sigma = 400, 500$ and 600 MeV and only the input set S when the $m_\sigma = 750$ and 800 MeV.

m_σ	$\frac{m_\pi^*}{m_\pi} = \frac{m_K^*}{m_K} = \beta$	f_π (MeV)	f_K (MeV)	M_η (MeV)	λ_{20}	c_0 (MeV)	λ_{10}	m_0^2 (MeV 2)	h_{x0}^* (MeV 3)	h_{y0}^* (MeV 3)
400	1(S)	93.0	113.7389	1103.22	33.522	7330.557	1.907	$(443.341)^2$	$(119.804)^3$	$(323.531)^3$
	1(I)	92.9737	113.2635	1035.55	35.47	7390.50	1.27	$(447.71)^2$	$(119.79)^3$	$(324.39)^3$
	$\beta_{\text{CEP}}=0.38738$ (S)	91.521	94.6332	889.14	31.148	8056.86	7.225	$(175.035)^2$	$(63.859)^3$	$(167.657)^3$
	$\beta_{\text{CEP}}=0.37963$ (I)	91.571	97.915	846.25	-24.468	7828.558	25.119	$(159.898)^2$	$(63.019)^3$	$(163.679)^3$
500	1(S)	93.0	113.7389	1103.22	33.522	7330.557	4.072	$(397.817)^2$	$(119.804)^3$	$(323.531)^3$
	1(I)	92.9737	113.2635	1035.55	35.47	7390.50	3.46	$(402.433)^2$	$(119.79)^3$	$(324.39)^3$
	$\beta_{\text{CEP}}=0.37665$ (S)	91.507	94.449	887.13	31.05	8069.107	10.541	$-(114.749)^2$	$(62.676)^3$	$(164.468)^3$
	$\beta_{\text{CEP}}=0.37159$ (I)	91.481	97.632	845.21	-25.271	7836.42	28.372	$-(125.371)^2$	$(62.11)^3$	$(161.307)^3$
600	1(S)	93.0	113.7389	1103.22	33.522	7330.557	9.0398	$(265.265)^2$	$(119.804)^3$	$(323.531)^3$
	1(I)	92.9737	113.2635	1035.55	35.47	7390.50	8.46	$(272.31)^2$	$(119.79)^3$	$(324.39)^3$
	$\beta_{\text{CEP}}=0.33634$ (S)	91.457	93.8028	880.12	30.689	8112.955	17.512	$-(322.909)^2$	$(58.126)^3$	$(152.253)^3$
	$\beta_{\text{CEP}}=0.32445$ (I)	90.946	95.985	839.74	-30.081	7880.442	37.757	$-(345.951)^2$	$(56.646)^3$	$(147.077)^3$
750	1(S)	93.0	113.7389	1103.22	33.522	7330.557	24.492	$-(540.551)^2$	$(119.804)^3$	$(323.531)^3$
	$\beta_{\text{CEP}}=0.25013$ (S)	91.369	92.666	867.82	-30.081	8193.523	33.834	$-(558.347)^2$	$(47.720)^3$	$(124.582)^3$
800	1(S)	93.0	113.7389	1103.22	33.522	7330.557	29.826	$-(545.342)^2$	$(119.804)^3$	$(323.531)^3$
	$\beta_{\text{CEP}}=0.23316$ (S)	91.354	92.482	865.83	29.86	8207.002	37.957	$-(602.887)^2$	$(45.538)^3$	$(118.818)^3$

(ChPT) inputs for finding the model parameters away from the physical point [128, 129]. The $\mathcal{O}(\frac{1}{f^2})$ accurate results of the infrared regularized U(3) ChPT [69, 138–141], as the input set I are used for the (m_π, m_K) dependence of the f_π, f_K and M_η^2 and the first, second order and crossover chiral transition regions in the Columbia plot are computed in the RQM-I model for the $m_\sigma = 400$ and 530 MeV. The large N_c standard U(3) ChPT scaling relations for the (m_π, m_K) dependence of the f_π, f_K and M_η^2 [132–137], termed here as the input set S, have also been used in the Ref. [128] for fixing the RQM model parameters away from the physical point and computing the Columbia plot in the RQM-S model when the $m_\sigma = 530$ MeV in the presence of $U_A(1)$ anomaly. The enrichment of the RQM model with the ChPT inputs, cures the problem of the loss of the spontaneous chiral symmetry breaking (SCSB) for the mass range $m_\sigma = 400 – 800$ MeV when the $m_\pi, m_K \rightarrow 0$ in the often used method [64, 66, 82, 92, 93, 99] of chiral limit studies in the QM model called the fixed-ultraviolet (UV) scheme [35] where the light (strange) explicit chiral symmetry breaking strengths $h_x(h_y)$ are changed while all other parameters are kept same as the ones at the physical point. The chiral limit in the fixed UV scheme can be explored only for very large $m_\sigma \geq 800$ MeV when the mass parameter m^2 turns negative to

get the SCSB. The nonperturbative FRG study of Resch et.al. [35] under the local potential approximation (LPA) circumvented the above problem by proposing the ChPT motivated fixed- f_π scheme where the initial effective action is heuristically adjusted to larger scales ($\Lambda' > \Lambda$) for every smaller mass point in the path to the chiral limit such that the f_π always retains its physical value and the SCSB is not lost for the mass range $m_\sigma = 400 – 600$ MeV. The change in parameters (which are kept same as at the physical point) gets compensated by changing the scale ($\Lambda' > \Lambda$) of the initial action when the explicit chiral symmetry breaking strengths h_x and h_y decrease. The fixed f_π scheme suffers from the problem of a heuristic determination of the initial effective action, even though it is physically reasonable. Furthermore the FRG flow allows for the scalar σ masses only in the range $m_\sigma \in [400, 600]$ MeV [35]. In contrast to the above, the RQM model parameter fixing with the ChPT inputs is free from any ambiguity and heuristic adjustment as the π, K meson masses are reduced to perform chiral limit study away from the physical point.

The Columbia plots in the presence of the $U_A(1)$ anomaly were computed in the RQM model using the two ChPT input sets I and S only for the case of $m_\sigma = 530$ MeV in the Ref. [128], so that the results can be compared for checking the consistency of chiral

limit study. One gets slightly larger first order region in the RQM-S model. The RQM-I and S model tricritical lines, demarcating the first and second order regions in the $\mu - m_K$ plane at $m_\pi = 0$, are almost overlapping for the $m_K < 450$ MeV. But the real difference emerges for the $m_K > 450$ MeV when the tricritical line obtained from the large N_c standard U(3) ChPT input set S shows saturation for the range $m_K = 450 - 550$ MeV as its slope becomes zero in the range $m_K = 520.0 - 550.0$ MeV in which the chemical potential stays almost constant at $\mu = 234.8$ MeV while the tricritical line for the infrared regularized input set I does not show saturation as its average slope increases to 0.1566 when it goes from the point ($m_K = 500.0, \mu = 235.79$) MeV to the ($m_K = 550.0, \mu = 243.62$) MeV. The proper saturation trend shown by the tricritical line in the $\mu - m_K$ plane of the RQM-S model Columbia plot for larger m_K is an improvement over the corresponding result obtained in the RQM-I model because the tricritical line is expected to be connected to the tricritical point of the two-flavor chiral limit [35, 142] at some higher value of m_K . The above discussion, prompts us to compute the Columbia plots in the RQM-S model for different $m_\sigma = 400, 500$ and 600 MeV and compare them with the existing (for the $m_\sigma = 400$ MeV in [129]) and to be computed RQM-I model Columbia plots for the $m_\sigma = 500$ and 600 MeV. Bringing out similarities and differences in the RQM-S and RQM-I model Columbia plots for different values of the m_σ in the range 400-600 MeV, the present work aims to know if the large N_c standard U(3) ChPT scaling relations for the (m_π, m_K) dependence of the f_π, f_K and M_η^2 , constitute an improved and better prescription for Chiral limit studies. It is well known that the strength of the first order chiral transition diminishes for larger m_σ and the critical end point $_{\text{CEP}}$ disappears from the entire $\mu - T$ plane as the chiral transition becomes crossover all over the phase diagram computed for the physical point parameters when the $m_\sigma > 600$ MeV [126]. In order to see how the first order regions get reduced when the second order chiral transition regions of the $\mu - m_K$ plane (at $m_\pi = 0$) and the chiral crossover transition regions of the $m_\pi - m_K$ plane (at $\mu = 0$), are expanding in response to the increasing σ meson mass, the Columbia plots will be computed and discussed below also for the $m_\sigma = 750$ and 800 MeV in the RQM-S model. We will compute, discuss and compare the light-strange quark mass $m_{ud} - m_s$ planes (at $\mu = 0$) and the $\mu - m_s$ planes (at $m_{ud} = 0$) of the Columbia plots also when the $m_\sigma = 400, 500, 600$ MeV in both the RQM-S as well as the RQM-I models and the $m_\sigma = 750$ and 800 MeV in the RQM-S model. The complete comparative perspective of the critical quantities obtained in the $\mu - m_K$ ($\mu - m_s$) and $m_\pi - m_K$ ($m_{ud} - m_s$) planes of the Columbia plots of different model scenarios over the whole range of scalar σ meson mass $m_\sigma = 400 - 800$ MeV together with the relevant LQCD study results (with references) will be presented in a tabular form.

Note that since the on-shell renormalization of pa-

rameters in the RQM model, gives rise to a significantly stronger axial $U_A(1)$ anomaly and a reduced strange as well as non-strange direction explicit chiral symmetry breaking strengths h_x and h_y , the softening effect of the quark one-loop vacuum fluctuation on the strength of the chiral transition is moderate in the RQM model [126, 127]. Therefore one finds a noticeably large first order regions in the $\mu - m_K$ ($\mu - m_s$) and $m_\pi - m_K$ ($m_{ud} - m_s$) planes of the RQM-S model Columbia plots for the $m_\sigma = 530$ MeV as reported recently in the Ref. [128]. In contrast to the above the corresponding first order regions are significantly smaller in the Columbia plots of the curvature mass based parametrized quark meson with vacuum term (QMVT) model [129] and the e-MFA FRG QM model work for the $m_\sigma = 530$ MeV [35] due to very large softening influence of the quark one-loop vacuum fluctuation on the strength of the chiral transition. The $U_A(1)$ anomaly strength c and $h_x(h_y)$ do not change in the QMVT model and the e-MFA FRG work as they are using curvature meson masses to fix the model parameters. It will also be interesting to compare the smaller extents of the first order regions that one finds due to the very strong smoothing effect of the quark one-loop vacuum correction in the QMVT model and the e-MFA FRG QM model Columbia plots for the $m_\sigma = 530$ MeV [35, 129] with the first order regions of the RQM-S model Columbia plots (for larger m_σ) which become smaller due to the effect of increasing the mass of the σ meson to $m_\sigma = 600, 750$ and 800 MeV. The three important critical quantities to be computed in the Columbia plots are 1) the tricritical points ($_{\text{TCP}}$) m_K^{TCP} (m_s^{TCP}) at $\mu = 0$ and also in the $\mu - m_K$ ($\mu - m_s$) plane for the light chiral limit $m_\pi = 0 = m_{ud}$, 2) the pion (light quark) critical mass m_π^c (m_{ud}^c) beyond which the chiral transition is a smooth crossover on the three flavor SU(3) symmetric chiral limit line ($m_\pi = m_K$ i.e. $m_{ud} = m_s$) in the $m_\pi - m_K$ ($m_{ud} - m_s$) plane and 3) the pion (light quark) terminal mass m_π^t (m_{ud}^t) at which the chiral critical line of Z(2) critical points, terminates on the strange chiral limit line $h_y = 0$ ($m_s = 0$) in the $m_\pi - m_K$ ($m_{ud} - m_s$) plane at $\mu = 0$. The tricritical point is defined by that kaon (s quark) mass m_K^{TCP} (m_s^{TCP}) at which the second order chiral phase transition becomes first order.

The $h_{x0} = 0$ in the Eq. (13) defines the light chiral limit for the RQM model whereas the $h_{y0} = 0$ in Eq. (14) gives the strange chiral limit line. The RQM model parameters $\lambda_{20}, c_0, \lambda_{10}, m_0^2$ corresponding to the reduced chiral symmetry breaking strengths h_{x0}^* and h_{y0}^* for performing the chiral limit study are calculated using the input sets of two different prescriptions of the ChPT. The reduced light and strange chiral symmetry breaking strengths for the QM model are given by $h_x^* = (m_\pi^*)^2 f_\pi$ and $h_y^* = \{\sqrt{2} f_K (m_K^*)^2 - \frac{f_\pi}{\sqrt{2}} (m_\pi^*)^2\}$. The RQM model reduced strengths are defined as : $h_{x0}^* = (m_{\pi,c}^*)^2 f_\pi$ and $h_{y0}^* = \{\sqrt{2} f_K (m_{K,c}^*)^2 - \frac{f_\pi}{\sqrt{2}} (m_{\pi,c}^*)^2\}$ where the reduced pion, kaon curvature masses $m_{\pi,c}^*$ and $m_{K,c}^*$ are found by putting the reduced pion, kaon mass m_π^* and m_K^* values

respectively in the expressions Eq. (15) and Eq. (16). The (m_π, m_K) dependence of the f_π, f_K and M_η^2 for the input set I of the infrared regularized U(3) ChPT prescription described in the section(II A-I), are calculated by substituting the reduced pion, kaon masses m_π^* and m_K^* respectively in the Eq. (23), Eq. (24) and Eq.(28). After substituting the reduced masses m_π^* and m_K^* respectively in the Eq. (29), Eq. (30) and Eq.(37), one finds the (m_π, m_K) dependence of the f_π, f_K and M_η^2 for the input set S of the large N_c standard U(3) ChPT framework given in the section(II A-II). The m_π^* and m_K^* defined by reducing the π and K masses in a fixed ratio. i.e. $\frac{m_\pi^*}{m_\pi} = \frac{m_K^*}{m_K} = \beta$, provides us a direct path from the physical point to the chiral limit by tuning only the fraction β instead of changing both the m_π and m_K randomly. The $\frac{m_\pi^*}{m_K^*}$ always remains equal to the fixed physical point ratio $\frac{m_\pi}{m_K}$ [82]. The fraction β of the above choice, also facilitates the comparison of our results with those of the Refs. [35, 82]. The RQM model with the input set I and S has been termed respectively as the RQM-I and RQM-S model whose parameters $\lambda_{20}, c_0, \lambda_{10}, m_0^2, h_{x0}, h_{y0}$ for the f_π, f_K, M_η corresponding to the physical point ratio $\beta = 1$ (where $(m_\pi, m_K) = (138, 496)$ MeV) and the critical end point ratio β_{CEP} when the $m_\sigma = 400, 500$ and 600 MeV are presented in the Table I. The RQM-S model parameters for the $\beta = 1$ and β_{CEP} when $m_\sigma = 750$ and 800 MeV, are also presented in the Table I. The critical end point ratio β_{CEP} is that fraction of π and K mass at which the chiral crossover transition, in the $m_\pi - m_K$ plane (at $\mu = 0$), becomes first order.

Using the $M_\eta = \sqrt{(m_\eta^2 + m_{\eta'}^2)} = 1103.22$ MeV (termed as M_η : Expt) for the experimental masses $(m_\eta, m_{\eta'}) = (547.5, 957.8)$ MeV with the f_π and f_K at $\beta = 1$ of the input set I in the Table I for the input, the renormalized parameters of the RQM-I model give $(m_\eta, m_{\eta'}) = (527.82, 968.76)$ MeV in the output. One finds a slightly smaller value of the $M_\eta = 1035.55$ MeV from the ChPT expression in Eq.(28) for the input set I at the physical point and with this M_η in the input, the RQM-I model give $(m_\eta, m_{\eta'}) = (520.62, 895.17)$ MeV in the output. Values taken from the prescribed range for the parameters and chiral constants of the large N_c standard U(3) ChPT in the Refs. [136, 137] as given in the section (II A-II), reproduce the experimental M_η : Expt=1103.22 MeV at the physical point for the input set S. The M_η : Expt=1103.22 MeV with the f_π, f_K for $\beta = 1$ from the input set S, give the $(m_\eta, m_{\eta'}) = (527.82, 968.77)$ MeV from the standard U(3) ChPT expressions Eqs. (37) and (38) whereas the corresponding RQM model calculation gives almost the same $(m_\eta, m_{\eta'}) = (528.48, 968.41)$ MeV. The above computations are consistent as the calculated M_η from the $(m_\eta, m_{\eta'})$ values obtained in the output of all the RQM-S(I) model calculations is the same as in the input.

A. Comparing temperature variations of the π and σ curvature masses at $\beta = 1, \beta_{\text{CEP}}$ in RQM-S(I) model for $m_\sigma = 400, 500, 600, 750$ and 800 MeV.

The chiral limit study has been performed in the above described set up of the RQM-S and RQM-I model framework. The explicit chiral symmetry breaking strengths h_{x0}^* and h_{y0}^* in the non-strange and strange directions are systematically decreased by reducing the pion and kaon masses when the ratio β is tuned to smaller fractions. The temperature variations of the light and strange condensates x and y when β is reduced from 1 for different $m_\sigma = 400, 500, 600, 750$ and 800 MeV, have similar pattern as shown for the RQM-I and S models in the Ref. [128] for the case of $m_\sigma = 530$ MeV. Becoming sharper in response to the decreasing β , the physical point chiral crossover transition turns second order at the Z_2 critical point fraction β_{CEP} for reduced CEP masses $m_{\pi,\text{CEP}}$ and $m_{K,\text{CEP}}$. For $\beta < \beta_{\text{CEP}}$, one gets the first order chiral phase transition which becomes successively stronger when β approaches zero in the chiral limit where the masses of the octet mesons π, K and η become zero [128, 129].

The chiral transition is analyzed also by studying the temperature variations of the masses of σ and π mesons which are the chiral partners. When the chiral crossover transition turns second order, the effective potential flattens in the σ direction and the associated critical σ mode becomes massless. Hence if the temperature variation of the scalar mass m_σ , hits zero on the temperature axis, one confirms the identification of the critical end point (cep). The correlation length $\xi = 1/m_\sigma$ diverges at the CEP when mass of the critical mode $m_\sigma \rightarrow 0$. The Ref. [35] has discussed that when only the chiral symmetry breaking source strengths j_x and j_y in the light and strange directions are reduced for performing the chiral limit study in the fixed UV scheme whereas the other parameter values of the model are kept fixed as at the physical point, the critical sigma mode mass m_σ increases and the corresponding correlation length ξ decreases to such an extent that the spontaneous chiral symmetry breaking (SCSB) gets lost. They proposed the ChPT motivated fixed- f_π scheme as a remedy of the above problem and performed the chiral limit study by heuristically adjusting the initial effective action to the larger scales ($\Lambda' > \Lambda$) when the symmetry breaking source strengths j_x and j_y , are reduced for smaller (m_π, m_K) such that the f_π remains fixed to its physical value and the SCSB is not lost when the $m_\sigma = 400 - 600$ MeV. The change in parameters (which are kept same as at the physical point) for the smaller explicit chiral symmetry breaking source strengths, are compensated by changing the scale ($\Lambda' > \Lambda$).

When the f_π, f_K, M_η and all the model parameters change according to the (m_π, m_K) dependent scaling relations provided by the large N_c standard U(3) ChPT and the infrared regularized U(3) ChPT prescriptions respectively in the RQM-S and RQM-I model, the con-

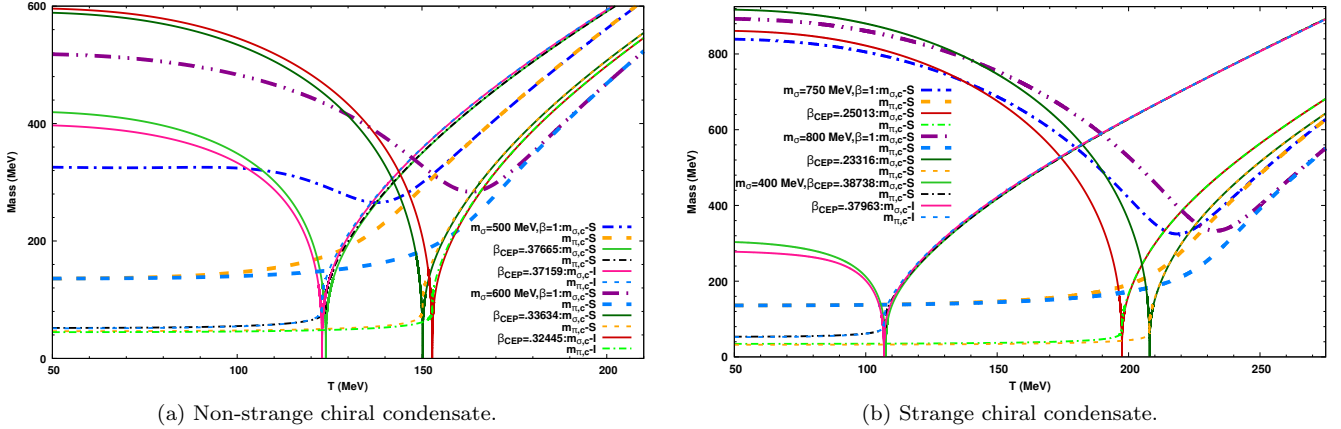


FIG. 1. The curvature masses of the π and σ mesons in the RQM model when its parameters are fixed using the large N_c standard U(3) ChPT inputs (the infrared regularized U(3) ChPT inputs) are termed as $m_{\pi,c} - S(I)$ and $m_{\sigma,c} - S(I)$. The temperature variations of the $m_{\pi,c} - S$ and $m_{\sigma,c} - S$ for both the physical point $\beta = 1$ and the β_{CEP} together with the $m_{\pi,c} - I$ and $m_{\sigma,c} - I$ temperature variations for the β_{CEP} at $\mu = 0$ when the $m_\sigma = 500$ and 600 MeV, are presented in the left panel (a). The right panel (b) shows the $\mu = 0$ temperature variations of the $m_{\pi,c} - S$ and $m_{\sigma,c} - S$ for the physical point $\beta = 1$ and β_{CEP} when the $m_\sigma = 750$ and 800 MeV. The $m_{\pi,c} - S(I)$ and $m_{\sigma,c} - S(I)$ temperature variations for the β_{CEP} when $m_\sigma = 400$ MeV are also plotted in the right panel where $\mu = 0$. The fraction $\beta = \frac{m_\pi^*}{m_\pi} = \frac{m_K^*}{m_K}$.

sistent chiral limit study can be performed without any loss of SCSB in our work. Here it is relevant to point out that the FRG flow allows for the scalar σ masses only in the range $m_\sigma \in [400, 600]$ MeV [35] while the chiral limit study can be accurately performed over the complete range of $m_\sigma = 400 - 800$ MeV in our RQM-S model work. Comparing the Columbia plots of the RQM-S model and RQM-I model for different m_σ in the range 400-600 MeV, it will be shown later that RQM-S model gives better and refined results. Therefore the plots of temperature variations of the σ , π curvature masses $m_{\sigma,c}$ and $m_{\pi,c}$ have been shown in the Fig. 1. The plots of $m_{\sigma,c}$ and $m_{\pi,c}$ in the RQM-S model for $\beta = 1$ and β_{CEP} and RQM-I model for β_{CEP} are presented in the Fig. 1(a) where $m_\sigma = 500$ and 600 MeV. The Fig. 1(b) presents the $m_{\sigma,c}$ and $m_{\pi,c}$ temperature plots for the RQM-S model at the physical point as well as β_{CEP} when $m_\sigma = 750$ and 800 MeV and the RQM-S and I models at β_{CEP} when $m_\sigma = 400$ MeV. Since the temperature variations of the $m_{\sigma,c}$ and $m_{\pi,c}$ in the RQM-S model overlap with the corresponding temperature plots in the RQM-I model at the physical point, the Fig. 1(a) shows the $\beta = 1$ temperature plots of the $(m_{\sigma,c}, m_{\pi,c})$ only for the RQM-S model when $m_\sigma = 500, 600$ MeV while the $(m_{\sigma,c}, m_{\pi,c})$ temperature variations at $\beta = 1$ for $m_\sigma = 400$ MeV, are not shown in the Fig. 1(b) for either the RQM-S or the RQM-I model. The temperature plots of the $m_{\sigma,c}$ and $m_{\pi,c}$ in the Fig. 1(a) and Fig. 1(b) become degenerate in the chiral symmetry restored phase after the chiral transition.

It is worth pointing out that the σ meson vacuum curvature mass $m_{\sigma,c}$ for all the cases of m_σ in both the RQM-S and RQM-I models, is lowest at the physical point. When the temperature variations of the $m_{\sigma,c}$

at the β_{CEP} are compared with those for the physical point $\beta = 1$ in both the RQM-S and I models, one finds noticeably larger values of the $m_{\sigma,c}$ in the beginning of their temperature variations for the $\beta = \beta_{CEP}$ in the Fig. 1(a) and Fig. 1(b). Successively increasing in the path to the chiral limit when the (m_π, m_K) are reduced by the fraction β , the $m_{\sigma,c}$ becomes highest when the chiral limit is reached (not shown here, it can be seen in the Ref. [129]). The above pattern is opposite of what one finds in the e-MFA-FRG:QM model study for the $m_\sigma = 530$ MeV in the Ref. [35] where the σ mass in the Fig. 2(c) goes through a significant successive decrease when the chiral limit is approached by decreasing the source strengths j_x and j_y successively by the fractions $\alpha = \sqrt{\beta} = 1.0, 0.17, 0.04$ and 0 and correspondingly adjusting the initial effective action (to start the FRG flow) successively to the higher scales $\Lambda = 700, 1000, 1100$ and 1143 MeV. Furthermore the $m_{\sigma,c}$ temperature variations of the RQM-S model for $m_\sigma = 400$ and 500 MeV respectively in the Fig. 1(b) and Fig. 1(a), are lying above the corresponding temperature variations of the RQM-I model. The above trend gets reversed in the Fig. 1(a) for the case of $m_\sigma = 600$ MeV where the RQM-S model $m_{\sigma,c}$ temperature plot lies below that of the RQM-I model. This behavior gets explained when one notes that the β_{CEP} for the RQM-I model is slightly smaller than the β_{CEP} of the RQM-S model when the $m_\sigma = 400$ and 500 MeV and this difference becomes noticeably larger for the $m_\sigma = 600$ MeV.

For the $m_\sigma = 400$ MeV, the crossover transition terminates at the second order Z_2 critical point masses $(m_{\pi,CEP}^*, m_{K,CEP}^*) = (53.46, 192.14)$ MeV for the β_{CEP} ratio $\beta_{CEP}|_{(m_\sigma=400 \text{ MeV:RQM-S})} = 0.38738$ in the RQM-S

model and $(m_{\pi, \text{CEP}}^*, m_{K, \text{CEP}}^*) = (52.39, 188.30)$ MeV for the CEP ratio $\beta_{\text{CEP}}|_{(m_\sigma=400 \text{ MeV:RQM-I})} = 0.37963$ in the RQM-I model. When the $m_\sigma = 500$ MeV, one finds a reduced set of masses for the second order Z_2 critical point at $(m_{\pi, \text{CEP}}^*, m_{K, \text{CEP}}^*) = (51.98, 186.82)$ MeV for the CEP ratio $\beta_{\text{CEP}}|_{(m_\sigma=500 \text{ MeV:RQM-S})} = 0.37665$ in the RQM-S model and $(m_{\pi, \text{CEP}}^*, m_{K, \text{CEP}}^*) = (51.33, 184.49)$ MeV for the CEP ratio $\beta_{\text{CEP}}|_{(m_\sigma=500 \text{ MeV:RQM-I})} = 0.37159$ in the RQM-I model. The critical end point masses for the $m_\sigma = 600$ MeV are obtained at the $(m_{\pi, \text{CEP}}^*, m_{K, \text{CEP}}^*) = (46.41, 166.82)$ MeV for the CEP ratio $\beta_{\text{CEP}}|_{(m_\sigma=600 \text{ MeV:RQM-S})} = 0.33634$ in the RQM-S model and the $(m_{\pi, \text{CEP}}^*, m_{K, \text{CEP}}^*) = (44.77, 160.93)$ MeV for the CEP ratio $\beta_{\text{CEP}}|_{(m_\sigma=600 \text{ MeV:RQM-I})} = 0.32445$ in the RQM-I model. One finds that for all the σ masses $m_\sigma = 400, 500$ and 600 MeV the RQM-S model CEP ratio is larger than the CEP ratio of the RQM-I model i.e. $\beta_{\text{CEP}}|_{(m_\sigma=400, 500 \text{ and } 600 \text{ MeV:RQM-S})} > \beta_{\text{CEP}}|_{(m_\sigma=400, 500 \text{ and } 600 \text{ MeV:RQM-I})}$. It is worth emphasizing that when the chiral limit study results obtained in the RQM-S model are compared with the corresponding results found in the RQM-I model, one finds that the use of the large N_c standard $U(3)$ ChPT input set S, generates a stronger approach towards the first order chiral transition as the chiral crossover transition turns second order and then first order transition is obtained for $\beta < \beta_{\text{CEP}}$ by a comparatively smaller reduction in the masses of π and K mesons. Note that since $\beta_{\text{CEP}}|_{(m_\sigma=400 \text{ MeV:RQM-S(I)})} > \beta_{\text{CEP}}|_{(m_\sigma=500 \text{ MeV:RQM-S(I)})} > \beta_{\text{CEP}}|_{(m_\sigma=600 \text{ MeV:RQM-S(I)})}$, the expected pattern gets confirmed that lower values of the σ meson mass in both the RQM-S and I model scenarios give rise to a stronger first order chiral transition whose strength become successively weaker for the higher m_σ . Further the $\{\beta_{\text{CEP}}|_{(m_\sigma=400 \text{ MeV})} - \beta_{\text{CEP}}|_{(m_\sigma=500 \text{ MeV})}\} < \{\beta_{\text{CEP}}|_{(m_\sigma=500 \text{ MeV})} - \beta_{\text{CEP}}|_{(m_\sigma=600 \text{ MeV})}\}$ indicates that the chiral transition strength becomes only marginally weak when $m_\sigma = 400 \rightarrow 500$ MeV whereas it gets significantly weaker when $m_\sigma = 500 \rightarrow 600$ MeV.

For a large $m_\sigma = 750$ MeV in the RQM-S model, one finds the critical end point masses as the $(m_{\pi, \text{CEP}}^*, m_{K, \text{CEP}}^*) = (34.52, 124.06)$ MeV for the CEP ratio $\beta_{\text{CEP}}|_{(m_\sigma=750 \text{ MeV:RQM-S})} = 0.25013$. When the σ mass becomes very large $m_\sigma = 800$ MeV, the second order Z_2 critical point masses become significantly small as $(m_{\pi, \text{CEP}}^*, m_{K, \text{CEP}}^*) = (32.18, 115.65)$ MeV for the smallest CEP ratio of $\beta_{\text{CEP}}|_{(m_\sigma=800 \text{ MeV:RQM-S})} = 0.23316$. Here it would be appropriate to compare our results in the RQM-S model with the e-MFA:QM model work of Ref. [35] where the parameter α in their study is related to the β in our work as the $\beta = \sqrt{\alpha}$. The second order Z_2 critical point in the e-MFA:QM model study for the $m_\sigma = 530$ MeV is obtained for a significantly smaller $\beta_{\text{CEP}}|_{(m_\sigma=530 \text{ MeV:e-MFA:FRG})} = \sqrt{\alpha_c} = 0.2$ which corresponds to quite small pion and kaon masses $(m_{\pi, \text{CEP}}^*, m_{K, \text{CEP}}^*) = (27.6, 99.2)$ MeV. Thus

even when the chiral transition gets strongly softened and diluted due to a very high σ mass ($m_\sigma = 800$ MeV) in the RQM-S model, its strength remains stronger than the strength of chiral transition in the e-MFA:QM model [35] and the curvature mass based parametrized QMVT model [129] study for the moderate $m_\sigma = 530$ MeV because $\beta_{\text{CEP}}|_{(m_\sigma=800 \text{ MeV:RQM-S})} > \beta_{\text{CEP}}|_{(m_\sigma=530 \text{ MeV:e-MFA:FRG})} \sim \beta_{\text{CEP}}|_{(m_\sigma=530 \text{ MeV:QMVT})}$. The diluted strength of the chiral transition in response to the increase of σ meson masses in the RQM-S model can be gauged from the β_{CEP} values which change from $\beta_{\text{CEP}}|_{(m_\sigma=530 \text{ MeV:RQM-S})} = 0.36778$ [128] to $\beta_{\text{CEP}}|_{(m_\sigma=800 \text{ MeV:RQM-S})} = 0.23316$ when the $m_\sigma = 530 \rightarrow 800$ MeV. The softening of the chiral phase transition due to the effect of quark one-loop vacuum fluctuations is quite moderate in our RQM model studies whether one uses the ChPT input set S or I. On account of the very large softening effect of the quark one-loop vacuum correction in the e-MFA:QM model work in the Ref. [35] and the curvature mass based parametrized QMVT model study in the Ref. [129], one finds significantly smaller regions or range of parameters in which the first order chiral transition occurs. For having the complete picture of the results, one should also look at the QM model results obtained after neglecting the Dirac's sea contribution under the s-MFA and taking the $m_\sigma = 800$ MeV such that the SCSB does not get lost in the work of Ref. [82] where the Fig. (9) shows that the chiral crossover transition terminates at the second order transition for a significantly larger ratio $\beta_{\text{CEP}} = .488$ that corresponds to noticeably larger π and K masses $(m_{\pi, \text{CEP}}^*, m_{K, \text{CEP}}^*) = (67.34, 242.05)$ MeV. The Table (II) presents an exhaustive comparison of the results of the RQM-S and RQM-I model for the $m_\sigma = 400, 500$ and 600 MeV and the RQM-S model for the $m_\sigma = 750$ and 800 MeV in the present work. The results of the RQM-S model study in Ref. [128], the e-MFA:QM model FRG study in Ref. [35] and the QMVT model study in Ref. [129] for the $m_\sigma = 530$ MeV, are also shown. The results of s-MFA QM model study in Ref [82] for $m_\sigma = 800$ MeV and different Lattice QCD results with proper references are also presented in the Table (II).

B. Comparison of RQM-S and I model Columbia plots for $m_\sigma = 400, 500, 600$ MeV and the RQM-S model plot description for $m_\sigma = 750, 800$ MeV.

One needs to implement different conditions, other than simply reducing the m_π and m_K by tuning the only one parameter β , for computing different regions of the Columbia plot. The tricritical line is defined as the locus of tricritical points in the vertical $\mu - m_K$ plane where the second order chiral phase transition ends to become the first order transition. This line is computed by implementing the condition of light chiral limit ($m_\pi = 0 \implies h_{x0} = 0$). The $Z(2)$ critical end points

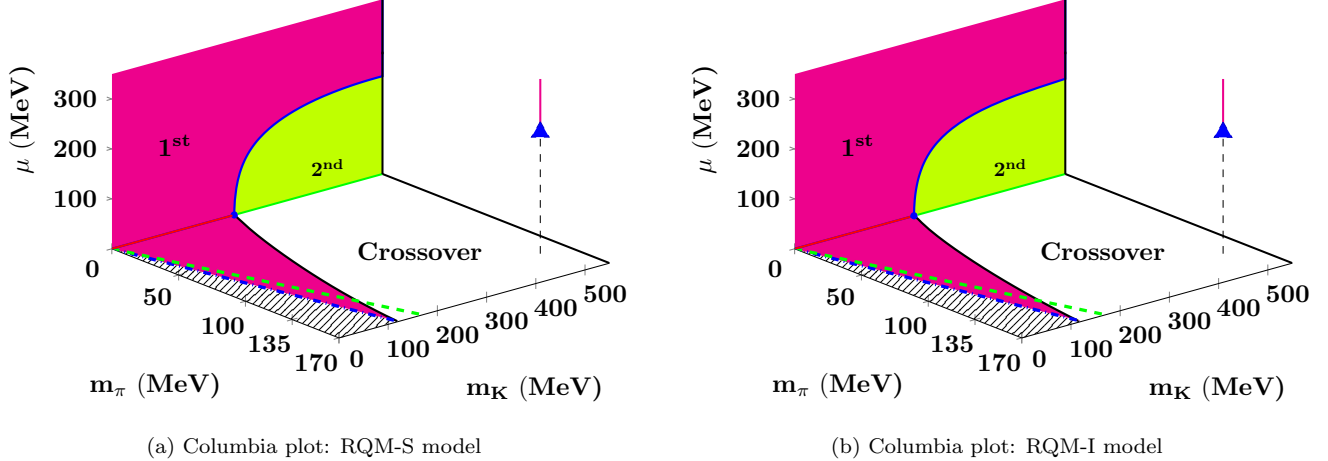


FIG. 2. The chiral transitions for the $m_\pi = 0$ and $\mu = 0$ are depicted respectively in the $\mu - m_K$ and $m_\pi - m_K$ plane. The results for the RQM-S model when its parameters are fixed using the large N_c standard $U(3)$ ChPT inputs, are presented in the left panel (a) whereas the right panel (b) shows the results for the RQM-I model where its parameters are fixed using the infrared regularized $U(3)$ ChPT inputs. The second order $Z(2)$ critical line in solid black color that separates the crossover from the first order transition region in the Fig.(a) and (b), intersects the $m_\pi = m_K$ green dash line respectively at the critical pion mass $m_\pi^c = 134.51$ and $m_\pi^c = 134.16$ MeV and it terminates respectively at the terminal pion mass $m_\pi^t = 169.25$ and $m_\pi^t = 168.39$ MeV. Solid blue line of the tricritical points which starts respectively at the blue dot $m_K^{TCP} = 248.8$ and $m_K^{TCP} = 242.6$ MeV in the Fig.(a) and (b), separates the second and first order regions. The h_{y0} is negative in the dashed area below the dash dot blue line for the strange chiral limit $h_{y0} = 0$. The black dashed vertical line at the physical point in the Fig(a) and (b), shows the crossover transition which ends at the critical end point in blue triangle and the solid red line shows the first order transition. The scalar σ mass $m_\sigma = 400$ MeV.

$(_{CEP})$ are located after fixing the $m_{\pi,CEP}$ and finding the corresponding $m_{K,CEP}$ at which the crossover transition for the $m_K > m_{K,CEP}$, turns second order to become first order for the $m_K < m_{K,CEP}$. Demarcating the first order transition from the crossover transition regions, the chiral critical line is constituted by the critical end points in the horizontal $m_\pi - m_K$ plane at the $\mu = 0$. This line has been depicted by the solid black line in the figures to follow. The implementation of strange chiral limit $h_{y0} = 0 = h_y$ condition, gives the blue dash dotted lines in the figures below. The strange direction chiral symmetry breaking strength h_y is negative in the shaded regions of the figures. The $SU(3)$ symmetric chiral limit lines for the $m_\pi = m_K$, are plotted by the green dash line in the figures below.

The s-MFA QM model study, where the quark one-loop vacuum term is dropped, shows first order chiral transition in the light chiral limit ($m_\pi = 0$) independent of the value of m_K and the strength of the $U_A(1)$ anomaly [82]. Confirming the predictions of the Ref. [20], the Chiral phase transition for the light chiral limit turns out to be second order when the $m_K \geq 496$ MeV due to the effect of the quark one-loop vacuum fluctuations in the present RQM-S and I model work as in the e-MFA:FRG QM model [35] or the QMVT model [129] studies. The second order chiral phase transition that occurs on the points of the m_K axis in the light chiral limit for $m_K < 496$ MeV, belongs to the $O(4)$ universality class. This $O(4)$ second order line terminates at the tri-

critical point m_K^{TCP} where the transition turns first order and becomes stronger till the chiral limit is reached when $m_K = 0$. The tricritical point m_K^{TCP} is marked by the blue dot in the figures below. The solid black color chiral critical line terminates on the strange chiral limit line at the terminal pion mass m_π^t beyond which the transition is a smooth crossover everywhere in the $m_\pi - m_K$ plane. The intersection point of the $SU(3)$ symmetric $m_\pi = m_K$ chiral limit path depicted by the green dash line with the chiral critical line in the solid black color, gives the critical pion mass m_π^c where the boundary of first order region ends in the $m_\pi - m_K$ plane.

The identification of the $_{TCP}$ at m_K^{TCP} , serves the two fold quantitative measure. The maximum extent of the first order transition region below the crossover region in the horizontal $m_\pi - m_K$ plane of the Columbia plot at $\mu = 0$ and the minimum extent of the first order above the second order transition region in the vertical $\mu - m_K$ plane of the Columbia plot at $m_\pi = 0$, both are quantified by the numerical value m_K^{TCP} of the $_{TCP}$. The terminal pion mass m_π^t quantifies the maximum spread of the first order transition on the m_π axis between the crossover region above and the unphysical $h_y = 0$ region below it while the critical pion mass m_π^c serves as the quantifying measure of the maximum spread of the first order transition region on the m_π axis covered between the crossover region above and the $SU(3)$ symmetric $m_\pi = m_K$ chiral limit line below it in the horizontal $m_\pi - m_K$ plane of the Columbia plot at $\mu = 0$. The set of critical quantities

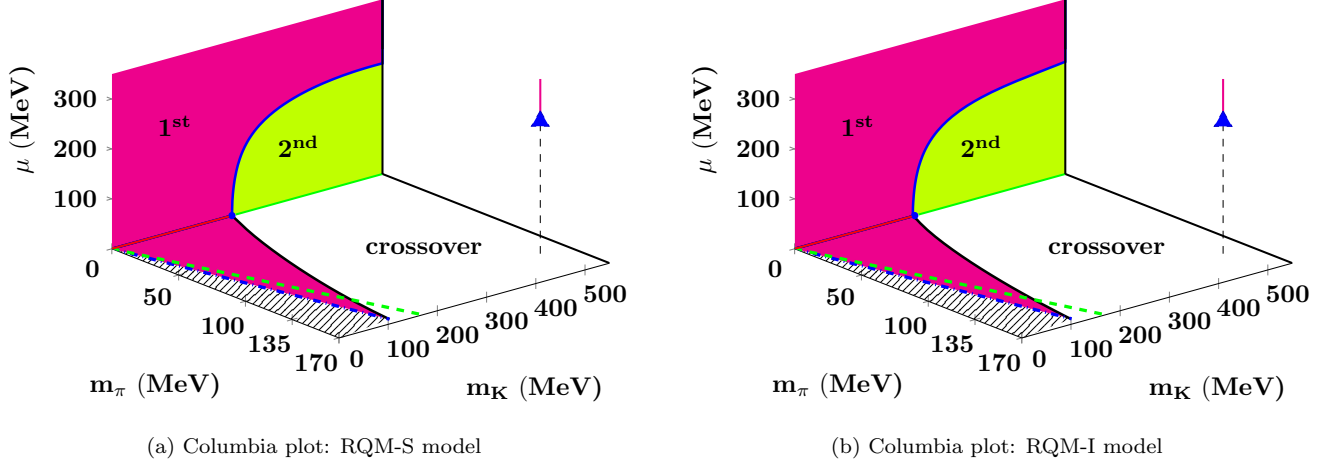


FIG. 3. The chiral transitions in the $\mu - m_K$ plane for the $m_\pi = 0$ and the $m_\pi - m_K$ plane for the $\mu = 0$ when the $m_\sigma = 500$ MeV are presented in the left panel (a) for the RQM-S model and the right panel (b) for the RQM-I model. The points, lines, crossover, first and second order chiral transition regions and features are defined similar to the Fig.(2). The critical quantities (m_K^{TCP} , m_π^t , m_π^c) in the RQM-S and RQM-I model are (244.1, 164.65, 130.71) MeV and (240.1, 164.02, 130.84) MeV in respective order.

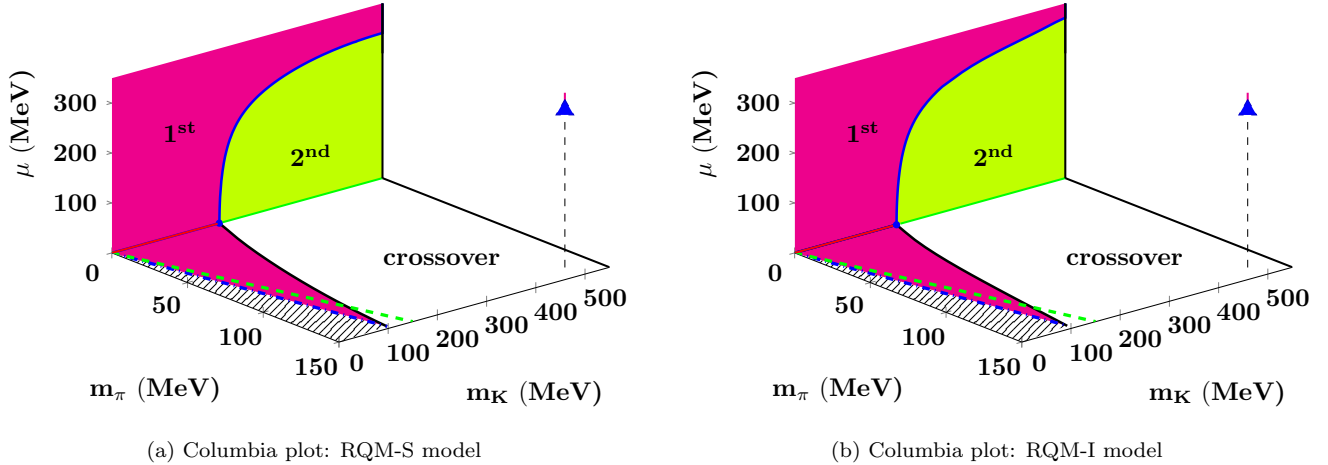


FIG. 4. Chiral transitions in the $\mu - m_K$ plane at $m_\pi = 0$ and the $m_\pi - m_K$ plane at $\mu = 0$ for the $m_\sigma = 600$ MeV, are presented in the left panel (a) for the RQM-S model and the right panel (b) for the RQM-I model. The points, lines, crossover, first and second order chiral transition regions and features are defined similar to the Fig.(2). The critical quantities (m_K^{TCP} , m_π^t , m_π^c) are respectively (218.5, 147.66, 117.26) MeV and (207.05, 146.35, 118.01) MeV in the RQM-S and RQM-I model.

$(m_K^{\text{TCP}}, m_\pi^t, m_\pi^c) \equiv (248.8, 169.25, 134.51)$ MeV in the Fig. 2(a) and $(m_K^{\text{TCP}}, m_\pi^t, m_\pi^c) \equiv (242.6, 168.39, 134.16)$ MeV in the Fig. 2(b) obtained respectively in the RQM-S model and RQM-I model computations, signify the largest spread of the first order regions in both the horizontal and vertical planes of the Columbia plots for the respective model scenarios when the scalar σ meson mass is taken as the $m_\sigma = 400$ MeV. Note that the extent of the first order regions in the vertical and horizontal planes of the Columbia plot are slightly larger in the RQM-S model than what is obtained in the corresponding RQM-I model computations. When

the scalar σ meson mass is sequentially increased to $m_\sigma = 500$ and 600 MeV, the sets of the critical quantities are obtained respectively as $(m_K^{\text{TCP}}, m_\pi^t, m_\pi^c) \equiv (244.1, 164.65, 130.71) \{(240.1, 164.02, 130.84)\}$ MeV in the Fig. 3(a) {Fig. 3(b)} and $(m_K^{\text{TCP}}, m_\pi^t, m_\pi^c) \equiv (218.5, 147.66, 117.26) \{(207.05, 146.35, 118.01)\}$ MeV in the Fig. 4(a) {Fig. 4(b)} for the RQM-S model {RQM-I model}. On increasing the m_σ from $400 \rightarrow 500$ MeV, the first order regions in the $m_\pi - m_K$ and $\mu - m_K$ planes of Columbia plots get slightly reduced as indicated by the marginal reduction of the critical quantities by $(\Delta m_K^{\text{TCP}}, \Delta m_\pi^t, \Delta m_\pi^c) \equiv (4.7, 4.6, 3.8)$ MeV

in the RQM-S model and $(\Delta m_K^{\text{TCP}}, \Delta m_\pi^t, \Delta m_\pi^c) \equiv (2.5, 4.37, 3.32)$ MeV in the RQM-I model. When the m_σ changes from $500 \rightarrow 600$ MeV, the ability to produce the first order transition over the large regions in the $m_\pi - m_K$ and $\mu - m_K$ planes of the RQM-S and I model Columbia plots, gets noticeably compromised in comparison to the case of $m_\sigma = 400 \rightarrow 500$. One finds moderate but noteworthy reduction of $(\Delta m_K^{\text{TCP}}, \Delta m_\pi^t, \Delta m_\pi^c) \equiv (25.6, 16.99, 13.45)$ MeV for the critical quantities computed in the RQM-S model while the RQM-I model critical quantities suffer from a larger reduction of $(\Delta m_K^{\text{TCP}}, \Delta m_\pi^t, \Delta m_\pi^c) \equiv (33.05, 17.67, 12.83)$ MeV when the m_σ goes from the $500 \rightarrow 600$ MeV. In comparison to the RQM-S Columbia plot in the Fig. 4(a), the horizontal ($m_\pi - m_K$) and vertical ($\mu - m_K$) planes, show distinctly smaller regions of the first order chiral transition in the Fig. 4(b) for the RQM-I Columbia plot when the $m_\sigma = 600$ MeV.

The first order region near the chiral limit in the $\mu - m_K$ plane at the $m_\pi = 0$, which is very large when the $m_\sigma = 400$ and 500 MeV respectively in the Fig. 2(a) (Fig. 2(b)) and Fig. 3(a) (Fig. 3(b)) and though smaller but still large when the $m_\sigma = 600$ MeV in the Fig. 4(a) (Fig. 4(b)) for the RQM-S model (RQM-I model), increases when the chemical potential μ is increased. The tricritical points chiral line lying below the first order and above the second order region, starts at $\mu = 0$ from the $m_K^{\text{TCP}} = 248.8(242.6)$ MeV with a large positive slope in the Fig. 2(a) (Fig. 2(b)) for the RQM-S (RQM-I) model when the $m_\sigma = 400$ MeV and its successively decreasing positive slope for the larger μ and m_K , gradually approaches zero showing good saturation (near saturation) for the $m_K > 500$ MeV. The μ rises from $191.12(184.7) \rightarrow 195.09(188.25)$ MeV on the tricritical line of the Fig. 2(a) (Fig. 2(b)) when the m_K goes from $450 \rightarrow 500$ MeV in the RQM-S (RQM-I) model giving 0.079 (0.071) as its slope which becomes very small to $.016$ (small to 0.049) when the $\mu = 195.09(188.25)$ MeV at $m_K = 500$ MeV becomes $\mu = 195.91(190.7)$ MeV at $m_K = 550$ MeV. Since the slope of the RQM-S model tricritical line in the Fig. 2(a) becomes zero in the range $m_K = 530$ to 550 MeV where μ remains constant as $\mu = 195.91$ MeV, it shows better saturation than the tricritical line of the RQM-I model in the Fig. 2(b). On increasing the σ mass to the $m_\sigma = 500$ MeV, the RQM-S (RQM-I) model tricritical line starting with large positive slope from the $m_K^{\text{TCP}} = 244.1(240.1)$ MeV at $\mu = 0$ in the Fig. 3(a) (Fig. 3(b)) shows (does not show) the saturation pattern like the one that we get for the $m_\sigma = 400$ MeV in the RQM-S (RQM-I) model. The slope $0.1634(0.168)$ between the points $(\mu, m_K) = (209.11, 400.0)\{(204.6, 400.0)\}$ MeV and $(\mu, m_K) = (217.28, 450.0)\{(213.0, 450.0)\}$ MeV on the tricritical line of the RQM-S (RQM-I) model in the Fig. 3(a) (Fig. 3(b)), decreases to the $0.0764(0.1222)$ when one goes from the point $(\mu, m_K) = (217.28, 450.0)\{(213.0, 450.0)\}$ MeV to the point $(\mu, m_K) = (221.1, 500.0)\{(219.11, 500.0)\}$ MeV and it becomes $0.011(0.1158)$ between the point

$(\mu, m_K) = (221.1, 500.0)\{(219.11, 500.0)\}$ and $(\mu, m_K) = (221.65, 550.0)\{(224.9, 550.0)\}$ MeV. With the zero slope for the range $m_K = 520$ to 550 MeV where μ is very close to the constant $\mu = 221.7$ MeV, the RQM-S model tricritical line saturates properly. The RQM-I model tricritical line does not show saturation having a noticeable non-zero slope 0.1158 close to $m_K = 550$ MeV.

When the m_σ is increased to 600 MeV, the RQM-S model tricritical line that begins in the Fig. 4(a) with large positive slope from the $m_K^{\text{TCP}} = 218.5$ MeV at $\mu = 0$, repeats the saturation trend that one observes in the RQM-S model for the case of $m_\sigma = 400$ and 500 MeV respectively in the Fig. 2(a) and 3(a). The RQM-S model tricritical line slope 0.1864 in the Fig. 4(a) between the points $(\mu, m_K) = (274.13, 400.0)$ and $(283.45, 450.0)$ MeV decreases noticeably to 0.1042 when the (μ, m_K) shifts from the point $(283.45, 450.0) \rightarrow (288.66, 500.0)$ MeV and the slope becomes very small to 0.0408 when the μ changes from $288.66 \rightarrow 290.7$ MeV corresponding to the shift of m_K from $500 \rightarrow 550$ MeV. The RQM-S model tricritical line shows proper saturation as its slope 0.01 is negligible in the range $m_K = 530$ to 550 MeV where $\mu = 290.2 \rightarrow 290.7$ MeV. In complete contrast to the RQM-S model, the tricritical line of the RQM-I model, that starts in the Fig. 4(b) with large positive slope from a noticeably smaller $m_K^{\text{TCP}} = 207.05$ MeV at $\mu = 0$, not only does not show the saturation trend but it becomes distinctly and significantly divergent for the $m_K > 400$ MeV. The quite large slope 0.229 of the RQM-I model tricritical line between the points $(\mu, m_K) = (287.82, 400.0)$ MeV and $(299.27, 450.0)$ MeV in the Fig. 4(b), decreases only marginally to 0.2188 when one goes from the point $(\mu, m_K) = (299.27, 450.0) \rightarrow (310.21, 500.0)$ MeV and the slope increases again to 0.2228 when the μ changes from $310.21 \rightarrow 321.35$ MeV for the increasing m_K from $500 \rightarrow 550$ MeV.

Here, it is relevant to point out the comparison of RQM-S and RQM-I model Columbia plots as reported recently in Ref [128] for the case of $m_\sigma = 530$ MeV. The use of input set M_η -I and the input set M_η -II in the Ref [128] for performing the chiral limit study, has been termed in the present study as the RQM-I model and the RQM-S model. The tricritical lines in the $\mu - m_K$ plane of the RQM-I and RQM-S model Columbia plots, start respectively from the $m_K^{\text{TCP}} = 235.7$ MeV in the Fig.(4a) and $m_K^{\text{TCP}} = 239.58$ MeV in the Fig.(5) of the Ref. [128]. The RQM-I and RQM-S model tricritical lines, are almost overlapping for the $m_K < 450$ MeV. Showing noticeable difference after the $m_K \geq 450$, the RQM-S model tricritical line shows saturation for the range $m_K = 450 - 550$ MeV while the RQM-I model tricritical line turns somewhat divergent. The RQM-S model tricritical line has the slope of only 0.078 in going from the point $(m_K, \mu) = (450.0, 230.22) \rightarrow (500.0, 234.12)$ MeV whereas the slope 0.1478 of the RQM-I model tricritical line between the point $(m_K, \mu) = (450.0, 228.4)$ MeV and $(500.0, 235.79)$ MeV, is nearly double of the above slope of the RQM-S model line. The slope of RQM-I model

line slightly increases to 0.1566 when it moves from the point $(m_K, \mu) = (500.0, 235.79) \rightarrow (550.0, 243.62)$ MeV whereas the decreasing average slope between the point $(m_K, \mu) = (500.0, 234.12)$ and $(550.0, 234.8)$ MeV is only 0.0136 for the RQM-S model tricritical line whose slope turns zero in the range $m_K = 520.0 - 550.0$ MeV as the chemical potential is almost constant at $\mu = 234.8$ MeV in this range. Thus the divergence that was observed in the Ref. [128] for the RQM-I model tricritical line for the case of $m_\sigma = 530$ MeV, becomes noticeable and distinctly large divergence when the m_σ becomes 600 MeV as discussed in the last paragraph.

The large initial positive slope at the beginning of the tricritical lines of the RQM-S and RQM-I model respectively in the Fig. 2(a), 3(a), 4(a), and the Fig. 2(b), 3(b), 4(b), is consequence of the fact that the chiral critical surface, in the three dimensions of the $m_\pi - m_K - \mu$ for the RQM model set up, has a positive curvature whose intersection with the $\mu - m_K$ plane at the $m_\pi = 0$, gives the tricritical line. The chiral critical lines of the $Z(2)$ critical end points which make the chiral critical surface, are its intersection with the $\mu - m_K$ planes for different $m_\pi \neq 0$. Due to its positive curvature [156], when the chiral critical surface intersects the dashed black vertical line for the chiral crossover transition at the physical point, the existence of a critical end point gets marked by a solid blue arrow in the Figs. (2),(3) and (4). The physical point $_{\text{CEP}}$ for the $m_\sigma = 400, 500$ and 600 MeV, lies respectively at the successively higher $\mu_{\text{CEP}} = 243.77, 265.62$ and 315.85 MeV in the Fig. 2(a), 3(a) and 4(a) for the RQM-S model and $\mu_{\text{CEP}} = 243.29, 265.3$ and 315.74 MeV in the Fig. 2(b), 3(b) and 4(b) for the RQM-I model. With nearly similar shape for the $m_\sigma = 400$ MeV, the RQM-S and RQM-I model chiral critical surfaces are positioned in comparatively lower chemical potential ranges where the tricritical lines in the $\mu - m_K$ plane of both the models, show the similar saturation pattern after $m_K > 400$ MeV, though the saturation behavior of the RQM-I model tricritical line is somewhat approximate. While shifting to the higher chemical potentials for the $m_\sigma = 500$ and 530 MeV, the chiral critical surface for the RQM-I model gets lifted to relatively higher μ near $(m_\pi = 0, m_K > 400$ MeV) as its tricritical line picks up the diverging trend after the $m_K > 400$ MeV while the RQM-S model chiral critical surface gets lifted up evenly in the μ direction since its tricritical line shows the consistent saturation pattern after the $m_K > 400$ MeV.

It is worth emphasizing that even though the RQM-S and RQM-I model $_{\text{CEP}}$ coordinates, for the physical point and $m_\sigma = 600$ MeV, respectively at the $(\mu_{\text{CEP}}, T_{\text{CEP}}) = (315.85, 21.96)$ and $(315.74, 22.1)$ MeV have almost no difference, the RQM-I model chiral critical line at the physical point is part of such a chiral critical surface that gets a noticeably larger μ direction lift up in the vicinity of the $(m_\pi = 0, m_K > 400$ MeV) in its overall positioning at significantly higher μ . The above mentioned tilting in the critical surface, ends up giving the

RQM-I model tricritical line that diverges significantly after the $m_K > 400$ MeV in the $\mu - m_K$ plane at $m_\pi = 0$ whereas the chiral critical surface of the RQM-S model has a proper evenly lifted up shape in the μ direction since it connects its chiral critical line at the physical point to the tricritical line which shows the expected saturation pattern for the $m_K > 400$ MeV in the $\mu - m_K$ plane at the $m_\pi = 0$. Note that the saturation behavior for the tricritical line in the $\mu - m_K$ plane (for whatever be the value of m_σ), is consistent and desirable on the physical grounds as the 2+1 flavor tricritical line is expected to be connected to the tricritical point of the two flavor chiral limit [142] at some higher value of the μ and m_K . Therefore it is reasonable to conclude that when one uses the large N_c standard U(3) ChPT scaling relations to determine the (m_π, m_K) dependence of the f_π, f_K and M_η^2 away from the physical point, the RQM-S model gives the improved and more refined results for the chiral limit studies for all values of the σ mass in the range 400-600 MeV.

The Columbia plots are drawn after increasing the m_σ successively to the 400, 500 and 600 MeV in order to see how the shifting critical end points present in the $\mu - T$ plane of the RQM model phase diagrams for the physical point parameters [126, 127], are associated with and influenced by the change in the chiral critical surface and the tricritical line for the light chiral limit. The chiral crossover transition line gets extended and the first order chiral transition line shrinks in the $\mu - T$ plane when the σ mass m_σ increases and the position of the $_{\text{CEP}}$ shifts to the right lower corner of the phase diagrams. The strength of the chiral transition becomes so weak that it turns crossover everywhere in the $\mu - T$ plane and the $_{\text{CEP}}$ altogether disappears from the phase diagrams for the physical point when the $m_\sigma > 600$ MeV. Since the RQM-S model gives better and accurate results for the chiral limit studies, it is worthwhile to draw the Columbia plots for the $m_\sigma = 750$ and 800 MeV. It will be interesting to compute the tricritical line for $m_\pi = 0$ in the $\mu - m_K$ plane for the $m_\sigma = 750$ MeV. The above tricritical line will give us a picture of shrinkage in the shape of the chiral critical surface that exists only for a small range of the $m_\pi - m_K$ and terminates well before the $m_\pi = 138$ MeV, hence does not have any chiral critical line that lies above the physical point on its other end since the chiral transition is crossover all over.

Even when the strength of chiral transition is significantly weaker for the large $m_\sigma = 750$ MeV in the RQM-S model Columbia plot of the Fig. 5(a), the corresponding critical quantities $(m_K^{\text{TCP}}, m_\pi^t, m_\pi^c) \equiv (159.85, 110.40, 87.90)$ MeV, are comparable to the critical quantities $(m_K^{\text{TCP}}, m_\pi^t, m_\pi^c) \equiv (169, 110, 86)$ MeV obtained for the $m_\sigma = 530$ MeV in the e-MFA QM model study done after switching off the quantum and thermal fluctuations of the mesons in the FRG framework of the Ref.[35]. The extent of the first order region in the horizontal $m_\pi - m_K$ plane of the Fig. 5(a), is similar to the area of the first order region seen in the $m_\pi - m_K$

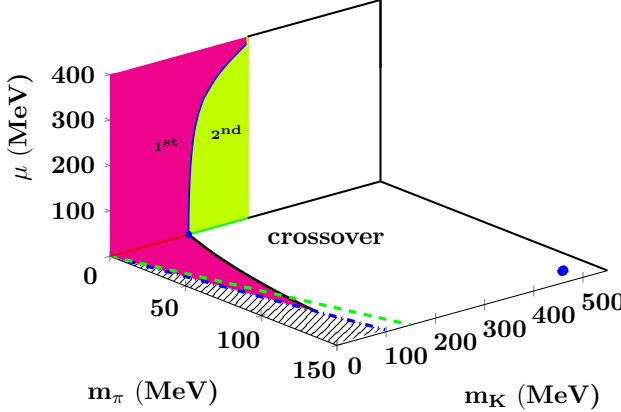
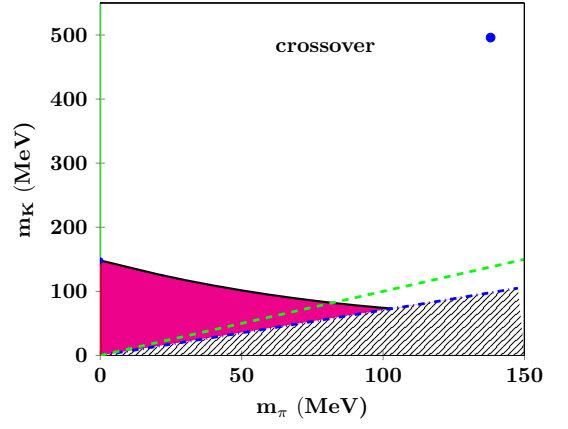
(a) Columbia plot: RQM-S model for $m_\sigma = 750$ MeV(b) Columbia plot: RQM-S model for $m_\sigma = 800$ MeV

FIG. 5. The left panel (a) depicts the RQM-S model chiral transition in the horizontal plane $m_\pi - m_K$ at $\mu = 0$ and the vertical $\mu - m_K$ plane at $m_\pi = 0$ when the $m_\sigma = 750$ MeV. The horizontal plane $m_\pi - m_K$ at $\mu = 0$ in the right panel (b) presents the chiral transition in RQM-S model for the case of $m_\sigma = 800$ MeV. The points, lines, crossover, first and second order chiral transition regions and features are defined similar to the Fig.(2). The tricritical line demarcating the first and second order colored regions, is computed only upto the point $(m_K, \mu) = (280, 386.8)$ MeV in the Fig. (a) because the chemical potential becomes very high for a significantly smaller kaon mass in the $\mu - m_K$ plane. The RQM-S model critical quantities $(m_K^{TCP}, m_\pi^t, m_\pi^c)$ are respectively $(159.85, 110.40, 87.90)$ MeV and $(148.2, 103.19, 82.07)$ MeV when $m_\sigma = 750$ and 800 MeV.

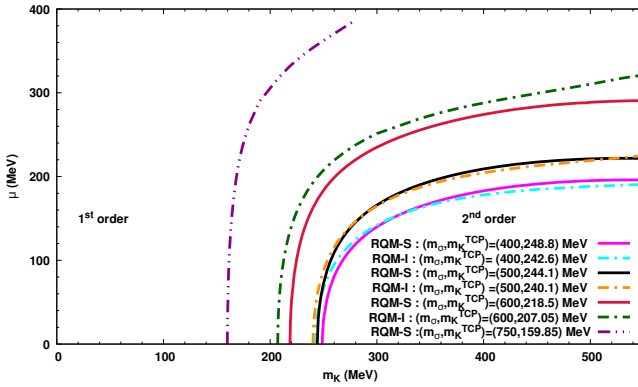
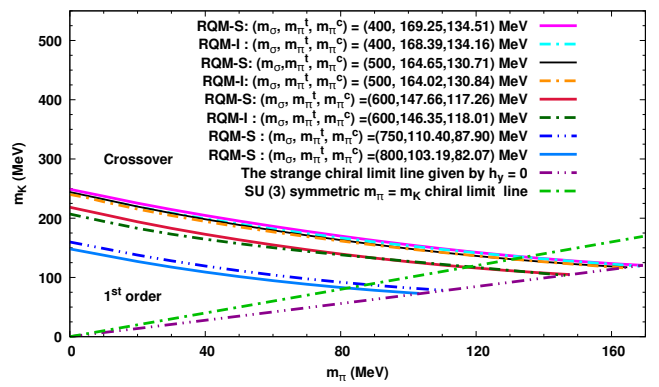
(a) Vertical plane $\mu - m_K$ for $m_\sigma = 400, 500, 600$ and 750 MeV(b) Horizontal plane $m_\pi - m_K$ for $m_\sigma = 400, 500, 600, 750, 800$ MeV

FIG. 6. Left panel (a) (Right panel (b)) presents the comparison of lines and regions in the vertical $\mu - m_K$, $m_\pi = 0$ (horizontal $m_\pi - m_K$, $\mu = 0$) planes of the three dimensional RQM-S and RQM-I model Columbia plots for the $m_\sigma = 400, 500, 600, 750$ and 800 MeV in the Fig. (2(a)), (2(b)), (3(a)), (3(b)), (4(a)), (4(b)) and (5(a)), (5(b)). RQM-S and RQM-I model tricritical lines for the $m_\sigma = 400, 500, 600$ and 750 MeV, as marked and explained in the Fig.(a), start from the m_K^{TCP} on the m_K axis and demarcate the first order region above them on their left hand side from the second order region below them on their right hand side. RQM-S and RQM-I model Z(2) critical lines for the $m_\sigma = 400, 500, 600, 750$ and 800 MeV, as marked and explained in the Fig.(b), separating the crossover transition region above them from the first order region that lies below, intersect the SU(3) symmetric $m_\pi = m_K$ chiral limit line at the critical pion mass m_π^c and terminate on the strange chiral limit line satisfying the $h_{y0} = 0$, at the terminal pion mass m_π^t .

plane of the Fig.(3a) in the Ref. [35] but the tricritical line in the vertical $\mu - m_K$ plane of the e-MFA:FRG QM model Columbia plot shows proper saturation while the corresponding tricritical line for the RQM-S model when $m_\sigma = 750$ is strongly divergent. The tricritical line in the vertical $\mu - m_K$ plane begins from a smaller $m_K^{TCP} = 159.85$ MeV at $m_\pi = 0$ in the Fig. 5(a) with

a very large positive slope but it shows a very large divergence and a smaller bending because the chemical potential becomes very high $\mu = 386.8$ MeV for a significantly smaller kaon mass $m_K = 280$ MeV. Thus the chiral critical surface can be constructed only for the range $m_K^{TCP} = 159.85 \rightarrow m_K = 280$ MeV on the m_K axis and the range $m_\pi = 0 \rightarrow m_\pi^t = 110.4$ MeV on the m_π

axis. The quite smaller and shrunk chiral critical surface would lie far from the region that could have possibly covered the physical point for some non-zero temperature and a large chemical potential, hence one does not find any critical end point $_{\text{CEP}}$ in the $\mu - T$ plane of the RQM-S model for physical point when the $m_\sigma = 750$ MeV. Since the tricritical lines in the $m_\pi = 0$ vertical $\mu - m_K$ planes of the RQM-S model Columbia plots for the $m_\sigma = 400, 500$ and 600 MeV show consistent and proper saturation trend, the other end of the corresponding chiral critical surfaces contain the chiral critical lines which pass over and cover the physical point, hence the corresponding $_{\text{CEP}}$ exists. One finds a very large reduction of $(\Delta m_K^{\text{TCP}}, \Delta m_\pi^t, \Delta m_\pi^c) \equiv (58.65, 37.26, 29.36)$ MeV for the critical quantities computed in the RQM-S model when the m_σ goes from the $600 \rightarrow 750$ MeV.

The $m_\pi - m_K$ plane of the Columbia plot for the $\mu = 0$ has been computed and presented in the Fig. 5(b) for the case of $m_\sigma = 800$ MeV when the strength for producing the first order chiral transition in the RQM-S model becomes very weak. The critical quantities $(m_K^{\text{TCP}}, m_\pi^t, m_\pi^c) \equiv (148.2, 103.19, 82.07)$ MeV obtained in the RQM-S model when the $m_\sigma = 800$ MeV, indicate that the area of the first order region is smallest while the crossover transition region has the largest area in the $m_\pi - m_K$ when the results are compared with the corresponding RQM-S model results for the case of $m_\sigma = 400, 500, 600$ and 750 MeV. When the m_σ goes from the $750 \rightarrow 800$ MeV, the computed critical quantities get reduced by the amount $(\Delta m_K^{\text{TCP}}, \Delta m_\pi^t, \Delta m_\pi^c) \equiv (11.65, 7.21, 5.83)$ MeV. Here it is relevant to mention that the Schaefer et. al. are finding the critical pion mass for the $SU(3)$ chiral limit as $m_\pi^c \equiv 150$ MeV in the Ref. [82] for the case of $m_\sigma = 800$ MeV where the quark one-loop vacuum fluctuations are neglected under the s-MFA. Further as mentioned in the Ref. [62], the chiral matrix model study using the mean field analysis gives $m_\pi^c \equiv 110$ MeV.

The complete comparative perspective of change in the area of first order and second order chiral transition regions of the RQM-S and RQM-I model when the scalar σ mass changes from $m_\sigma = 400 \rightarrow 750$ MeV, have been presented in the Fig. 6(a) after re-plotting the tricritical lines of the vertical $\mu - m_K$ planes at $m_\pi = 0$ of the RQM-S {RQM-I} model Columbia plots in the Fig. 2(a) {2(b)}, 3(a) {3(b)}, 4(a) {4(b)} and 5(a) respectively for the $m_\sigma = 400, 500, 600$ and 750 MeV. One can clearly see that as the m_σ increases, the tricritical lines shift to higher chemical potentials in general for both the models. The RQM-S and RQM-I model tricritical lines are nearly overlapping when the $m_\sigma = 400$ and 500 MeV and one can see that both lines become almost flat for $m_K > 450$ MeV showing saturation for the $m_\sigma = 400$ MeV. Picking up small divergence from below when the $m_K > 450$, the RQM-I tricritical line for the $m_\sigma = 500$ MeV crosses the properly saturating RQM-S tricritical line near the $m_K \sim 500$ MeV. Being quite distinct and separate, the RQM-I model tri-

critical line, that starts from a smaller $m_K^{\text{TCP}} = 207.05$ MeV for the $m_\sigma = 600$ MeV, becomes quite divergent after $m_K > 400$ MeV while the flattening RQM-S model tricritical line shows the proper saturation trend. The RQM-S model tricritical line for the case of $m_\sigma = 750$ MeV that starts from a significantly smaller $m_K^{\text{TCP}} = 159.85$ MeV, shows a very strong divergence and a smaller bending because one needs to take very high chemical potential $\mu = 386.8$ MeV such that the second order transition turns first order even when the kaon mass $m_K = 280$ MeV is significantly smaller, the value upto which the tricritical line can be calculated. In order to appreciate the proper context of the above discussed tricritical lines, one has to recall that the $_{\text{CEP}}$ does not exist in the RQM-S model phase diagram when the $m_\sigma = 750$ MeV, since the chiral transition is crossover all over in the $\mu - T$ plane whereas one finds $_{\text{CEP}}$ in both the scenarios of RQM-S and I model when the $m_\sigma = 400, 500$ and 600 MeV.

The chiral critical solid black lines of the $Z(2)$ critical end points in the horizontal $m_\pi - m_K$ planes (at $\mu = 0$) of the RQM-S {RQM-I} model Columbia plots in the Fig. 2(a) {2(b)}, 3(a) {3(b)}, 4(a) {4(b)}, 5(a) and 5(b) respectively for the $m_\sigma = 400, 500, 600, 750$ and 800 MeV, have been redrawn in one frame of the Fig. 6(b) in order to show the relative shrinking in the area of first order chiral transition regions in response to the expanding chiral crossover transition regions in the RQM-S and RQM-I model when the scalar σ mass changes from $m_\sigma = 400 \rightarrow 800$ MeV. The $SU(3)$ symmetric chiral limit lines for $m_\pi = m_K$ and strange chiral limit $h_y = 0$ line are also plotted. The line types of the RQM-S(I) model chiral critical lines for different m_σ , chiral crossover transition and first order transition regions are marked and explained in the Fig. (6(b)) where the numerical values of the critical quantities m_π^t and m_π^c in the RQM-S(I) model for different m_σ are also given.

The $m_\sigma = 400(500)$ MeV case RQM-S model chiral critical line, which lies marginally above the corresponding critical line of the RQM-I model when the $m_\pi < 80$ MeV overlap completely with it in the range $m_\pi = 80 - 169.25(164.65)$ MeV. The numerical values of the critical quantities m_π^c , m_π^t and the extent of the first order and crossover chiral transition regions in the $m_\pi - m_K$ plane, are nearly the same in the RQM-S and the RQM-I model for the respective cases of the $m_\sigma = 400$ and 500 MeV. While lying noticeably above the critical line of the RQM-I model in the range $m_\pi = 0 \rightarrow 80$ MeV, the RQM-S model chiral critical line for the case of $m_\sigma = 600$ MeV, overlaps with it completely in the range $m_\pi = 80 - 147.66$ MeV. The first order region of the chiral transition in the $m_\pi - m_K$ plane gets reduced by a proportion through which the corresponding chiral crossover transition region increases when the σ mass increases from $400 \rightarrow 600$ MeV in both the RQM-S and I model. The RQM-S chiral critical lines are enclosing comparatively larger first order transition regions for all the m_σ . The RQM-S model first order regions go through

TABLE II. The quantities m_K^{TCP} , m_s^{TCP} , m_π^t , m_{ud}^t , m_π^c , m_{ud}^c and the β_{CEP} : $m_{\pi,\text{CEP}}^*$, $m_{K,\text{CEP}}^*$ are presented in this table for the RQM-S model whose parameters away from the physical point, are fixed using the large N_c standard U(3) ChPT inputs and the RQM-I model whose parameters are fixed using the infrared regularized U(3) ChPT inputs. Very recent results of these quantities computed in the curvature mass based parametrization of the quark meson model with quark one-loop vacuum term (QMVT-I) where the infrared regularized U(3) ChPT inputs are used for parameter fixing [129], are also presented. The results for some of these quantities obtained in the e-MFA:QM model FRG study for $m_\sigma = 530$ MeV and the QM model s-MFA study for $m_\sigma = 800$ MeV, are also shown for comparison. In the QM model s-MFA study, the TCP and second order chiral transition are absent in the light chiral limit $m_\pi = 0$. The change of the quantities Δm_K^{TCP} , Δm_s^{TCP} , Δm_π^t , Δm_{ud}^t , Δm_π^c , Δm_{ud}^c and the $\Delta\beta_{\text{CEP}}$: $\Delta m_{\pi,\text{CEP}}^*$, $\Delta m_{K,\text{CEP}}^*$ are also presented when the m_σ sequentially changes from 400→500 and 500→600 (600→750 and 750→800) in the RQM-S and RQM-I model (RQM-S model). The SU(3) chiral limit results of the critical pion (light quark) mass m_π^c (m_{ud}^c) obtained from different LQCD studies for three degenerate flavors at $\mu = 0$, are presented in the last two rows where the corresponding fermion implementation and the number of time slices N_t are also shown.

m_σ	Model	m_K^{TCP}	m_s^{TCP}	m_π^t	m_{ud}^t	m_π^c	m_{ud}^c	β_{CEP}	$m_{\pi,\text{CEP}}^*$	$m_{K,\text{CEP}}^*$
400	RQM-S	248.8	25.23	169.25	5.97	134.51	3.80	0.38738	53.46	192.14
	RQM-I[129]	242.6	25.53	168.39	6.13	134.16	3.84	0.37963	52.39	188.30
	QMVT-I[129]	137.2	8.06	98.15	2.05	78.45	1.31	0.2215	30.57	109.88
500	RQM-S	244.1	24.33	164.65	5.66	130.71	3.59	0.37665	51.98	186.82
	RQM-I	240.1	25.00	164.02	5.79	130.84	3.66	0.37159	51.33	184.49
600	RQM-S	218.5	19.65	147.66	4.57	117.26	2.90	0.33634	46.41	166.82
	RQM-I	207.05	17.70	146.35	4.59	118.01	2.97	0.32445	44.77	160.93
750	RQM-S	159.85	10.65	110.40	2.57	87.90	1.64	0.25013	34.52	124.06
800	RQM-S	148.2	9.21	103.19	2.25	82.07	1.43	0.23316	32.18	115.65
530	RQM-S[128]	239.58	23.47	161.35	5.44	128.04	3.45	0.36778	50.9	182.96
	RQM-I[128]	235.7	24.08	160.75	5.58	128.38	3.51	0.3642	50.26	180.64
	e-MFA:QM-FRG[35]	169	-	110	3.0	86	-	0.20	27.6	99.2
	QMVT-I[129]	124.7	6.64	90.03	1.72	72.12	1.1	0.2028	27.98	100.58
800	s-MFA:QM[82]	No TCP	-	177	-	150	-	0.488	67.34	242.05
Change of m_σ	Model	Δm_K^{TCP}	Δm_s^{TCP}	Δm_π^t	Δm_{ud}^t	Δm_π^c	Δm_{ud}^c	$\Delta\beta_{\text{CEP}}$	$\Delta m_{\pi,\text{CEP}}^*$	$\Delta m_{K,\text{CEP}}^*$
400→500	RQM-S	4.7	0.9	4.6	0.31	3.8	0.21	0.01073	1.48	5.32
	RQM-I	2.5	0.53	4.37	0.34	3.32	0.18	0.00804	1.06	3.81
500→600	RQM-S	25.6	4.68	16.99	1.09	13.45	0.69	0.04031	5.57	20.0
	RQM-I	33.05	7.3	17.67	1.2	12.83	0.69	0.04714	6.56	23.56
600→750	RQM-S	58.65	9.0	37.26	2.0	29.36	1.26	0.08621	11.89	42.76
750→800	RQM-S	11.65	1.44	7.21	0.32	5.83	0.21	0.01697	2.34	8.41
LQCD Study	$N_t = 4$, Standard Staggered m_π^c	$N_t = 4$, p4 Staggered m_π^c	$N_t = 6$, Standard Staggered m_π^c	$N_t = 6$, Stout Staggered m_π^c	Wilson Clover $N_t = 6$, m_π^c	$N_t = 6$, HISQ Staggered m_π^c	Wilson Clover $N_t = 8$, m_π^c	m_{ud}^c : Möbius Domain Wall		
Ref.	~290 [29]	~67 [30]	~150 [31]	~0 [39]	~300 [32]	≤50 [37]	≤170 [33]	≤4 [41]		

significant reduction in the $m_\pi - m_K$ plane for the significantly large $m_\sigma = 750$ and 800 MeV, hence one finds that the critical quantities m_π^c , m_π^t are also getting reduced accordingly.

First order chiral phase transitions occur over a significantly large and wide area in the vertical and horizontal planes of the RQM-S and I model Columbia plots when the $m_\sigma = 400$ and 500 MeV. Even after the noticeable reduction for the case of larger $m_\sigma = 600$ MeV, the extents of first order chiral transition regions in the RQM-S and RQM-I model Columbia plots, are significantly larger than the first order regions obtained in the e-MFA:FRG QM model Columbia plots for the $m_\sigma = 530$ MeV in Ref. [35] and QMVT model Columbia plots for the $m_\sigma = 400$ and 530 MeV in the Ref. [129]. The critical quantities m_π^t and m_π^c in the horizontal $m_\pi - m_K$

planes of the RQM-S model for the $m_\sigma = 750$ and 800 MeV, when the strength of producing the first order chiral transition is very weak, are respectively comparable to and larger than the values of the m_π^t and m_π^c obtained respectively in the $m_\pi - m_K$ planes of the e-MFA:FRG QM model Columbia plot for the $m_\sigma = 530$ MeV and the QMVT model Columbia plots for the case of $m_\sigma = 400$ and 530 MeV. The e-MFA:FRG QM model work [35] and the QMVT model studies [145, 147, 148] treat the quark one-loop vacuum correction term using the $\overline{\text{MS}}$ renormalization scheme and curvature masses of mesons are used to fix the model parameters. The above method of treating quark one-loop vacuum fluctuations, generates a very large smoothing effect on the strength of the chiral transition, hence one finds significantly smaller first order regions in the Columbia plots

of these studies [128, 129].

Different effective theory approaches are actively pursuing the Columbia plot studies in the light of the most recent LQCD results. The very recent work of the Ref.[63] has discussed a scenario in the Columbia plot of its Fig.1, where the area of first order region is maximum when the sixth order anomalous coupling is zero and the first order region decreases corresponding to the increasing sixth order coupling strength while the cubic coupling strength decreases. They have shown a possibility where the chiral phase transition in the whole $m_\pi - m_K$ plane of the Columbia plot becomes second order, even though the $U_A(1)$ anomaly is still broken because of the large strength of the sixth order anomalous coupling term while the cubic coupling strength is zero. The FRG QM model study under the LPA in the Ref. [35], has shown that, the critical pion mass $m_\pi^c \equiv 86$ MeV obtained in the e-MFA of the QM model, becomes quite small $m_\pi^c \equiv 17$ MeV indicating much reduced first order regions in the Columbia plot when the thermal and vacuum quantum fluctuations of meson loops are also included in their study with the full FRG flow. However the Ref. [62] has pointed out that the approximation used in the above work is known to overestimate the mesonic fluctuations [116] that tend to soften the chiral transition. Further one should also note that it has been cautioned in the Ref. [45] that the LPA in the FRG studies, completely neglects the wave function renormalization which might affect the final result. Including the nonperturbative mesonic loop corrections in the Hartree approximation of LSM using the Cornwall-Jackiw-Tomboulis (CJT) two-particle (2PI) irreducible effective action formalism, the beyond perturbation method studies [65, 66] reported a large first order region in the Columbia plot when the $U_A(1)$ anomaly is absent and the results show drastic σ mass dependence in the presence of the $U_A(1)$ anomaly where the heavier m_σ values give the first order regions which disappear for the realistic m_σ . Using the symmetry improved CJT called the SICJT formalism [118] in the LSM, the very recent study in the Ref. [119], finds a stable first-order regime with a definite location of the T_{CP} at $m_s^{TCP}/m_s^{Phys} = 0.696$ which shows small variation on increasing the $m_\sigma/f_0(500)$ from 672.4 MeV to 797.2 MeV whereas the critical pion mass reported in their work is $m_\pi^c = 52.4$ MeV for the $m_\sigma/f_0(500) = 672.4$ MeV. They have clarified that the enhanced first order regions found with the conventional CJT formalism, are merely an artifact due to the lack of manifest invariance of the Nambu Goldstone and low energy theorems at finite temperature. The relative position of the RQM-S model T_{CP} at m_K^{TCP}/m_K^{Phys} (m_s^{TCP}/m_s^{Phys}), with respect to the value of kaon (s quark) mass at the physical point, shifts from the 0.5016 to 0.4405 (0.2927 to 0.2280) when the $m_\sigma = 400 \rightarrow 600$ MeV and one finds a significantly large shift in the m_K^{TCP}/m_K^{Phys} (m_s^{TCP}/m_s^{Phys}) from the 0.4405 to 0.2988 (0.2280 to 0.1068) when the $m_\sigma = 600 \rightarrow 800$ MeV. In a similar fashion the $m_\pi^c(m_{ud}^c)$ changes from 134.51 (3.8) to 117.26 (2.9) MeV when the

$m_\sigma = 400 \rightarrow 600$ whereas the change in the $m_\pi^c(m_{ud}^c)$ from 117.26 (2.9) to 82.07 (1.43) MeV is significantly large when the $m_\sigma = 600 \rightarrow 800$ MeV. It is important to note that we are finding stable first order regions in the RQM model Columbia plots even though its area gets reduced for very high $m_\sigma = 800$ MeV. Furthermore the relatively larger first order regions in the RQM-S model Columbia plots are caused by the fact that the $U_A(1)$ anomaly strength c which contains a condensate dependent part, gets significantly enhanced when the meson self energies due to quark loops are evaluated using the meson pole masses and parameters are fixed on-sell where the smoothing effect of the quark one-loop vacuum fluctuations become moderate.

C. Comparing the RQM-S and I model Columbia plots in the quark mass $m_{ud} - m_s$ and $\mu - m_s$ planes

The Columbia plots in the $m_\pi - m_K$ plane at $\mu = 0$ and the $\mu - m_K$ plane at $m_\pi = 0$ can be redrawn in the light-strange quark mass $m_{ud} - m_s$ plane at $\mu = 0$ and the chemical potential-strange quark mass $\mu - m_s$ plane at $m_{ud} = 0$ by using the Eqs. (21) and (22) for the infrared regularized U(3) ChPT input set for the RQM-I model and the Eqs.(31) and (32) for the large N_c standard U(3) ChPT input set for the RQM-S model. Columbia plots in the quark mass planes would make the results of chiral limit studies in effective model approach, available for comparison with LQCD results and studies in other approaches. In order to map the results from the $m_\pi - m_K$ to the $m_{ud} - m_s$ plane, the light quark mass has been fixed to $m_{ud} = 4$ MeV at the physical point. With the $m_{ud} = 4$ MeV, the solutions of Eqs. (21) and (22) give the physical point value of the strange quark mass as ($m_s^{Phys} = 99.7$ MeV) for the RQM-I model whereas the solutions of Eqs. (31) and (32) give the physical point value of the strange quark mass for the RQM-S model as ($m_s^{Phys} = 86.2$ MeV). The zero light quark mass $m_{ud} = 0$ gives the light chiral limit. The strange quark mass physical point value for the physical kaon mass $m_K = 496$ MeV, gives the second order chiral phase transition on the m_s axis when $m_{ud} = 0$. The second order phase transition turns first order chiral transition at the tricritical point of strange quark mass m_s^{TCP} corresponding to the kaon mass m_K^{TCP} when the $m_s(m_K)$ is reduced keeping the $m_{ud} = 0$ and $\mu = 0$. For different non-zero values of μ on the chemical potential axis, the tricritical point value of the strange quark mass shifts up on the m_s axis and the resulting tricritical line in the $\mu - m_s$ plane at $m_{ud} = 0$, depicted by blue line in the figures below, starts from the m_s^{TCP} at the $\mu = 0$ (shown by solid blue dot in the figures) and demarcates the first order transition region above it from the second order transition region lying below. The chiral critical line separating the chiral crossover transition region from the first order region in the $m_{ud} - m_s$ plane at $\mu = 0$, is obtained from the corresponding line in the $m_\pi - m_K$ plane and it has been

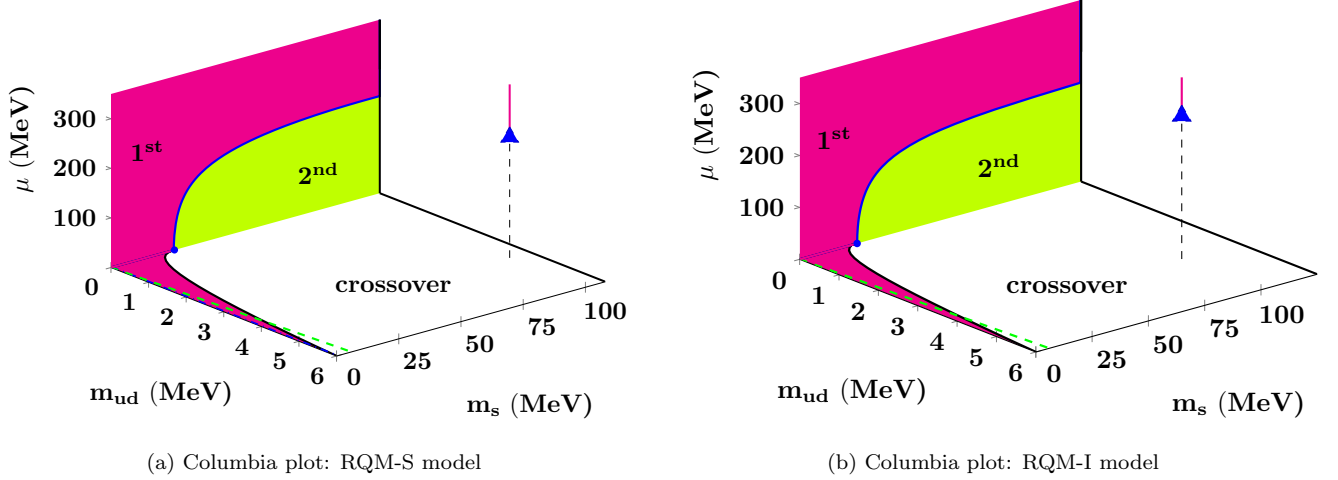


FIG. 7. The chiral transitions for the $m_{ud} = 0$ and $\mu = 0$ are depicted respectively in the $\mu - m_s$ and $m_{ud} - m_s$ plane. The results for the RQM-S model when its parameters are fixed using the large N_c standard U(3) ChPT inputs, are presented in the left panel (a) whereas the right panel (b) shows the results for the RQM-I model where its parameters are fixed using the infrared regularized U(3) ChPT inputs. The second order $Z(2)$ critical line in solid black color that separates the crossover from the first order transition region in the Fig.(a) and (b), intersects the $m_{ud} = m_s$ green dash line respectively at the critical light quark mass $m_{ud}^c = 3.80$ and $m_{ud}^c = 3.84$ MeV and it terminates respectively at the terminal light quark mass $m_{ud}^t = 5.97$ and $m_{ud}^t = 6.13$ MeV. Solid blue line of the tricritical points which starts respectively at the blue dot $m_s^{TCP} = 25.23$ and $m_s^{TCP} = 25.53$ MeV in the Fig.(a) and (b), separates the second and first order regions. The black dashed vertical line at the physical point in the Fig.(a) and (b), shows the crossover transition which ends at the critical end point in blue triangle and the solid red line shows the first order transition. The scalar σ mass $m_\sigma = 400$ MeV.

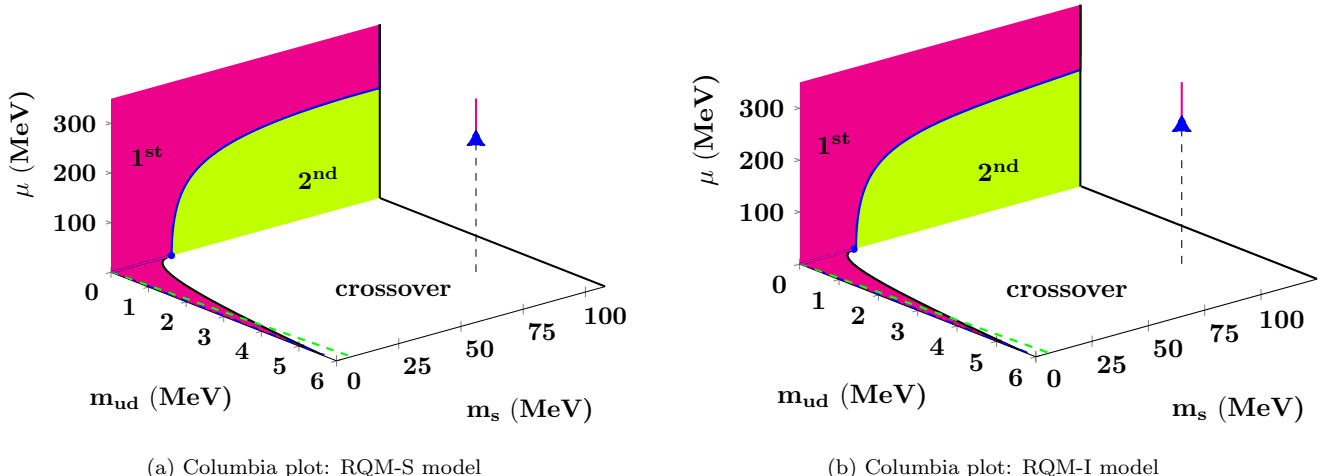


FIG. 8. The chiral transitions in the $\mu - m_s$ plane for the $m_{ud} = 0$ and the $m_{ud} - m_s$ plane for the $\mu = 0$ when the $m_\sigma = 500$ MeV are presented in the left panel (a) for the RQM-S model and the right panel (b) for the RQM-I model. The points, lines, crossover, first and second order chiral transition regions and features are defined similar to the Fig.(7). The critical quantities (m_s^{TCP} , m_{ud}^t , m_{ud}^c) in the RQM-S and RQM-I model are (24.33, 5.66, 3.59) MeV and (25.0, 5.79, 3.66) MeV in respective order.

depicted here also by the solid black color. The chiral critical line terminates on the m_{ud} axis at the terminal light quark mass m_{ud}^t (obtained from the m_π^t) beyond which the transition is a smooth crossover everywhere in the $m_{ud} - m_s$ plane. The intersection point of the SU(3) symmetric $m_{ud} = m_s$ chiral limit path, depicted by the

green dash line in the figures, with the chiral critical line in the solid black color, gives the critical light quark mass m_{ud}^c (obtained from the m_π^c) where the boundary of first order region ends in the $m_{ud} - m_s$ plane.

The horizontal $m_{ud} - m_s$ and vertical $\mu - m_s$ quark mass planes of the RQM-S model Columbia plot for the

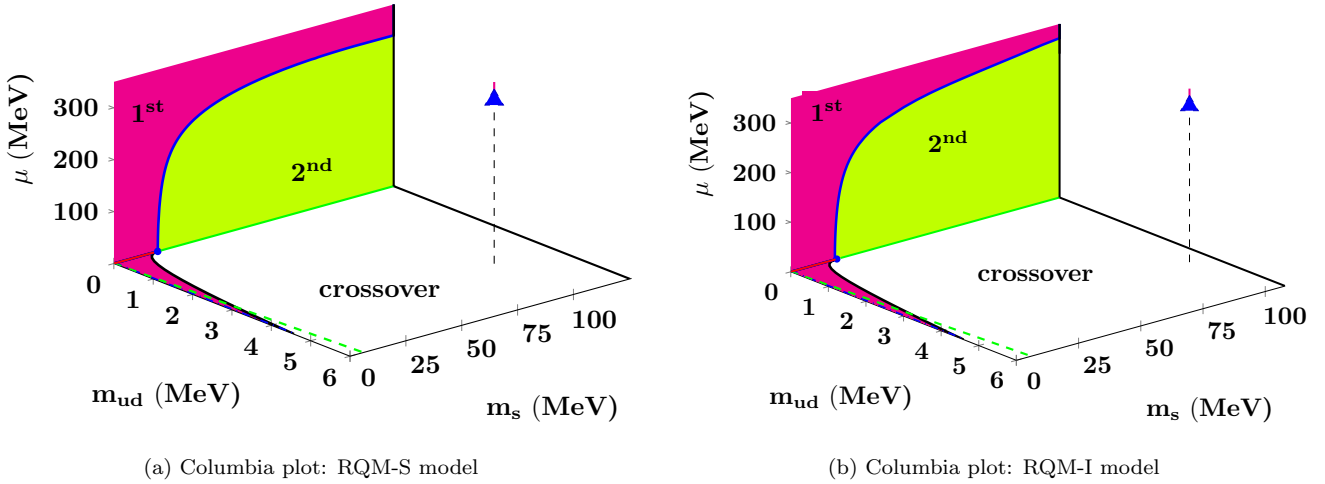


FIG. 9. Chiral transitions in the $\mu - m_s$ plane at $m_{ud} = 0$ and the $m_{ud} - m_s$ plane at $\mu = 0$ for the $m_\sigma = 600$ MeV, are presented in the left panel (a) for the RQM-S model and the right panel (b) for the RQM-I model. The points, lines, crossover, first and second order chiral transition regions and features are defined similar to the Fig.(7). The critical quantities $(m_s^{\text{TCP}}, m_{ud}^t, m_{ud}^c)$ are respectively $(19.65, 4.57, 2.90)$ MeV and $(17.70, 4.59, 2.97)$ MeV in the RQM-S and RQM-I model.

$m_\sigma = 400$ MeV show the largest extent of the first order chiral transition regions in the Fig. 7(a) where the obtained critical quantities are $(m_s^{\text{TCP}}, m_{ud}^t, m_{ud}^c) = (25.23, 5.97, 3.80)$ MeV corresponding to the $(m_K^{\text{TCP}}, m_\pi^t, m_\pi^c) \equiv (248.8, 169.25, 134.51)$ MeV. Even though the RQM-I model first order regions in the $m_\pi - m_K$ and $\mu - m_K$ planes of the Fig. 2(b) are marginally smaller than the corresponding RQM-S model first order regions in the Fig. 2(a), the first order regions in the $m_{ud} - m_s$ and $\mu - m_s$ quark mass planes of the RQM-I model Columbia plot for the $m_\sigma = 400$ MeV in the Fig. 7(b) are equivalent and negligibly larger than the corresponding first order regions in the Fig. 7(a) for the RQM-S model because the strange quark mass value ($m_s^{\text{Phys}} = 99.7$ MeV) for the RQM-I model at the physical point, is larger than its RQM-S model value ($m_s^{\text{Phys}} = 86.2$ MeV). Hence the RQM-I model critical quantities in the Fig. 7(b) are obtained as $(m_s^{\text{TCP}}, m_{ud}^t, m_{ud}^c) = (25.53, 6.13, 3.84)$ MeV corresponding to the $(m_K^{\text{TCP}}, m_\pi^t, m_\pi^c) \equiv (242.6, 168.39, 134.16)$ MeV. The extents of first order regions in the quark mass planes of the RQM-S and RQM-I Columbia plots for the $m_\sigma = 500$ MeV respectively in the Fig. 8(a) and Fig. 8(b), get reduced only marginally when compared to the case of $m_\sigma = 400$ MeV. After slight reduction by $(\Delta m_s^{\text{TCP}}, \Delta m_{ud}^t, \Delta m_{ud}^c) = (0.9, 0.31, 0.21)$ MeV when the $m_\sigma = 400 \rightarrow 500$ MeV, the RQM-S model critical quantities in the Fig. 8(a) are obtained as $(m_s^{\text{TCP}}, m_{ud}^t, m_{ud}^c) = (24.33, 5.66, 3.59)$ MeV corresponding to the $(m_K^{\text{TCP}}, m_\pi^t, m_\pi^c) \equiv (244.1, 164.65, 130.71)$ MeV whereas with the corresponding marginal reduction of $(\Delta m_s^{\text{TCP}}, \Delta m_{ud}^t, \Delta m_{ud}^c) = (0.53, 0.34, 0.18)$ MeV, the RQM-I model critical quantities in the

Fig. 8(b) are obtained as $(m_s^{\text{TCP}}, m_{ud}^t, m_{ud}^c) = (25.0, 5.79, 3.66)$ MeV corresponding to the $(m_K^{\text{TCP}}, m_\pi^t, m_\pi^c) \equiv (240.1, 164.02, 130.84)$ MeV when the $m_\sigma = 500$ MeV.

In contrast to the results obtained when the $m_\sigma = 400 \rightarrow 500$ MeV, the first order regions shrink noticeably when the $m_\sigma = 500 \rightarrow 600$ MeV as evident from the regions of the first order transition witnessed in the quark mass planes of the RQM-S and RQM-I Columbia plots for the $m_\sigma = 600$ MeV respectively in the Fig. 9(a) and Fig. 9(b). After moderately large reduction of $(\Delta m_s^{\text{TCP}}, \Delta m_{ud}^t, \Delta m_{ud}^c) = (4.68, 1.09, 0.69)$ MeV when the $m_\sigma = 500 \rightarrow 600$ MeV, the RQM-S model critical quantities in the Fig. 9(a) are obtained as $(m_s^{\text{TCP}}, m_{ud}^t, m_{ud}^c) = (19.65, 4.57, 2.90)$ MeV corresponding to the $(m_K^{\text{TCP}}, m_\pi^t, m_\pi^c) \equiv (218.5, 147.66, 117.26)$ MeV. On account of the significantly large reduction of $(\Delta m_s^{\text{TCP}}, \Delta m_{ud}^t, \Delta m_{ud}^c) = (7.3, 1.2, 0.69)$ MeV in the RQM-I model critical quantities when the $m_\sigma = 500 \rightarrow 600$ MeV, one finds noticeably smaller areas of first order regions in the Fig. 9(b) when compared to the first order regions of the RQM-S model in the Fig. 9(a) even though the physical point value of the strange quark mass ($m_s^{\text{Phys}} = 99.7$ MeV) is larger for the RQM-I model. With the above mentioned reduction, the RQM-I model critical quantities in the Fig. 9(b) are obtained as $(m_s^{\text{TCP}}, m_{ud}^t, m_{ud}^c) = (17.70, 4.59, 2.97)$ MeV corresponding to the $(m_K^{\text{TCP}}, m_\pi^t, m_\pi^c) \equiv (207.05, 146.35, 118.01)$ MeV when the $m_\sigma = 600$ MeV.

All the tricritical lines in the vertical $\mu - m_s$ planes at $m_{ud} = 0$, in the Fig. 7(a), 8(a) and 9(a) of the RQM-S model and Fig. 7(b), 8(b) and 9(b) of the RQM-S model respectively for the $m_\sigma = 400, 500$ and 600 MeV, begin with a large positive slope from their ori-

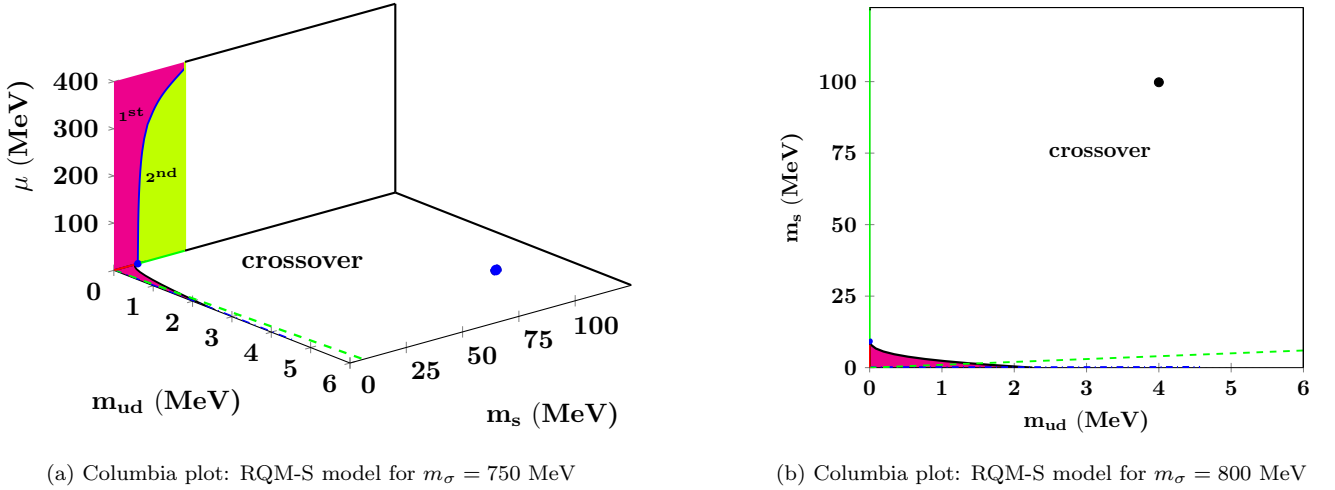


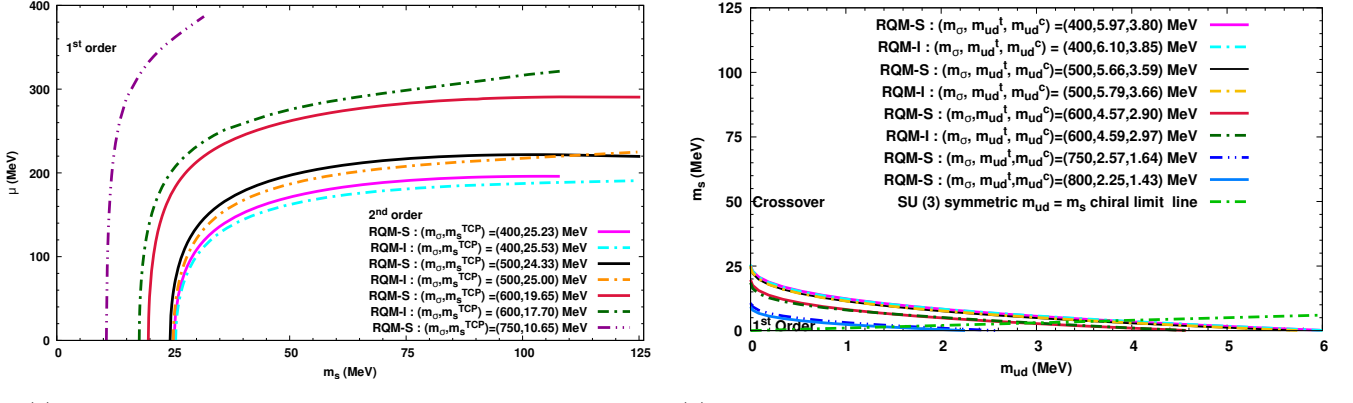
FIG. 10. The left panel (a) depicts the RQM-S model chiral transition in the horizontal plane $m_{ud} - m_s$ at $\mu = 0$ and the vertical $\mu - m_s$ plane at $m_{ud} = 0$ when the $m_\sigma = 750$ MeV. The horizontal plane $m_{ud} - m_s$ at $\mu = 0$ in the right panel (b) presents the chiral transition in RQM-S model for the case of $m_\sigma = 800$ MeV. The points, lines, crossover, first and second order chiral transition regions and features are defined similar to the Fig.(7). The tricritical line demarcating the first and second order colored regions, is computed only upto the point $(m_s, \mu) = (31.61, 386.8)$ MeV in the Fig. (a) because the chemical potential becomes very high for a significantly smaller strange mass in the $\mu - m_s$ plane. The RQM-S model critical quantities $(m_s^{\text{TCP}}, m_{ud}^t, m_{ud}^c)$ are respectively $(10.65, 2.57, 1.64)$ MeV and $(9.21, 2.25, 1.43)$ MeV when $m_\sigma = 750$ and 800 MeV.

gin at the m_s^{TCP} and $\mu = 0$ and suffer a large bending for higher chemical potentials. The RQM-S model tricritical lines show proper saturation for all the cases of the the $m_\sigma = 400, 500$ and 600 MeV as each of them become flat and horizontal with almost a zero slope in the strange quark mass range $m_s = 91.5 - 108$ MeV that corresponds to the kaon mass range of $m_K = 500 - 550$ MeV. When the $m_\sigma = 400$ MeV in the RQM-I model, its tricritical line shows a saturation pattern close to that of the RQM-S model as its slope approaches nearly zero in the strange quark mass range $m_s = 105.22 - 124.66$ MeV for the $m_K = 500 - 550$ MeV. But the RQM-I model tricritical line for the $m_\sigma = 500$ MeV, picks up a divergence trend after $m_s > 69.1$ MeV for the $m_K > 400$ MeV. Showing a significantly large divergence after the $m_s > 69.1$ MeV, the RQM-I model tricritical in the Fig. 9(b) for the $m_\sigma = 600$ MeV, looks very different from the corresponding RQM-S model tricritical line in the Fig. 9(a).

The critical quantities suffer a very large reduction of $(\Delta m_s^{\text{TCP}}, \Delta m_{ud}^t, \Delta m_{ud}^c) = (9.0, 2.0, 1.26)$ MeV when the $m_\sigma = 600 \rightarrow 750$ MeV in the RQM-S model. One finds very small areas of first order chiral transition regions in the vertical $\mu - m_s$ and horizontal $m_{ud} - m_s$ planes of the RQM-S model Columbia plot in the Fig. 10(a) when the $m_\sigma = 750$ MeV as also signified by the observed critical quantities $(m_s^{\text{TCP}}, m_{ud}^t, m_{ud}^c) = (10.65, 2.57, 1.64)$ MeV. The tricritical line in the vertical $\mu - m_s$ plane is very strongly divergent since it suffers quite a small bending and it could be drawn only upto $m_s = 31.6$ MeV for $m_K = 280$ MeV because even for such a smaller m_s value, one needs to increase the chemical poten-

tial to very high $\mu = 386.83$ MeV for finding the TCP since strength of the chiral transition becomes very weak for the $m_\sigma = 750$ MeV. The divergent tricritical line is associated with a chiral critical region whose spread is significantly smaller in the Columbia plot, hence the CEP does not exist at the physical point co-ordinates in the $m_{ud} - m_s$ plane. The critical quantities change by $(\Delta m_s^{\text{TCP}}, \Delta m_{ud}^t, \Delta m_{ud}^c) = (1.44, 0.32, 0.21)$ MeV when the $m_\sigma = 750 \rightarrow 800$ MeV in the RQM-S model. The Fig. 10(b) shows the horizontal $m_{ud} - m_s$ plane of the Columbia plot where the chiral critical line of $Z(2)$ points underneath the largest chiral crossover area, covers the smallest area of first order regions which gets indicated also by the values of the critical quantities $(m_s^{\text{TCP}}, m_{ud}^t, m_{ud}^c) = (9.21, 2.25, 1.43)$ MeV when the $m_\sigma = 800$ MeV in the RQM-S model.

The tricritical lines in the chemical potential-strange quark mass vertical $\mu - m_s$ planes at $m_{ud} = 0$ of the RQM-S {RQM-I} model Columbia plots in the Fig. 7(a) {(7(b)}}, (8(a)) {(8(b)}}, (9(a)) {(9(b)} and (10(a)) respectively for the $m_\sigma = 400, 500, 600$ and 750 MeV have been redrawn in a single frame of the Fig. (11(a)) in order to show how the comparative shifting of the tricritical lines to higher chemical potentials, indicate the decreasing first order regions while the corresponding area of second order transitions increase in the $\mu - m_s$ plane when the m_σ increases from $400 \rightarrow 750$ MeV. Turning flat with a zero slope in the range $m_s = 91.5$ to 108 MeV of strange quark mass, the tricritical lines for the RQM-S model, show proper saturation for all the cases of the $m_\sigma = 400, 500$ and 600



(a) Vertical plane $\mu - m_s$ for $m_\sigma=400,500,600$ and 750 MeV. (b) Horizontal plane $m_{ud} - m_s$ for $m_\sigma=400,500,600,750, 800$ MeV.

FIG. 11. Left panel (a) (Right panel (b)) presents the comparison of lines and regions in the vertical $\mu - m_s$, $m_{ud} = 0$ (horizontal $m_{ud} - m_s$, $\mu = 0$) planes of the three dimensional RQM-S and RQM-I model Columbia plots for the $m_\sigma = 400, 500, 600, 750$ and 800 MeV in the Fig. (7(a)), (7(b)), (8(a)), (8(b)), (9(a)), (9(b)) and (10(a)), (10(b)). RQM-S and RQM-I model tricritical lines for the $m_\sigma = 400, 500, 600$ and 750 MeV, as marked and explained in the Fig.(a), start from the m_s^{TCP} on the m_s axis and demarcate the first order region above them from the second order region below them on their right hand side. RQM-S and RQM-I model Z(2) critical lines for the $m_\sigma = 400, 500, 600, 750$ and 800 MeV, as marked and explained in the Fig.(b), separating the crossover transition region above them from the first order region that lies below, intersect the SU(3) symmetric $m_{ud} = m_s$ chiral limit line at the critical light quark mass m_{ud}^c and terminate on the m_{ud} axis at the terminal light quark mass of m_{ud}^t .

MeV. While showing a saturation pattern in the range $m_s = 105.22$ to 124.66 MeV for the $m_\sigma = 400$ and picking up a small divergence for the $m_\sigma = 500$ MeV, the RQM-I model tricritical line for the case of $m_\sigma = 600$ MeV, becomes significantly divergent after the $m_s > 69.1$ MeV and looks completely different from the RQM-S model tricritical line. Owing to its very strong divergence for the large $m_\sigma = 750$ MeV, the RQM-S model tricritical line could be drawn only upto $(m_s, \mu) = (31.6, 386.83)$ MeV since the strength of the chiral transition becomes very weak.

The horizontal $m_{ud} - m_s$ planes (at $\mu = 0$) of the RQM-S {RQM-I} model Columbia plots together with the chiral critical solid black lines and the SU(3) symmetric chiral limit lines for the $m_{ud} = m_s$ in the Fig. (7(a)) {(7(b))}, (8(a)) {(8(b))}, (9(a)) {(9(b))}, (10(a)) and (10(b)) respectively for the $m_\sigma = 400, 500, 600, 750$ and 800 MeV, have been plotted again at one place in the Fig. (11(b)) for depicting the relative shrinkage in the first order chiral transition regions when the areas of chiral crossover transition in the RQM-S and RQM-I model, expand corresponding to the increase of scalar σ meson mass in the range $m_\sigma = 400$ to 800 MeV. The different line types and regions are marked and explained in the Fig. (11(b)) where the values of critical quantities m_{ud}^t and m_{ud}^c are also given. The RQM-S and RQM-I model $Z(2)$ chiral critical lines for the $m_\sigma = 400$ and 500 MeV are nearly overlapping. In order to understand the above mentioned results, one has to recall that when the light quark mass is fixed to $m_{ud} = 4$ MeV at the physical point, the solutions of Eqs. (21) and (22) for the RQM-I model give

larger strange quark mass $m_s^{Phys} = 99.7$ MeV while the solutions of the Eqs.(31) and (32) for the RQM-S model give moderate strange quark mass $m_s^{tinyPhys} = 86.2$ MeV at the physical point. If one tries to match the strange quark mass value at the physical point for both the input sets I and S, by taking $m_s^{Phys} = 86.2$ MeV at the physical point for the infrared regularized ChPT input set I, one needs to take a lower value of light quark mass $m_{ud} = 3.46$ MeV at the physical point such that the m_s becomes 86.2 MeV and if that is done, the critical quantities defined in terms of light and strange quark masses will have a smaller value in the RQM-I model [128]. One should also note that the chiral constants and parameters of the large N_c standard U(3) ChPT input set-S, give $q = \frac{m_s}{m_{ud}} = 21.56$ at the physical point and this value lies in its appropriate range given in the Ref. [128, 136, 137]. The first order region under the chiral critical line is very small for the $m_\sigma = 750$ MeV and it is smallest for the $m_\sigma = 800$ MeV. In the RQM-S model, the largest value of the critical light quark mass is obtained as $m_{ud}^c = 3.8$ MeV when the $m_\sigma = 400$ MeV while its smallest value $m_{ud}^c = 1.43$ MeV is found for a very large $m_\sigma = 800$ MeV. It is relevant to recall that the quark one-loop vacuum fluctuation exerts a very strong smoothing effect on the strength of chiral transition in the curvature mass parametrized QMVT model where one finds significantly smaller areas of first order transition even for the $m_\sigma = 400$ and 530 MeV as shown in a very recent work in ref. [129] where one finds the smallest $m_{ud}^c = 1.1$ MeV for the $m_\sigma = 530$ MeV. It is important to see that the range $m_{ud}^c = 3.8$ to 1.43 MeV of critical light quark mass values (for different m_σ)

found in our present RQM-S model work, lies well within the range of $m_{ud}^c \leq 4$ MeV given by recent LQCD study using Möbius domain wall fermions in Ref. [41]. The critical pion mass m_π^c and the critical light quark mass m_{ud}^c obtained from the different LQCD study results, are presented in the Table(II) for a comparative view.

IV. SUMMARY

The problem of the loss of the spontaneous chiral symmetry breaking (SCSB) in the quark meson (QM) model for the $m_\sigma = 400 - 800$ MeV when the chiral limit studies are performed [64, 66, 82, 92, 93, 99] in the often used fixed-ultraviolet (UV) scheme [35], where the light (strange) explicit chiral symmetry breaking strengths $h_x(h_y)$ are reduced and the other model parameter values are kept fixed as at the physical point, got cured very recently in the on-shell renormalized 2+1 flavor quark meson (RQM) model [128, 129] when its parameter fixing away from the physical point for the reduced π and K masses (as the $m_\pi, m_K \rightarrow 0$), was refined by using the (m_π, m_K) dependent scaling relations for the f_π, f_K and M_η^2 given by the $\mathcal{O}(\frac{1}{f^2})$ accurate results of the large N_c standard U(3) chiral perturbation theory (ChPT) [132–137] in the RQM-S model and the infrared regularized U(3) ChPT [69, 138–141] in the RQM-I model. The Columbia plots of the RQM-S model for the $m_\sigma = 400, 500, 600, 750$ and 800 MeV and the RQM-I model for the $m_\sigma = 500$ and 600 MeV are computed in the present work. Bringing out similarities and differences after a thorough and comprehensive comparison of the RQM-S and RQM-I model Columbia plots for the $m_\sigma = 400, 500$ and 600 MeV, it has been shown conclusively in the present work that the large N_c standard U(3) ChPT scaling relations for the (m_π, m_K) dependence of the f_π, f_K and M_η^2 , constitute the improved and better prescription for Chiral limit studies. We emphasize that the RQM-S model has given us the framework in which the chiral limit studies can be consistently performed over the complete range of $m_\sigma = 400 \rightarrow 800$ MeV without any ambiguity or heuristic adjustment in its parameter fixing whereas the e-MFA:FRG QM model chiral limit study, where the FRG flow allows for the scalar σ masses only in the range $m_\sigma \in [400, 600]$ MeV [35], could avoid the loss of SCSB only by heuristically adjusting the initial effective action successively to larger scales ($\Lambda' > \Lambda$ (for starting the FRG flow) at each step of reducing the symmetry breaking strengths such that the f_π does not change in their ChPT motivated fixed f_π scheme.

The fraction $\beta = \frac{m_\pi^*}{m_\pi} = \frac{m_K^*}{m_K}$ provides us a direct path from the physical point to the chiral limit as it defines the reduced (π, K) masses (m_π^*, m_K^*) such that the $\frac{m_\pi^*}{m_K^*} = \text{physical point ratio } \frac{m_\pi}{m_K}$ where the ChPT parameter ratio $q = \frac{2 m_s}{m_u + m_d}$ also gets fixed. Turning sharper as the β is decreased, the chiral crossover transition for the physical point $\beta=1$ becomes sec-

ond order transition at the Z_2 critical point fraction β_{CEP} . The changing β_{CEP} from the $0.38738 \{0.37963\} \rightarrow 0.37665 \{0.37159\} \rightarrow 0.33634 \{0.32445\}$ for the changing m_σ as $400 \rightarrow 500 \rightarrow 600$ MeV gives us the correspondingly changed reduced $_{\text{CEP}}$ masses $(m_{\pi, \text{CEP}}^*, m_{K, \text{CEP}}^*)$ as $(53.46, 192.14) \{(52.39, 188.30)\} \rightarrow (51.98, 186.82) \{(51.33, 184.49)\} \rightarrow (46.41, 166.82) \{(44.77, 160.93)\}$ MeV in respective order for which the chiral crossover transition becomes second order transition in the RQM-S {RQM-I} model. The relative decrease in β_{CEP} indicates that the chiral transition strength becomes only marginally weak when $m_\sigma = 400 \rightarrow 500$ MeV whereas it gets noticeably weaker when $m_\sigma = 500 \rightarrow 600$ MeV. Note that since $\beta_{\text{CEP}}|_{(m_\sigma=400,500,600\text{MeV:RQM-S})} > \beta_{\text{CEP}}|_{(m_\sigma=400,500,600\text{MeV:RQM-I})}$, the use of input set-S gives rise to a stronger strength of transition in the RQM-S model as the first order chiral transition is obtained by a smaller reduction in the masses of π and K mesons. The β_{CEP} changes from the $0.33634 \rightarrow 0.25013 \rightarrow 0.23316$ for the changing m_σ in the RQM-S model as $600 \rightarrow 750 \rightarrow 800$ MeV. Even though the chiral transition gets strongly diluted due to a very high $m_\sigma = 800$ MeV, its strength in the RQM-S model remains stronger than what is found in the e-MFA:FRG QM model [35] and the curvature mass based parametrized QMVT model [129] study for the moderate $m_\sigma = 530$ MeV because the $\beta_{\text{CEP}}|_{(m_\sigma=800\text{ MeV:RQM-S})} = 0.23316 > \beta_{\text{CEP}}|_{(m_\sigma=530\text{MeV:e-MFA:FRG})} = 0.2 \sim \beta_{\text{CEP}}|_{(m_\sigma=530\text{MeV:QMVT})} = 0.2028$.

The second order transition turns first order on the kaon (s quark) mass axis of the Columbia plot for the light chiral limit $m_\pi = 0$ ($m_{ud} = 0$), at the tricritical point at $m_K = m_K^{\text{TCP}}$ ($m_s = m_s^{\text{TCP}}$). The chiral critical line, of the second order $Z(2)$ universality points that demarcates the crossover from the first order region in the $m_\pi - m_K$ ($m_{ud} - m_s$) plane at the $\mu = 0$, terminates on the strange chiral limit line $h_{y0} = 0$ ($m_s = 0$) at the terminal π (light quark) mass $m_\pi^t(m_{ud}^t)$ beyond which the transition is a smooth crossover everywhere and this line intersects the SU(3) symmetric $m_\pi = m_K$ ($m_{ud} = m_s$) chiral limit line also at the critical pion mass m_π^c (light quark mass m_{ud}^c) where the boundary of first order region ends. The values of the critical quantities $(m_K^{\text{TCP}}, m_\pi^t, m_s^c) \{(m_s^{\text{TCP}}, m_{ud}^t, m_{ud}^c)\}$ in the meson mass ($m_\pi - m_K$) {quark mass ($m_{ud} - m_s$)} planes of the RQM-S model and RQM-I model Columbia plots are $(248.8, 169.25, 134.51) \{(25.23, 5.97, 3.80)\}$ MeV and $(242.6, 168.39, 134.16) \{(25.53, 6.13, 3.84)\}$ MeV in the respective order of models for the $m_\sigma = 400$ MeV and $(244.1, 164.65, 130.71) \{(24.33, 5.66, 3.59)\}$ MeV and $(240.1, 164.02, 130.84) \{25.0, 5.79, 3.66\}$ MeV in the respective order of models for the $m_\sigma = 500$ MeV. The largest first order regions are found in the Columbia plot of the RQM-S model when the $m_\sigma = 400$ MeV. The RQM-S and RQM-I model first order regions, get only slightly reduced when the $m_\sigma = 400 \rightarrow 500$ MeV. Even though the $m_\sigma = 400$ and 500 MeV case first order regions in the $m_\pi - m_K$ and $\mu - m_K$ planes of the RQM-

S model are slightly larger than those of the RQM-I model, the first order regions in the $m_{ud} - m_s$ and $\mu - m_s$ quark mass planes of the RQM-I model Columbia plot look equivalent and negligibly larger than those of the RQM-S model because the strange quark mass ($m_s^{\text{phys}} = 99.7$ MeV) for the RQM-I model at the physical point, is larger than its RQM-S model value ($m_s^{\text{phys}} = 86.2$ MeV). When the $m_\sigma = 600$ MeV, the critical quantities $(m_K^{\text{TCP}}, m_\pi^t, m_\pi^c) \{ (m_s^{\text{TCP}}, m_{ud}^t, m_{ud}^c) \}$ computed in the meson {quark} mass planes, are $(218.5, 147.66, 117.26) \{ (19.65, 4.57, 2.90) \}$ MeV in the RQM-S model and $(207.05, 146.35, 118.01) \{ (17.70, 4.59, 2.97) \}$ MeV in the RQM-I model. In contrast to a marginal change in first order regions of both the RQM-S and RQM-I models for the $m_\sigma = 400 \rightarrow 500$ MeV, the shrinking of first order regions in the RQM-I model Columbia plots, in comparison to that of the RQM-S model, is noticeably larger when the $m_\sigma = 500 \rightarrow 600$ MeV. Even if the physical point strange quark mass $m_s^{\text{phys}} = 99.7$ MeV is larger in the RQM-I model, its quark mass planes for the $m_\sigma = 600$ MeV case, show noticeably smaller first order regions.

The tricritical lines in the vertical $\mu - m_K, m_\pi = 0$ ($\mu - m_s, m_{ud} = 0$) planes of the RQM-S and RQM-I model Columbia plots, start with a large positive slope from the m_K^{TCP} (m_s^{TCP}) at $\mu = 0$ and bend strongly for higher μ . Turning flat with almost a zero slope at higher μ in the kaon (s quark) mass range of $m_K = 500 - 550$ ($m_s = 91.5 - 108$) MeV, the RQM-S model tricritical lines for all the cases of the $m_\sigma = 400, 500$ and 600 , show proper saturation. The RQM-I model tricritical line shows a saturation pattern close to that of the RQM-S model only when the $m_\sigma = 400$ MeV. Since the slope does not decrease after the $m_K > 400$ ($m_s > 69.1$) MeV, the RQM-I model tricritical lines for the $m_\sigma = 500$ and 600 MeV, pick up a moderate and significantly large divergent trend, respectively. The strongly divergent RQM-I model tricritical line looks very different from the RQM-S model tricritical line for the $m_\sigma = 600$ MeV. The RQM-S and RQM-I model $Z(2)$ chiral critical lines are likely to have similar shapes in that $\mu - m_K$ plane which corresponds to the $m_\pi = 138$ MeV since the CEP co-ordinates are very nearly identical in $\mu - T$ planes of the RQM-S and I model phase diagrams computed for the physical point parameters. Even though the chiral critical surfaces of the RQM-S and RQM-I models are similar and convergent on their corresponding chiral critical lines at the physical point, the RQM-I model critical surface gets lifted higher up in the μ direction near the ($m_\pi = 0, m_K > 400$ MeV), hence the tricritical line on its other end at the $m_\pi = 0$ becomes significantly divergent. The RQM-S model critical surface seems to have evenly leveled up rise in the μ direction for all m_π as its tricritical line at the $m_\pi = 0$ shows proper saturation that is consistent and desirable on the physical grounds also since the 2+1 flavor tricritical line is expected to be connected to the tricritical point of the two flavor chiral limit [142] at higher μ and m_K . Our first goal of comprehensively comparing the RQM-I and RQM-S model Columbia plots has

clearly established that the RQM-S model with the large N_c standard U(3) ChPT inputs, constitutes the improved and better framework for the Chiral limit studies.

The RQM-S model critical quantities $(m_K^{\text{TCP}}, m_\pi^t, m_\pi^c) \{ (m_s^{\text{TCP}}, m_{ud}^t, m_{ud}^c) \}$ in the $(m_\pi - m_K) \{ (m_{ud} - m_s) \}$ plane, get strongly reduced when the σ mass changes from $600 \rightarrow 750$ and 800 MeV to give significantly smaller values as $(159.85, 110.40, 87.90) \{ (10.65, 2.57, 1.64) \}$ MeV for the $m_\sigma = 750$ MeV and $(148.2, 103.19, 82.07) \{ (9.21, 2.25, 1.43) \}$ MeV for the $m_\sigma = 800$ MeV. The relative position of the RQM-S model TCP at $m_K^{\text{TCP}}/m_K^{\text{phys}}$ ($m_s^{\text{TCP}}/m_s^{\text{phys}}$), with respect to the value of kaon (s quark) mass at the physical point, shifts from the 0.5016 to 0.4405 (0.2927 to 0.2280) when the $m_\sigma = 400 \rightarrow 600$ MeV and one finds a significantly large shift in the $m_K^{\text{TCP}}/m_K^{\text{phys}}$ ($m_s^{\text{TCP}}/m_s^{\text{phys}}$) from the 0.4405 to 0.2988 (0.2280 to 0.1068) when the $m_\sigma = 600 \rightarrow 800$ MeV. In a similar fashion the $m_\pi^c (m_{ud}^c)$ changes from 134.51 (3.8) to 117.26 (2.9) MeV when the $m_\sigma = 400 \rightarrow 600$ whereas the change in the $m_\pi^c (m_{ud}^c)$ from 117.26 (2.9) to 82.07 (1.43) MeV is significantly large when the $m_\sigma = 600 \rightarrow 800$ MeV. Note that the very recent study in the Ref. [119] in the SICJT formalism [118] in the LSM, finds a stable first-order regime with a definite location of the TCP at $m_s^{\text{TCP}}/m_s^{\text{phys}} = 0.696$ which shows small variation on increasing the $m_{\sigma/f_0(500)}$ from 672.4 MeV to 797.2 MeV whereas the critical pion mass reported in their work is $m_\pi^c = 52.4$ MeV for the $m_{\sigma/f_0(500)} = 672.4$ MeV. The RQM-S model tricritical line for the case of $m_\sigma = 750$ MeV is very strongly divergent in the $\mu - m_K (\mu - m_s)$ plane as it suffers a small bending since the chemical potential becomes very high $\mu = 386.8$ MeV for quite a small kaon mass $m_K = 280$ MeV. Hence the associated chiral critical surface would exist in a very reduced range of $m_K^{\text{TCP}} = 159.85$ to $m_K = 280$ MeV on the m_K axis and $m_\pi = 0$ to $m_\pi^t = 110.4$ MeV on the m_π axis. Apart from demonstrating that the RQM-S model critical quantities go through a significantly large relative shifts when the m_σ becomes very high, our second goal of computing the Columbia plots for the higher $m_\sigma = 750$ MeV in the RQM-S model, has given us the idea of boundaries of a significantly smaller and shrunk shape of chiral critical surface that would be terminating well before the region under which lies the physical point, hence the associated critical end point CEP would not exist in the $\mu - T$ plane of the phase diagram.

It is important to note that even a weak chiral transition strength in the RQM-S model for $m_\sigma = 750$ MeV gives $(159.85, 110.40, 87.90)$ MeV for the values of critical quantities $(m_K^{\text{TCP}}, m_\pi^t, m_\pi^c)$ which are comparable to their values $(169, 110, 86)$ MeV reported in the e-MFA:FRG QM model study [35] where $m_\sigma = 530$ MeV and the spreads of first order regions in the horizontal $m_\pi - m_K$ plane, look similar in both the studies. Furthermore, even the significantly diluted strength of chiral transition, for a very high $m_\sigma = 800$ MeV in the RQM-S model, gives the critical quantities $(m_K^{\text{TCP}}, m_\pi^t, m_\pi^c) \equiv (148.2, 103.19, 82.07)$ MeV

which turn out to be larger than the critical quantities $(m_K^{\text{TCP}}, m_\pi^t, m_\pi^c) = (137.2, 98.15, 78.45)$ MeV reported for the case of small $m_\sigma = 400$ MeV in the QMVT model Columbia plot in the Ref. [129]. Thus the third goal of the present work gives us the quantitative evidence and strongly confirms the conclusion that the effect of quark one-loop vacuum correction is quite moderate due to on-shell renormalization of the parameters in the RQM-S model whereas the strength of chiral transition gets strongly softened and diluted by a very large smoothing influence of the quark one-loop vacuum fluctuations when its effect gets treated in the $\overline{\text{MS}}$ scheme of renormalization and the curvature masses of mesons are used to fix the model parameters. Here, it is worthwhile to recall that the critical $m_\pi^c \equiv 150$ MeV and the chiral

transition is first order everywhere on the m_K axis for $m_\pi = 0$ when the quark one-loop vacuum fluctuations are neglected under the s-MFA in the Ref. [82] for the case of $m_\sigma = 800$ MeV. We finally conclude by noting that the range $m_{ud}^c = 3.8$ to 1.43 MeV of critical light quark mass values, for different m_σ , found in our present RQM-S model work, lies well within the range of $m_{ud}^c \leq 4$ MeV given by recent LQCD study using Möbius domain wall fermions in Ref. [41].

ACKNOWLEDGMENTS

I would like to express my sincere gratitude towards Suraj Kumar Rai, Akanksha Tripathi and Pooja Kumari for the careful readings of the manuscript. I am deeply indebted and very much tankful to Swatantra Kumar Tiwari for making the three dimensional Columbia plots.

[1] N. Cabibbo and G. Parisi, *Phys.Lett.B* **59**, 67-69 (1975).

[2] L. D. McLerran and B. Svetitsky, *Phys. Rev. D* **24**, 450 (1981); B. Svetitsky, *Phys. Rep.* **132**, 1 (1986).

[3] B. Muller, *Rep. Prog. Phys.* **58**, 611 (1995).

[4] H. Meyer-Ortmanns, *Rev. Mod. Phys.* **68**, 473 (1996).

[5] D. H. Rischke, *Prog. Part. Nucl. Phys.* **52**, 197 (2004).

[6] N. Aghanim et al. (Planck Collaboration), *Astron. Astrophys.* **641**, A6 (2020).

[7] H.-w. Zheng, F. Gao, L. Bian, S.-x. Qin, and Y.-x. Liu, *Phys. Rev. D* **111**, L021303 (2025).

[8] M. Buballa, *Phys. Rep.* **407**, 205 (2005).

[9] K. Fukushima and C. Sasaki, *Prog. Part. Nucl. Phys.* **72**, 99 (2013).

[10] M. Oertel, M. Hempel, T. Klähn, and S. Typel, *Rev. Mod. Phys.* **89**, 015007 (2017).

[11] M. Aggarwal et al. (STAR Collaboration), *Phys. Rev. Lett.* **105**, 022302 (2010).

[12] G. Odyniec; RHIC Beam Energy Scan Program: Phase I and II, *PoS CPOD 2013*, 043(2013) and *PoS CORFU2018* 151 (2019).

[13] Pandav, Ashish; *EPJ Web Conf.* **296**, 01016, (2024) ; A. Pandav (STAR collaboration), plenary talk at CPOD 2024, .

[14] M. Stephanov, *EPJ Web of Conferences* **314**, 00042 (2024).

[15] S. Borsányi, Z. Fodor, C. Hoelbling, S. D. Katz, S. Krieg, C. Ratti, and K. K. Szabó, *J. High Energy Phys.* **09**, (2010) 073.

[16] S. Borsányi, G. Endrodi, Z. Fodor, A. Jakovac, S. D. Katz, S. Krieg, C. Ratti and K. K. Szabó, *JHEP* **11**, (2010) 077.

[17] A. Bazavov et al., *Phys. Rev. D* **85**, 054503 (2012)

[18] S. Borsányi, Z. Fodor, C. Hoelbling, S. D. Katz, S. Krieg and K. K. Szabó, *Phys. Lett. B* **730**, 99-104 (2014).

[19] A. Bazavov et al., *Phys. Rev. D* **90**, 094503 (2014).

[20] R. D. Pisarski and F. Wilczek, *Phys. Rev. D* **29**, 338 (1984).

[21] G. 't Hooft, *Phys. Rev. Lett.* **37**, 8 (1976)

[22] F. R. Brown, F. P. Butler, H. Chen, N. H. Christ, Z.-h. Dong, W. Schaffer, L. I. Unger and A. Vaccarino, *Phys. Rev. Lett.* **65**, 2491 (1990).

[23] M. Fromm, J. Langelage, S. Lottini, and O. Philipsen, *JHEP* **01**, 042 (2012).

[24] H. Saito, S. Ejiri, S. Aoki, K. Kanaya, Y. Nakagawa, H. Ohno, K. Okuno, and T. Umeda, *Phys. Rev. D* **89**, 034507 (2014).

[25] U. Reinosa, J. Serreau, and M. Tissier, *Phys. Rev. D* **92**, 025021 (2015).

[26] C. S. Fischer, J. Luecker, and J. M. Pawłowski, *Phys. Rev. D* **91**, 014024 (2015).

[27] J. Maelger, U. Reinosa, and J. Serreau, *Phys. Rev. D* **98**, 094020 (2018).

[28] F. Karsch, E. Laermann, and A. Peikert, *Nucl. Phys. B* **605**, 579 (2001).

[29] F. Karsch, E. Laermann, and C. Schmidt, *Phys. Lett. B* **520**, 41 (2001).

[30] F. Karsch, C. R. Allton, S. Ejiri, S. J. Hands, O. Kaczmarek, E. Laermann, and C. Schmidt, *Nucl. Phys. Proc. Suppl.* **129**, 614 (2004).

[31] P. de Forcrand, S. Kim and O. Philipsen, *Proc. Sci. LATTICE2007*, (2007) 178 [arXiv:0711.0262].

[32] X.-Y. Jin, Y. Kuramashi, Y. Nakamura, S. Takeda, and A. Ukawa, *Phys. Rev. D* **91**, 014508 (2015).

[33] X.-Y. Jin, Y. Kuramashi, Y. Nakamura, S. Takeda, and A. Ukawa, *Phys. Rev. D* **96**, 034523 (2017).

[34] P. de Forcrand and M.D'Elia *Proc. Sci. LATTICE2016*, (2017) 081 [arXiv:1702.00330].

[35] Simon Resch, Fabian Rennecke and Bernd-Jochen Schaefer *Phys. Rev. D* **99**, 076005 (2019).

[36] Y. Kuramashi, Y. Nakamura, H. Ohno, and S. Takeda, *Phys. Rev. D* **101**, 054509 (2020).

[37] A. Bazavov, H. T. Ding, P. Hegde, F. Karsch, E. Laermann, S. Mukherjee, P. Petreczky, and C. Schmidt, *Phys. Rev. D* **95**, 074505 (2017).

[38] L. Dini, P. Hegde, F. Karsch, A. Lahiri, C. Schmidt, and S. Sharma, *Phys. Rev. D* **105**, 034510 (2022).

[39] L. Varnhorst, *Proc. Sci. LATTICE2014*, (2015) 193.

[40] F. Cuteri, O. Philipsen, and A. Sciarra, *JHEP* **11**, 141 (2021).

[41] Y. Zhang, Y. Aoki, S. Hashimoto, I. Kanamori, T. Kaneko, and Y. Nakamura, *Proc. Sci. LATTICE2023* (2024) 203 [arXiv:2401.05066].

[42] J. Bernhardt and C.-S. Fischer, *Phys. Rev. D* **108**, 114018 (2023).

[43] S. R. Kousvos and A. Stergiou, *SciPost Phys.* **15**, 075 (2023).

[44] G. Fejos, *Phys. Rev. D* **105**, L071506 (2022).

[45] G. Fejos, T. Hatsuda, *Phys. Rev. D* **110**, 016021 (2024).

[46] V. Dick, F. Karsch, E. Laermann, S. Mukherjee, and S. Sharma, *Phys. Rev. D* **91**, 094504 (2015).

[47] H. T. Ding, S. T. Li, S. Mukherjee, A. Tomiya, X. D. Wang, and Y. Zhang, *Phys. Rev. Lett.* **126**, 082001 (2021).

[48] O. Kaczmarek, L. Mazur, and S. Sharma, *Phys. Rev. D* **104**, 094518 (2021).

[49] A. Bazavov, T. Bhattacharya, M. I. Buchoff, M. Cheng, N. H. Christ, H.-T. Ding *et al.*, *Phys. Rev. D* **86**, 094503 (2012).

[50] T. Bhattacharya, M. I. Buchoff, N. H. Christ, H.-T. Ding, R. Gupta, C. Jung *et al.*, *Phys. Rev. Lett.* **113**, 082001 (2014).

[51] O. Kaczmarek, R. Shanker, and S. Sharma, *Phys. Rev. D* **108**, 094051 (2023).

[52] B. B. Brandt, A. Francis, H. B. Meyer, O. Philipsen, D. Robaina, and H. Wittig, *J. High Energy Phys.* **12** (2016), 158.

[53] A. Tomiya, G. Cossu, S. Aoki, H. Fukaya, S. Hashimoto, T. Kaneko, and J. Noaki, *Phys. Rev. D* **96**, 034509 (2017); **96**, 079902(A) (2017).

[54] S. Aoki, Y. Aoki, G. Cossu, H. Fukaya, S. Hashimoto, T. Kaneko, C. Rohrhofer, and K. Suzuki, *Phys. Rev. D* **103**, 074506 (2021).

[55] S. Aoki, Y. Aoki, H. Fukaya, S. Hashimoto, C. Rohrhofer, and K. Suzuki, *Prog. Theor. Exp. Phys.* **2022**, 023B05 (2022).

[56] A. Lahiri, *Proc. Sci. LATTICE2021* (2022) 003 [arXiv:2112.08164].

[57] A. Gomez Nicola, J. Ruiz de Elvira and R. Torres Andres, *Phys. Rev. D* **88**, 076007 (2013).

[58] A. Gomez Nicola, J. Ruiz de Elvira, *JHEP* **03**, (2016) 186.

[59] A. Gomez Nicola, J. Ruiz de Elvira, *Phys. Rev. D* **97**, 074016 (2018).

[60] A. Gomez Nicola, J. Ruiz de Elvira, *Phys. Rev. D* **98**, 014020 (2018).

[61] S. Ferreres-Sole, A. Gomez Nicola and A. Vioque-Rodriguez, *Phys. Rev. D* **99**, 036018 (2019).

[62] R. D. Pisarski and F. Rennecke, *Phys. Rev. Lett.* **132**, 251903 (2024).

[63] Francesco Giaosa, Gyozo Kovacs, Peter Kovacs, R. D. Pisarski and Fabian Rennecke, *Phys. Rev. D* **111**, 016014 (2025).

[64] H. Meyer-Ortmanns and B. J. Schaefer, *Phys. Rev. D* **53**, 6586 (1996).

[65] J. T. Lenaghan, D. H. Rischke and J. Schaffner-Bielich, *Phys. Rev. D* **62**, 085008 (2000).
J. T. Lenaghan, D. H. Rischke, *J. Phys. G* **26**, 431 (2000).

[66] J. T. Lenaghan, *Phys. Rev. D* **63**, 037901 (2001).

[67] D. Roder, J. Ruppert and D. H. Rischke, *Phys. Rev. D* **68**, 016003 (2003).

[68] A. Jakovac, A. Patkos, Z. Szep, and P. Szepfalusy, *Phys. Lett. B* **582**, 179 (2004).

[69] T. Herpay, A. Patkós, Zs. Szép and P. Szépfalusy, *Phys. Rev. D* **71**, 125017 (2005).

[70] T. Herpay and Zs. Szép, *Phys. Rev. D* **74**, 025008 (2006).

[71] P. Kovács and Zs. Szép, *Phys. Rev. D* **75**, 025015 (2007).

[72] A. Jakovac and Zs. Szep, *Phys. Rev. D* **82**, 125038, (2010).

[73] G. Marko and Zs. Szep, *Phys. Rev. D* **82**, 065021 (2010).

[74] G. Fejos, A. Patkos, *Phys. Rev. D* **82**, 045011 (2010).

[75] O. Scavenuius, A. Mocsy, I. N. Mishustin, and D. H. Rischke, *Phys. Rev. C* **64**, 045202 (2001).

[76] A. Mocsy, I. N. Mishustin, and P. J. Ellis, *Phys. Rev. C* **70**, 015204 (2004).

[77] B.-J. Schaefer and J. Wambach, *Nucl. Phys. A* **757**, 479 (2005).

[78] B.-J. Schaefer and J. Wambach, *Phys. Rev. D* **75**, 085015 (2007).

[79] B. J. Schaefer, J. M. Pawłowski, and J. Wambach, *Phys. Rev. D* **76**, 074023 (2007).

[80] E. S. Bowman and J. I. Kapusta, *Phys. Rev. C* **79**, 015202 (2009); J. I. Kapusta, and E. S. Bowman, *Nucl. Phys. A* **830**, 721C (2009).

[81] B. J. Schaefer and M. Wagner, *Prog. Part. Nucl. Phys.* **62**, 381 (2009).

[82] B. J. Schaefer and M. Wagner, *Phys. Rev. D* **79**, 014018 (2009).

[83] B. J. Schaefer, M. Wagner and J. Wambach, *CPOD*(2009)017, arXiv:0909.0289

[84] B. J. Schaefer, M. Wagner, and J. Wambach, *Phys. Rev. D* **81**, 074013 (2010).

[85] H. Mao, J. Jin, and M. Huang, *J. Phys. G* **37**, 035001.

[86] U. S. Gupta and V. K. Tiwari, *Phys. Rev. D* **81**, 054019(2010).

[87] L. Ferroni, V. Koch, and M. B. Pinto, *Phys. Rev. C* **82**, 055205 (2010).

[88] Andreas Zacchi and Jürgen Schaffner-Bielich, *Phys. Rev. D* **97**, 074011 (2018).

[89] Andreas Zacchi and Jürgen Schaffner-Bielich, *Phys. Rev. D* **100**, 0123024 (2019).

[90] Pedro Costa, M. C. Ruivo, C. A. de Sousa and Yu. L. Kalinovsky, *AIP Conf. Proc.* **775**, 173–181 (2005).

[91] Pedro Costa, M. C. Ruivo, C. A. de Sousa and Yu. L. Kalinovsky, *Phys. Rev. D* **71**, 116002 (2005).

[92] K. Fukushima, *Phys. Rev. D* **77**, 114028 (2008); **78**, 039902(E) (2008) .

[93] J. Berges, D.-U. Jungnickel, and C. Wetterich, *Phys. Rev. D* **59**, 034010 (1999).

[94] J. Berges, N. Tetradis, and C. Wetterich, *Phys. Rept.* **363**, 223 (2002).

[95] H. Gies and C. Wetterich, *Phys. Rev. D* **69**, 025001 (2004).

[96] J. Braun and H. Gies, *JHEP* **06**, 024 (2006).

[97] J. M. Pawłowski, *Annals Phys.* **322**, 2831 (2007)

[98] K. Fukushima, K. Kamikado and B. Klein, *Phys. Rev. D* **83**, 116005 (2011).

[99] T. K. Herbst, J. M. Pawłowski, and B.-J. Schaefer, *Phys. Rev. D* **88**, 014007 (2013).

[100] M. Grahl and D. H. Rischke, *Phys. Rev. D* **88**, 056014 (2013).

[101] M. Mitter and B.-J. Schaefer, *Phys. Rev. D* **89**, 054027 (2014).

[102] M. Drew, W. Weise, *Phys. Rev. C* **91**, 035802 (2015).

[103] G. Fejos, *Phys. Rev. D* **92**, 036011 (2015).

[104] F. Rennecke, *Phys. Rev. D* **92**, 076012 (2015).

[105] J. Braun, L. Fister, J. M. Pawłowski, and F. Rennecke, *Phys. Rev. D* **94**, 034016 (2016).

[106] G. Fejos, A. Hosaka, *Phys. Rev. D* **94**, 036005 (2016).

[107] Fabian Rennecke, Bernd-Jochen Schaefer, *Phys. Rev. D* **96**, 016009 (2017).

[108] M. Drew, W. Weise, *Prog. Part. Nucl. Phys.* **93**, 69 (2017).

[109] R.-A. Tripolt, B. -J. Schaefer, L. von Smekal, J. Wambach, *Phys. Rev. D* **97**, 034022 (2018).

[110] G. Fejos, A. Hosaka, *Phys. Rev. D* **98**, 036009 (2018).

[111] L. Brandes, N. Kaiser, W. Weise, *Eur. Phys. J. A* **57:243**, (2021).

[112] G. Fejos, A. Patkos, *Phys. Rev. D* **105**, 096007 (2022).

[113] G. Fejos and A. Patkos, *Phys. Rev. D* **109**, 036035 (2024).

[114] J. Braun, L. M. Haas, F. Marhauser, and J. M. Pawlowski, *Phys. Rev. Lett.* **106**, 022002 (2011).

[115] J. Braun, W.-j. Fu, J. M. Pawlowski, F. Rennecke, D. Rosenblüh, and S. Yin, *Phys. Rev. D* **102**, 056010 (2020).

[116] J.M.Pawlowski and F. Rennecke, *Phys. Rev. D* **90**, 076002 (2014).

[117] J. R. Pelaez, *Phys. Rept.* **658**, 1 (2016).

[118] A. Pilaftsis and D. Teresi, *Nucl. Phys. B* **874**, 594 (2013). H. Mao, *Nucl. Phys. A* **925**, 185 (2014).

[119] Yuepeng Guan, Mamiya Kawaguchi, Shinya Matsuzaki and Akio Tomiya, *Phys. Rev. D* **113**, 014013 (2026).

[120] P. Adhikari, J. O. Andersen and P. Kneschke, *Phys. Rev. D* **95**, 036017 (2017).

[121] P. Adhikari, J. O. Andersen and P. Kneschke, *Phys. Rev. D* **96**, 016013 (2017).

[122] P. Adhikari, J. O. Andersen and P. Kneschke, *Phys. Rev. D* **98**, 074016 (2018).

[123] A. Folkestad, J. O. Andersen, *Phys. Rev. D* **99**, 054006 (2019).

[124] S. K. Rai and V. K. Tiwari, *Phys. Rev. D* **105**, 094010 (2022).

[125] S. K. Rai and V. K. Tiwari, *Phys. Rev. D* **108**, 074014 (2023).

[126] V. K. Tiwari, *Phys. Rev. D* **108**, 074002 (2023).

[127] S. K. Rai and V. K. Tiwari, *Phys. Rev. D* **109**, 034025 (2024).

[128] V. K. Tiwari, *Phys. Rev. D* **111**, 114014 (2025).

[129] V. K. Tiwari, *Phys. Rev. D* **112**, 054046 (2025).

[130] Jens O. Andersen, Mathias P. Nødtvedt, arXiv:2506.02941[hep-ph], 2025

[131] Hosein Gholami, Kurth Lennart, Ugo Mire, Michael Buballa and Bernd-Jochen Schaefer, arXiv:2505.22542[hep-ph], 2025

[132] J. Gasser and H. Leutwyler, *Nucl. Phys. B* **250**, 465 (1985).

[133] H. Leutwyler, *Phys. Lett. B* **374**, 163 (1996).

[134] R. Kiaser and H. Leutwyler, *Eur. Phys. J. C* **17**, 623 (2000).

[135] P. Herrera-Siklody, J. I. Latorre, P. pascual and J. Taron, *Nucl. Phys. B* **497**, 345 (1997).

[136] P. Herrera-Siklody, J. I. Latorre, P. pascual and J. Taron, *Phys. Lett. B* **419**, 326 (1998).

[137] R. Escribano, F. S. Ling, M. H. G. Tytgat, *Phys. Rev. D* **62**, 056004 (2000).

[138] B. Borasoy and S. Wetzel, *Phys. Rev. D* **63**, 074019 (2001).

[139] N. Beisert and B. Borasoy, *Eur. Phys. J. A* **11**, 329 (2001).

[140] N. Beisert and B. Borasoy, *Nucl. Phys. A* **705**, 433 (2002).

[141] T. Becher and H. Leutwyler, *Eur. Phys. J. C* **9**, 643 (1999).

[142] A. Halasz, A. D. Jackson, R. E. Shrock, M. A. Stephanov, and J. J. M. Verbaarschot, *Phys. Rev. D* **58**, 096007 (1998).

[143] V. Skokov, B. Friman, E. Nakano, K. Redlich, and B.-J. Schaefer, *Phys. Rev. D* **82**, 034029 (2010).

[144] R. Khan and L. T. Kyllingstad, *AIP Conf. Proc.* **1343**, 504 (2011).

[145] B.-J. Schaefer and M. Wagner, *Phys. Rev. D* **85**, 034027 (2012).

[146] U. S. Gupta, V. K. Tiwari, *Phys. Rev. D* **85**, 014010 (2012).

[147] V. K. Tiwari, *Phys. Rev. D* **86**, 094032 (2012).

[148] V. K. Tiwari, *Phys. Rev. D* **88**, 074017 (2013).

[149] S. K. Rai and V. K. Tiwari, *Eur. Phys. J. Plus* **135:844**, (2020).

[150] K. Kajantie, M. Laine, K. Rummukainen, and M. E. Shaposhnikov *Nucl. Phys. B* **458**, 90 (1996).

[151] S. Carignano, M. Buballa and B-J Schaefer *Phys. Rev. D* **90**, 014033 (2014).

[152] S. Carignano, M. Buballa, and W. Elkamhawy, *Phys. Rev. D* **94**, 034023 (2016).

[153] R. Kobes, G. Kunstatter, and A. Rebhan, *Phys. Rev. Lett.* **64**, 2992 (1990); *Nucl. Phys. B* **355**, 1 (1991).

[154] A. K. Rebhan, *Phys. Rev. D* **48**, R3967 (1993).

[155] S. Eidelman et. al. (Particle Data Group), *Phys. Lett. B* **592**, 1 (2004).

[156] P. de Forcrand, and O. Philipsen, Wittig, *J. High Energy Phys.* **01** (2007), 077.